TECHNISCHE UNIVERSITÄT MÜNCHEN

Munich School of Engineering

Polythiophene thin films: Structure formation during in situ polymerization

Jenny Lebert

Vollständiger Abdruck der von der Munich School of Engineering der Technischen Universität München zur Erlangung des akademischen Grades eines

Doktors der Naturwissenschaften (Dr. rer. nat.)

genehmigten Dissertation.

München, Mai 2018

TECHNISCHE UNIVERSITÄT MÜNCHEN

Munich School of Engineering

Polythiophene thin films: Structure formation during in situ polymerization

Jenny Lebert

Vollständiger Abdruck der von der Munich School of Engineering der Technischen Universität München zur Erlangung des akademischen Grades eines

Doktors der Naturwissenschaften (Dr. rer. nat.)

genehmigten Dissertation.

Vorsitzender:	Prof. Dr. Karsten Reuter
Prüfer der Dissertation:	1. Prof. Dr. Eva M. Herzig
	2. Prof. Dr. Peter Müller-Buschbaum

Die Dissertation wurde am 29.05.2018 bei der Technischen Universität München eingereicht und durch die Munich School of Engineering am 17.10.2018 angenommen.

Abstract

The structure formation of native polythiophene (PT) thin films during *in situ* polymerization is the center of this thesis. A solution-based synthesis is developed that enables the fabrication of conducting and semiconducting PT films, respectively. The established synthesis employs an oxidative polymerization mechanism in which the oxidizing agent additionally serves as chemical dopant. A structural analysis reveals that the polymer aggregation upon heavy doping during film formation results in a novel PT crystal structure with improved intermolecular interactions. Furthermore, an experimental routine is presented that enables to track the film formation dynamics by performing simultaneous time-resolved grazing-incidence wide-angle X-ray scattering (GIWAXS) and UV/Vis transmission measurements. A model is extracted which illustrates the impact of the concentration of oxidizing agent on the reactions kinetics and on the evolution of the doping level throughout the whole process. Finally, the nanomorphology of the semiconducting PT films is shown to be tunable with respect to their porosity by employing water as solvent additive. Overall, this work contributes to the understanding of relevant structure formation processes and how those can be exploited for manipulating the morphology and resulting key material properties in PT thin films.

Zusammenfassung

Diese Dissertation befasst sich im Kern mit der Strukturbildung in *in situ* polymerisierten Polythiophen-Dünnschichten. Eine lösungsbasierte Synthese wird entwickelt, die die Herstellung von leitenden sowie halbleitenden PT-Filmen ermöglicht. Die Grundlage dieser Synthese ist ein oxidative Polymerisationsreaktion, in der das eingesetzte Oxidationsmittel zusätzlich in der Lage ist die gebildeten Polymere chemisch zu dotieren. Es wird gezeigt, dass die Aggregation der Polymerketten bei starker Dotierung während der Filmbildung zu einer neuartigen Kristallstruktur mit verstärkten intermolekularen Wechselwirkungen führt. Weiterhin wird ein Messkonzept aus kombinierten zeitaufgelösten Messungen von Röntgen-Weitwinkel-Streuung und UV/Vis-Transmission vorgestellt, welches die Verfolgung der Filmbildung ermöglicht. Aus den experimentellen Daten wird ein Modell abgeleitet, dass den Einfluss der Oxidationsmittelkonzentration auf die Reaktionskinetik sowie den Grad der Dotierung während des gesamten Prozesses darstellt. Abschließend wird gezeigt, dass die Nanomorphologie der halbleitenden PT-Dünnschichten manipulierbar ist, indem der Einfluss von Wasser als Lösungsmittel-Additiv auf ihre Porosität untersucht wird. Insgesamt liefert diese Arbeit einen Beitrag zum Verständnis von relevanten Strukturbildungsprozessen, die zur Morphologiekontrolle und damit zum Einstellen von wichtigen Materialeigenschaften verwendet werden können.

Contents

List of Abbreviations

BHJ	bulk heterojunction
BT	2,2'-bithiophene
DESY	Deutsches Elektronen Synchrotron
DOS	density of states
FeTos	iron p-toluenesulfonate
FF	fill factor
FWHM	full width at half maximum
GISAXS	grazing-incidence small-angle X-ray scattering
GIWAXS	grazing-incidence wide-angle X-ray scattering
GIXS	grazing-incidence X-ray scattering
HB	herringbone
HOMO	highest occupied molecular orbital
ITO	indium tin oxide
I-V	current-voltage characteristics
LCAO	linear combination of molecular orbitals
LMA	local monodisperse approximation
LUMO	lowest unoccupied molecular orbital
MD	molecular dynamics
MIS-CELIV	metal-insulator-semiconductor-charge extraction by linearly increasing voltage
MPP	maximum power point
oCVD	oxidative chemical vapor deposition
P3HT	poly(3-hexylthiophene)
PEDOT	poly(3,4-ethylenedioxy-thiophene)
PES	potential energy surface
PL	photoluminescence
PMA	phopshomolybdic acid hydrate
PP	polypropylene
PSS	polystyrene sulfonate

PT	polythiophene
rpm	revolutions per minute
SCE	saturated calomel electrode
SEM	scanning electron microscopy
SLD	scattering length density
UV/Vis	ultraviolet and visible light
XT	oligothiophenes

1. Introduction

Conductive polymers were first discovered in the 1970s by Alan J. Heeger, Alan G. MacDiarmid, and Hideki Shirakawa. [1] For their detection of electrical conductivity in iodine-doped polyacetylene they were awarded the Nobel prize in chemistry in 2000. Since then, conductive polymers have gained a major interest in research and industry because of their highly attractive application in organic electronic devices. These have increasingly come more into focus as the world-wide growing energy demand is attracting public attention. [2] As a consequence, new solutions for decentralized energy supply are required. New markets are opening up, in which the application of organic semiconductors is more attractive than that of conventional inorganic ones such as silicon. Organic solar cells, for example, allow the conversion of sunlight into electricity in niche field applications that the common inorganic technologies are unable to cover. [3] This is possible because organic photovoltaic devices can be light-weight, are producible on mechanically flexible substrates, and can be tuned with regard to their optical properties by help of synthetic chemistry. [4–7] Due to the solution-processability of the materials the device fabrication can be up-scaled easily by roll-to-roll fabrication techniques such as printing. [8] This facilitates the production of devices in different size-regimes for implementation in buildings, wearables, or portable devices. [3, 9] Beyond photovoltaics, conductive polymers are also employed in technologies such as organic light-emitting diodes (OLEDs), energy-storage devices, and organic field-effect transistors (OFETs). [10–14]

The origin of conductivity in polymers lies in their conjugated π orbital system which enables the transport of charge carriers. [15] Therefore, their electronic properties strongly depend on their crystallinity, conjugation length, intermolecular orbital overlap, and orientation of the crystallites. [16–18] An efficient charge transport along a single polymer chain requires an stretched backbone, which results in a long conjugation length. Intermolecular charge transport, on the other hand, is mostly governed by the aggregation behavior of the polymer chains and the resulting π orbital overlap. Hence, some of the key morphological properties in organic thin film devices are their molecular conformation, short- and long-range order, and domain sizes in material blends. [19]

Polythiophenes are an important class of conjugated polymers. Especially the substituted derivatives poly(3-hexylthiophene) (P3HT) and poly(3,4-ethylenedioxythiophene)

(PEDOT) are two of the most intensely studied (semi)conducting polymers in the field of organic electronic devices. P3HT is typically employed in its semiconducting state to serve as absorbing material in the active layer of organic solar cells. [20, 21] PEDOT is rather employed in its doped state in which it obtains sufficient electrical conductivities for application as transparent and flexible electrode material. [22–24]

Native, unsubstituted polythiophene (PT), on the other hand, is not often considered for device applications because it is not easily processable from solution due to its complete insolubility. Nevertheless, PT is a promising material because its chemical stability is strongly enhanced in comparison to that of its soluble derivatives. This stability originates in its closer packing structure preventing the permeation of for example oxygen into its structure. [25,26] Therefore, several *in situ* polymerization techniques have been developed that enable the fabrication of insoluble PT thin films. In *in situ* polymerization approaches the polymer insolubility is overcome by initially depositing the soluble monomers and subsequently performing the actual synthesis of the polymer directly on the substrate. The major advantage of such syntheses is their potentially low costs, as the synthetic effort is significantly reduced in comparison to that of the polymerization of substituted polythiophene derivatives.

The *in situ* polymerization techniques presented in literature typically employ an oxidative reaction mechanism in which the monomers are activated for polymerization by oxidation. [27,28] This oxidation can either be done electrochemically or chemically. In an electrochemical polymerization the substrate is utilized as anode in an electrochemical cell. Upon application of a cell voltage a polymer film is formed on the substrate surface. [29–31] The main drawback of such electrochemical syntheses is their restriction with respect to suitable substrates as these need to be electrically conducting. Chemical polymerization mechanisms, on the other hand, employ oxidizing agents for monomer oxidation, thereby making the synthesis independent of the substrate material. The application of monomer and oxidant can be performed from either solution or by evaporation. [32–37] While the latter typically suffers from a rather high energy consumption, solution-based approaches promise a simple upscaling to the fabrication of larger devices.

While the fabrication of PT thin films is easily feasible with the variety of literature-known *in situ* syntheses, the respective electronic devices still suffer from low performance. Without addition of any side chains, native PT typically exhibits a rather low degree of crystallinity. Moreover, it aggregates in a herringbone motif that results from the electrostatic repulsion of the π-orbitals of neighboring chains. [38] As a result, its morphology in thin films typically yields insufficient charge transport properties. Nevertheless, structural investigations and approaches for morphological tuning play only a very minor role in the optimization of *in situ* polymerization techniques. This is despite the fact that

the processes typically depend on a large number of parameters that could potentially be exploited for structural control once their influence is revealed. However, the underlying film formation mechanisms are often not investigated nor discussed. Consequently, understanding the structure formation during *in situ* polymerization is still of high significance in order to tune the properties of unsubstituted conducting polymers to their optimum.

2. Objective

The introduction showed that there is still knowledge lacking on the film formation processes during *in situ* polymerization of semiconducting polymer thin films. As a result, it is difficult to optimize these functional layers under consideration of fabrication-structure-function relations. The aim of this thesis is to get a more detailed insight on solution-based *in situ* polymerization techniques, using polythiophene as model material system. A special focus is put into the polymer morphology on different length scales and how the chosen fabrication route can be employed for an increased structural control. For this purpose, the project is divided into four different parts that are introduced in the following and schematically depicted in figure 2.1.

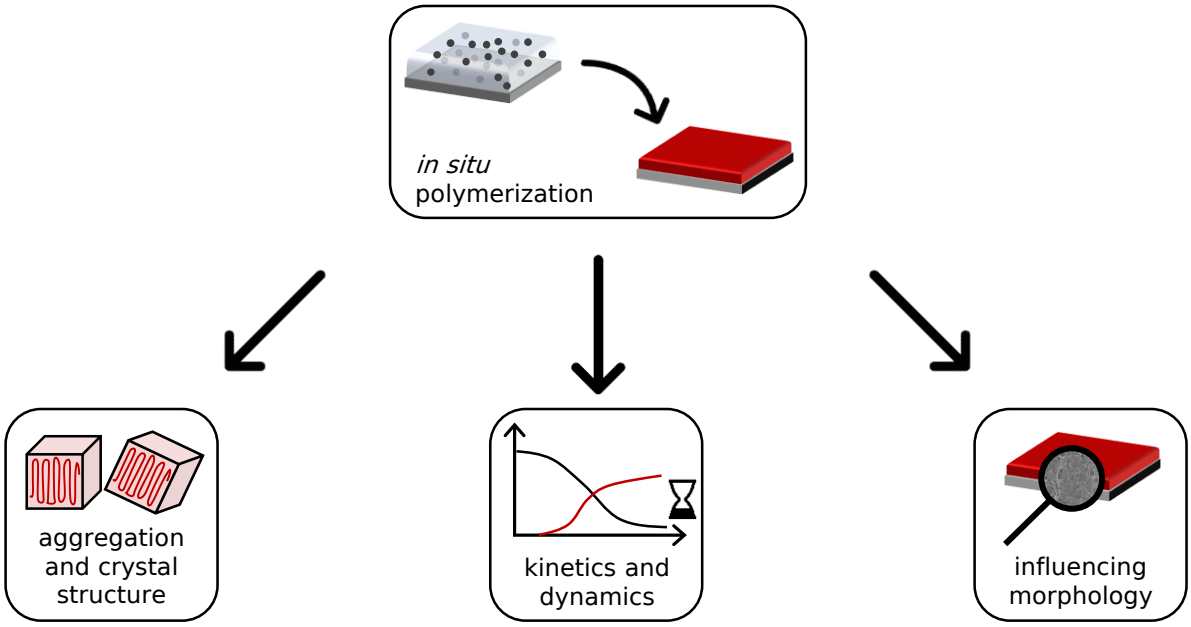

Figure 2.1.: Graphical overview of topics addressed in this thesis. A solution-based *in situ* polymerization for polythiophene thin films is developed. Thereafter, the film formation process and the impact of different reaction parameters on the morphology are investigated in terms of doping-induced modification of the polymer crystal structure, the reaction and drying kinetics, and the change in nano-morphology upon application of water as an additive.

Initially, it is necessary to establish an *in situ* polymerization routine, which shall meet two main demands. Firstly, the process is supposed to be solution-based, thereby enabling the fabrication of films by up-scalable techniques like printing. Secondly, the resulting films should be of sufficient quality to enable their application in the active layer of organic solar cells. Chapter 6 discusses the adaption and optimization of a literature-known method which employs so-called metastable reaction mixtures, utilizing special oxidizing agents for the polymerization. The resulting films are analyzed regarding their (opto)electronic properties and finally implemented in organic bilayer solar cells.

In oxidative polymerization reactions the oxidizing agent additionally serves as chemical dopant, meaning it is further able to oxidize the polymer chains following their formation. This synthesis-intrinsic doping can be reversed after the actual film formation by post-treatment with reducing solvents. However, during the film formation the doping is expected to have an impact on the aggregation of the polythiophene chains. Hence, the possibilities to exploit this doping for altering the crystal structures in both doped, conducting and undoped, semiconducting thin films are investigated in chapter 7.

The observed aggregation behavior upon doping raises the question, at which point in the fabrication the doping reaction is actually happening. In order to gain a deeper understanding of the film formation simultaneous time-resolved spectroscopic measurements and X-ray scattering experiments are performed. For this purpose, the polymerization is performed by slot-die printing the reaction mixture in a printer setup implemented at a synchrotron beamline. The data analysis and concluded film formation model are introduced and discussed in chapter 8.

Finally, the morphological tuning on a larger length scale is the focus of chapter 9. This is of high interest, as blending the polymer with a second functional material is difficult during *in situ* polymerization. Hence, a tuning of film porosity enables a strong increase in the polymer surface, which can potentially be exploited in backfilling processes. Here, the impact of water on the film porosity is investigated by applying it as solvent additive during the reaction. Additionally, the crystallization of reaction by-products inside the polymer matrix is studied and proposed to be the origin of the variation in porosity and pore size.

The other chapters cover the necessary theoretical background (chapter 3), information on the employed characterization methods (chapter 4), and the details on employed materials and sample preparation (chapter 5).

Finally, a conclusion and remaining open questions are given in chapter 10.

3. Theoretical aspects

This chapter gives an introduction to the theoretical aspects of the topics discussed in this thesis. First, some basic concepts of polymer physics are introduced in section 3.1, ranging from general definitions to polymer crystallinity, and at the end of the chapter the origin of conductivity in organic systems (section 3.1.1). Thereafter, the polymerization of semiconducting polymers with special focus on the *in situ* polymerization of polythiophene is discussed in section 3.2.

A large part of this thesis deals with structural investigations on polymer thin films performed by means of X-ray scattering techniques. The respective basics are introduced in section 3.3.1. The specifics of scattering under grazing incidence are discussed further in section 3.3.2.

3.1. Basics of polymer physics

The word *polymer* originates from the combination of two Greek words: *poly* (many) and *mer* (part). Polymers are macromolecules that are composed of a large number of repeating building blocks, the monomers. A chemical reaction linking the monomers is called polymerization. Naturally, the chemical and physical properties of polymer molecules are strongly related to those of their monomer molecules. Moreover, the number of linked monomers n plays a crucial role, as the influence of the addition or removal of a single monomer unit is strong for short or medium long chains and becomes almost negligible if the chain is sufficiently long. Therefore, it is convenient to roughly distinguish between single monomers ($n = 1$), oligomers ($n > 1$), and polymers ($n >> 1$). n is also referred to as degree of polymerization.

In order to serve as a monomer in a polymerization reaction, a molecule needs to contain at least one polymerizable chemical group. Figure 3.1 shows the schematic reaction of propene to polypropylene. Here, the double bond of the monomer can be activated for polymerization.

All synthetic polymerization reactions are statistical processes which result in polymers of not one exact degree of polymerization but rather a distribution of different chain

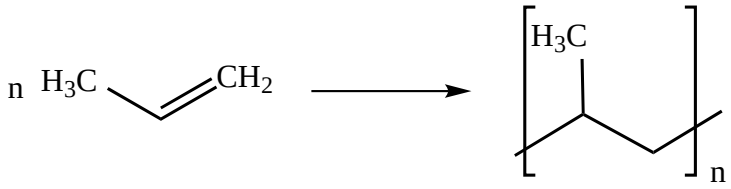

Figure 3.1.: Schematic polymerization equation of propene to polypropylene, with n as degree of polymerization.

lengths. In order to describe the molecular weight it is necessary to work with statistical mean values. Here, different approaches are possible. The simplest one is the number average molar mass M_n

$$M_n = \frac{\sum_i n_i \cdot M_i}{\sum_i n_i} \tag{3.1}$$

with n_i as the number of molecules of molar mass M_i. Additionally, it is possible to weight the mean value by the weight fraction of each chain length. This weight average molar mass M_w is defined as

$$M_w = \frac{\sum_i n_i \cdot M_i^2}{\sum_i n_i \cdot M_i} = \frac{\sum_i w_i \cdot M_i}{\sum_i w_i} \tag{3.2}$$

where $w_i = n_i \cdot M_i$ is the total mass of component i. In order to additionally quantify the distribution width of the molar masses, the ratio between M_w and M_n is defined to be the polydispersity index PDI:

$$PDI = \frac{M_w}{M_n} \tag{3.3}$$

Hence, a monodisperse system would give $PDI = 1$. While this is hardly achievable with synthetic methods (in comparison to some natural polymers such as for example DNA), a narrow distribution of the polymerization degrees is often desired in order to obtain well-defined and predictable system properties.

Another important aspect in describing polymers is the classification into different groups. Depending on the characteristic trait that is considered they are assigned to different categories. Most often they are categorized by [39]

origin: While natural polymers such as DNA or cellulose have been around long before synthetic chemistry, synthetic polymers are man-made.

structure: Depending on the architecture in which the monomers are connected, polymers can be of linear, branched, or cross-linked structure.

composition: If a polymer is composed of only one type of monomer A, it is called a homopolymer. The combination of different monomer species A and B yields to copolymers, which are differentiated by the arrangement of the different building blocks into statistical ($...AABABABBAAAB...$), alternating ($...ABABABABA...$), or block copolymers ($...AAAA - BBBB...$).

mechanical properties: Depending on their mechanical properties and the underlying molecular forces it is possible to classify into thermoplasts, elastomers, or duroplasts.

Polythiophene (PT), its processing for thin film applications, and finally its electronic and morphological properties are the center of this work. PT is a synthetic homopolymer, which additionally belongs to the class of organic conducting materials. In order to interpret and understand the results later-on, it is necessary to first give a short insight into two main physical aspects that underly its properties: polymer crystallization and the origin of conductivity in organic materials.

Just like their shorter relatives, the oligomers, polymers can have the tendency to crystallize. Moreover, they exhibit analogous crystal structures of parallel extended straight chains. In contrast to oligomers, however, solid polymers usually do not fully crystallize to form single crystals but rather stay in a semicrystalline state that is a mixture of crystalline and amorphous domains. The origin of this semicrystalline state lies in two major differences between oligomers and polymers: i) other than oligomers, polymers do not have a uniform chain length distribution, and ii) more importantly, the entanglement of the longer chains is a large energetic barrier that needs to be overcome in order to obtain a crystalline polymer. Hence, when a polymer crystallizes from an entangled melt, a separation happens between molecular parts that can be stretched out forming crystals and amorphous, strongly entangled regions. These typically contain chain bends and ends. Considering the entanglement that needs to be overcome upon crystallization it is evident that the process is not mainly governed by thermodynamics but rather by kinetics. In other words, the structures that develop fastest are not necessarily those with the lowest free energy but simply possess the fastest growth rates.

Crystallinity plays a crucial role in the properties electronic of conducting polymers. The basics of conductivity in organic systems is adressed in the next section.

3.1.1. Organic semiconductors

Organic semiconductors can be of molecular or polymeric nature. In both cases, the origin of the electronic properties follows the same basic concept that lies in the chemical structure of the materials. Conductivity is present in organic systems when the molecules are conjugated, meaning they feature alternating single and double bonds. This conjugation results in the presence of an extended π electron system, leading to an increased mobility of charge carriers through that system. Conductivity in polymers was first discovered by Shirakawa, MacDiarmi, and Heeger in 1977 and awarded the Nobel prize in chemistry in 2000. [1]

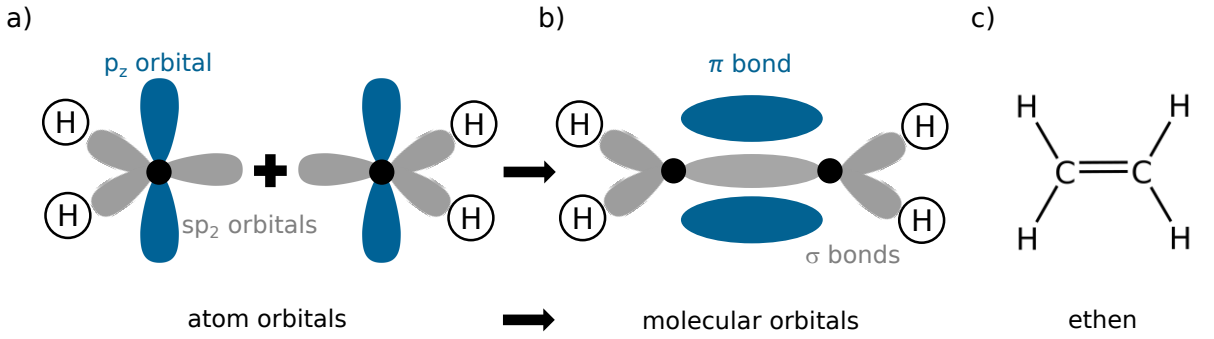

Figure 3.2.: Electron orbitals and chemical structure of ethen. a) Schematic depiction of atomic orbitals of two carbon atoms (black) after hybridization (grey: sp^2 orbitals, blue: p_z, b) formation of molecular orbitals upon bond formation (grey: σbonds, blue: πbond), c) chemical structure of ethen molecule.

Figure 3.2 exemplary depicts the formation of a π bond for the molecule ethen. When a carbon atom is not in its elemental atomic state, its 2s and 2p orbitals form hybrids in order to enable the formation of molecular bonds to other atoms. In organic semiconductors at least one of the p orbitals remains in its original state without undergoing hybridization. For creation of a double bond, such as in the case of ethen, sp^2 orbitals are formed while the p_z orbital remains. The development of molecular orbitals from the single atomic orbitals upon bond formation is often described in terms of the *linear combination of atomic orbitals* (LCAO). According to LCAO, ethen exhibits five σ bonds, one between the carbon atoms and one to each of the connected hydrogen atoms. Additionally, the non-hybridized p_z orbitals are overlapping to form a binding π (filled) and a corresponding antibinding π^* (empty) orbital. Usually, these two orbitals are less involved in the binding of two atoms and energetically closer together than for example σ and σ^* orbitals. As a consequence, they often make up the highest occupied molecular orbital (HOMO, π orbital) and the lowest unoccupied molecular orbital (LUMO, π^* orbital), respectively.

When the conjugated system consists of more atoms than in ethen, as it is the case in conjugated polymers, the π orbitals become delocalized over several atoms in the backbone, resulting in an outstretched electron system in which charge carriers are able to move. In analogy to inorganic semiconductors, the HOMO and LUMO of conducting polymers are often referred to as bands. The evolution of these bands upon increasing conjugation length (i.e. number of monomers involved in one π system) can be explained by a splitting of the energy levels due to interaction of the HOMOs and LUMOs of each subunit in the chain. The energy gap between the resulting bands is referred to as band

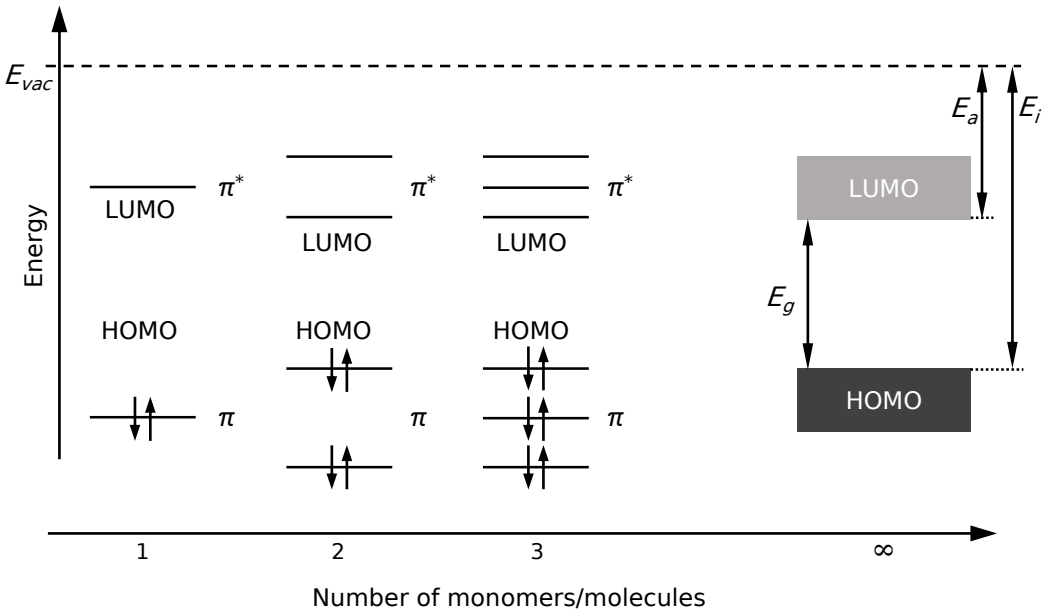

Figure 3.3.: Formation of bands in conjugated polymers upon increasing number of monomers, band structure obtained from linear combination of atomic orbitals (LCAO). HOMO and LUMO of single molecules split due to interaction with neighboring orbitals, resulting in formation of band-like structure with band gap E_g, ionization energy E_i, and electron affinity E_a with respect to energy level of vacuum E_{vac}.

gap E_g. The band gap of semiconducting polymers is usually in the range of 1.5 - 3.0 eV and hence in the energetic range of visible light. [40–42] Therefore, such polymers are very attractive for the application in optoelectronic devices such as organic solar cells or organic light-emitting diodes. The formation of electronic bands by increasing number of monomers/aggregates is schematically shown in figure 3.3.

Doping

Intrinsically, semiconducting polymers do not have a high conductivity, as the concentration of free charge carriers is low. A strong increase in the concentration is achieved by a so-called chemical doping, such as performed with iodine in the first discovered conducting polymer polyacetylene. [1] In chemical doping an oxidizing (p-doping) or reducing agent (n-doping) is added to the polymer, resulting in the extraction or addition of electrons from the backbone. [15] The electric charges are stabilized on the chain by dopant staying incorporated in the polymer matrix due to electrostatic attraction.

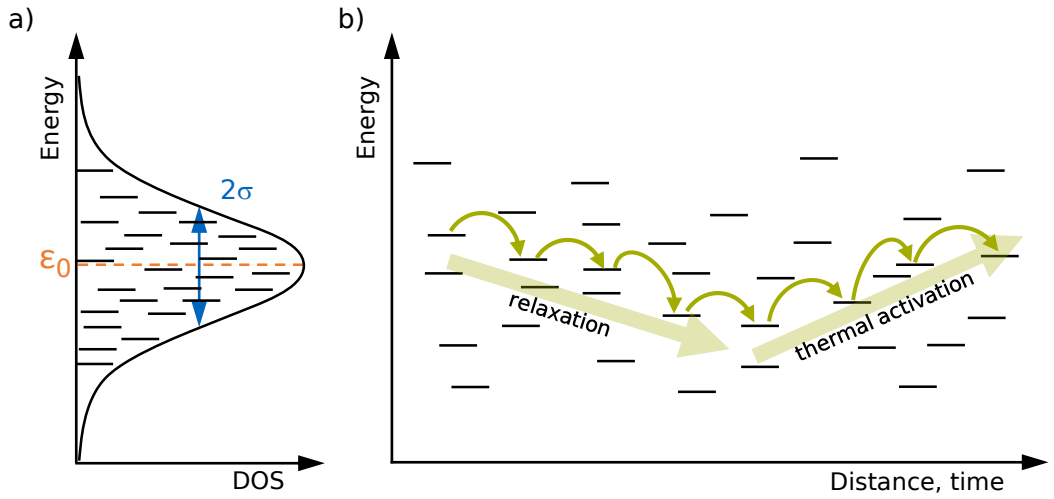

Figure 3.4.: Energetic disorder and resulting hopping transport in polymer systems. a) Statistic variation of energy levels resulting in Gaussian distribution of density of states (DOS), with mean value ϵ_0 and width 2σ. b) Hopping transport of charge carriers between energy levels with relaxation to energetically lower states at low temperature and thermally activated hopping to higher states.

Charge transport

π systems in ideally outstretched conjugated polymer chains would be delocalized along the complete backbone. However, chain torsions, bends, and chemical defects cause disruptions of the conjugation length. From the LCAO band scheme (figure 3.3) it is clear that the gap between HOMO and LUMO increases when the number of monomer units within the conjugation length is decreased. In real systems, the conjugated segments vary in their length, resulting in a statistical disorder of the respective HOMO and LUMO energy levels. The resulting density of states (DOS) can be described mathematically by a Gaussian function accounting for energetic and spacial distribution of the states as depicted in figure 3.4a. [15]

Charge carriers in such disordered polymer systems move between the neighboring states of different energy by tunneling. This mechanism is also referred to as hopping transport. [15, 43] Figure 3.4b schematically shows the hopping transport in energetically disorderd systems. A charge carrier moves from from one state to another, usually upon relaxation to energetically lower states. If additional thermal energy k_BT is provided, however, it is possible for the charge carriers to hop to states of higher energetic level. Hence, the conductivity in disordered polymers increases with temperature. Of course, an increased structural order by crystallization has a strong impact on the width of the DOS and therefore also increases the mobility of the charge carriers.

Interaction with light

Next to doping, the absorption of light also induces charge carriers in organic semiconductors. If the energy of an incoming photon exceeds the band gap E_g it can be absorbed, resulting in an electronic excitation of the molecule. The absorption is quantified by the Lambert-Beer law according to

$$I(\lambda) = I_0(\lambda)e^{-\alpha(\lambda)cd} \tag{3.4}$$

with I and I_0 as intensity of transmitted and incident light, respectively, the wavelength-dependent absorption coefficient α, the concentration of the absorbing species c, and the path length of the light through the sample d.

Upon absorption of a photon, an electron is typically excited from the HOMO to the corresponding LUMO level. The resulting electronic excitation of a molecule is described by means of the Franck-Condon principle, which is schematically depicted in figure 3.5. The graphic shows the excitation by absorption (b) as well as the subsequent relaxation by emission (a), with the potential curves of the electronic ground and first excited state, S_0 and S_1, respectively. For simplification, the shape of the potential curves is depicted as symmetric wells. As the electronic transition is much faster than the following molecular relaxation inducing a shift in the molecule's geometry, the excitation is depicted by vertical arrows at constant nuclear coordinates while the respective electronic states are shifted with respect to each other.

The respective vibronic states are depicted as horizontal energy levels. Within the approximation of an harmonic oscillator the energetic difference between the vibronic energy levels is constant. When a photon is absorbed, the molecule gets excited from the vibronic state $\nu = 0$ in the electronic ground state S_0 to a specific vibronic state $\nu = i$ in S_1. Here, the probability for an excitation to each of the respective vibrational states depends on the overlap of their wave functions, depicted in gray in the figure. If the molecule is excited to a vibronic state higher than 0, the excitation is followed by a fast molecular rearrangement resulting in a relaxation to $\nu = 0$ in S_1. From there, the molecule can relax to S_0 via photoluminescence. Again, the emission probability varies for the different vibronic states in the electronic ground state. The resulting absorption and emission spectra are a superposition of the single vibronic transitions (figure 3.5c).

Naturally, the width of the single transitions is strongly dictated by the energetic disorder in the system. For polymer systems with varying conjugation lengths and amorphous as well as crystalline sections, broad vibronic absorbance bands are typically observed which rather appear to be shoulders of a broad spectrum than single transitions. The emission spectra are usually better resolved, as excited electrons tend to diffuse to ener-

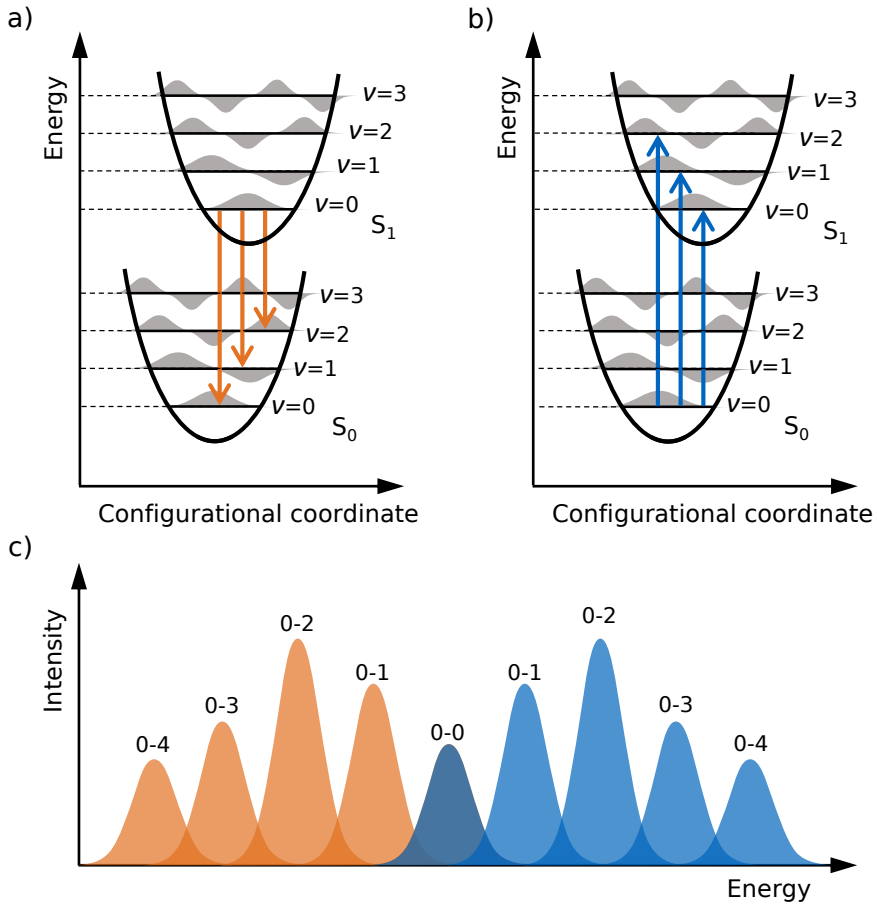

Figure 3.5.: Illustration of Franck-Condon principle. a,b) Potential energy curves for electronic ground state S_0 and first excited state S_1; sub-states within each curve represent vibronic states ν with corresponding wave functions in grey. Emission (a) and excitation (b) are depicted by vertical orange and blue arrows, respectively. Probability of the single electronic transitions depends on overlap of the wave functions of initial and final vibronic state. c) Exemplary symmetric emission (orange) and absorption spetrum (blue) with varying intensity of different vibronic transitions.

getically lower states of molecule parts with longer conjugation lengths and higher order before finally radiatively relaxing to the ground state.

Another factor that is important in semiconducting polymers is the interaction between neighboring chromophore units. Here, aggregation results in a shift of the electronic states and a coupling-induced splitting of the energy levels in the excited states. The strength of the electronic transition to each of the resulting excited energy levels is dictated by the transition dipole moment of the dimer. This transition dipole moment depends on the relative orientation of the coupling chromophores to each other. Considering the

interaction between two chromophores forming an aggregated dimer, the molecules can stack in two different geometries:

i) Aggregation in a coplanar and parallel fashion (relative transition dipole moment orientation: $\uparrow\downarrow$ or $\uparrow\uparrow$) which is also referred to as H-aggregate. In H-aggregates (from *Hypsochrom*) the excitation only happens to the higher energy level, resulting in an overall hypsochromic shift of the spectra.

ii) Aggregation in a sequential and parallel fashion (relative transition dipole moment orientation: $\rightarrow\rightarrow$ or $\rightarrow\leftarrow$) leads to the formation of a J-aggregate. Here, the transition dipole moments of the higher energy level add up to 0, which makes an excitation to that state forbidden. Hence, the transition to the lower energetic excited state results in a bathochromic shift of the spectra with respect to the single molecule absorption. The impact of the different coupling geometries in polymer semiconductors is described in much detail by Frank Spano. [44–46]

Application: organic solar cells

Semiconducting polymers are highly investigated also due to their application in organic electronic devices. Within this thesis, organic solar cells serve as an exemplary application of the *in situ* polymerized polythiophene thin films. The general working principle and resulting demands to single polymer layers are introduced here very briefly. [7, 21, 47, 48]

Organic or polymer solar cells are usually composed of a stack of several functional thin film layers. A transparent substrate covered with an equally transmissive conducting material serves as front electrode through which the light can enter the device. On top of the transparent anode an electron blocking layer is often deposited to increase the charge carrier selectivity at the anode. The heart of organic solar cells is their active layer, in which the light is absorbed and the charge carriers are generated. Its architecture and working principle are discussed in the next passage. On top of the active layer follows the cathode, that is usually a thin metal film. Here again it is possible to increase the charge carrier selectivity by insertion of a hole blocking layer between active layer and back electrode.

The active layer in organic solar cells is most often composed of a material mixture of an electron donor and an electron acceptor material. This is required due to the low dielectric constant in organic materials, which results in a strongly increased Coulomb attraction between opposite charges when compared to inorganic materials. When a photon is absorbed in the active layer, typically in the polymeric donor molecules, an exciton is created. [49] Usually, this bound electron-hole pair is too strongly bound to dissociate just by means of thermal energy. Hence, a second material is employed in the active layer. In this electron acceptor the energetic levels of HOMO and LUMO are lower

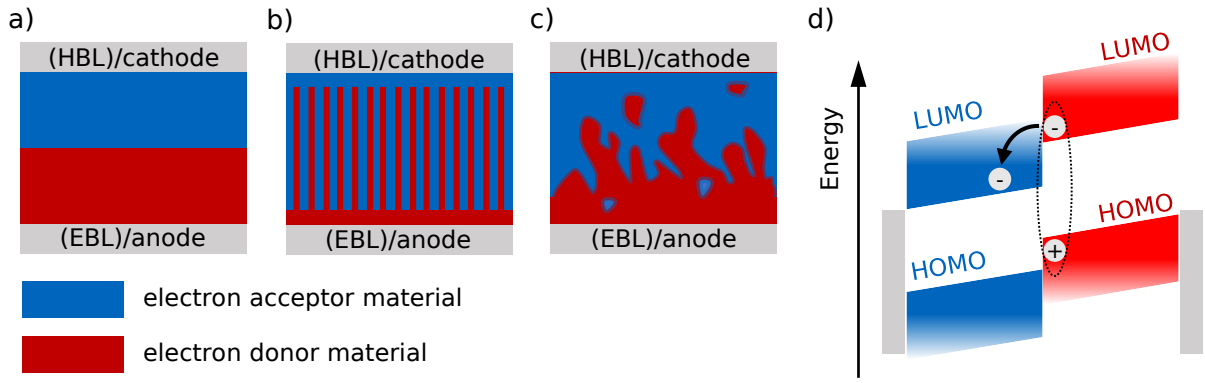

Figure 3.6.: Organic solar cell layer stacks with different active layer architectures: a) bilayer, b) interdigitated heterojunction, and c) bulk heterojunction. d) Energy offset between HOMO and LUMO of donor and acceptor material enabling the splitting of an exciton.

as compared to the ones of the donor, enabling a splitting of the exciton by a transfer of the electron (see figure 3.6d). However, the lifetime and resulting diffusion length of an exciton are very limited (typically on the order of 10-30 nm [50]), which creates the need of a nanostructured active layer with small structure sizes of the intermixed materials. If an exciton does not reach the donor-acceptor interface within its lifetime, the electron and hole recombine resulting in a decrease in the solar cell current.

Hence, the active layer architecture is usually designed in order to increase the interface between the two materials and enable short travel distances for the charge carriers. Figure 3.6 schematically shows three different geometries. In a bilayer device (figure 3.6a) flat layers of donor and acceptor are simply stacked on top of each other. Here, the interfacial area is naturally small. Moreover, a trade-off in the layer thicknesses is necessary in order to increase the amount of light absorbed (thick layers) and the charge carriers to reach the respective interfaces despite the low mobility in the organic materials (thin layers). The resulting efficiency in bilayer solar cells is therefore often limited in the current generated. In an interdigitated heterojunction (figure 3.6b) pillars or lamellae of the donor material are created by help of physical methods such as nano imprint lithography. Afterwards, the empty channels are backfilled with the acceptor material. The radii or thicknesses of these structures is desired to be of the order of the exciton diffusion length, in order to maximize the current yield. However, a large scale production of such small structures is complicated and expensive, creating the need for a more feasible approach to manufacture a nanosized morphology. In a bulk heterojunction structure (figure 3.6c) the active layer is a percolating network of interdigitated donor and acceptor domains. This structure is obtained by a solution-based processing of the two materials from one blend solution. During thin film fabrication a partial phase separation on the nanometer scale creates the

random morphology. Due to the insolubility of polythiophene, however, only bilayer solar cells are fabricated in the framework of this thesis.

3.2. Polymerization of semiconducting polymers

The *in situ* polymerization of unsubstituted polythiophene is the center of this work. Therefore it is necessary to take a look at the chosen reaction mechanism as well as the special requirements for enabling a successful synthesis during thin film fabrication.

The polymerization of five-membered heterocycles such as thiophene or pyrrole is usually performed employing an oxidative reaction mechanism. [27–29] The initiation step of such reaction is the activation of the respective monomer molecules resulting in the formation of a radical cationic species. The necessary removal of an electron from the monomer is achieved by either electrochemical or chemical means. Electrochemical polymerizations are performed in three-electrode cells, in which the monomer is dissolved in the electrolyte solution and subsequently oxidized at the anode surface. Here, the anodes additionally serve as substrates for the film deposition, as the insoluble polymer films precipitate on the electrode surface. [29,30] Chemical oxidative polymerizations on the other hand employ a second reactant, namely an oxidizing agent that activates the monomers by chemical oxidation. Typically, metal ion salts are employed as oxidants. Nevertheless, the general polymerization mechanism for both approaches remains the same.

Figure 3.7 exemplary depicts the mechanism of the bithiophene (BT) polymerization using an Fe^{3+} salt as oxidant, as this is the educt combination employed within this work. But, as already stated before, it is analogously true for the oxidative polymerization of other five-membered heterocycles by either the electrochemical or chemical approach. [30, 32, 51]

The polymerization is initialized by oxidation of the aromatic monomer molecule, here BT, by a redox reaction with the oxidizing agent. When two of the formed chemically highly active radical cations meet, they dimerize upon formation of a carbon-carbon bond. Here, α-coupling is more probable than bond formation at the β-position due to a higher unpaired electron density at that position. Nevertheless, β-coupling becomes more likely when the chains get longer and the radical electron becomes more delocalized within the molecule. [28, 52] The splitting-off of two protons leads to the neutralization of the oligomer molecule, which hereby also obtains its aromaticity.

In the subsequent chain growth the just introduced steps are repeated for the addition of every monomer unit to the polymer chain. Both, the already existing longer chain and the monomer need to be oxidized by an Fe^{3+} ion before the formation of a new covalent bond is possible. This results in a stoichiometric molar ratio of 1:2 between monomer

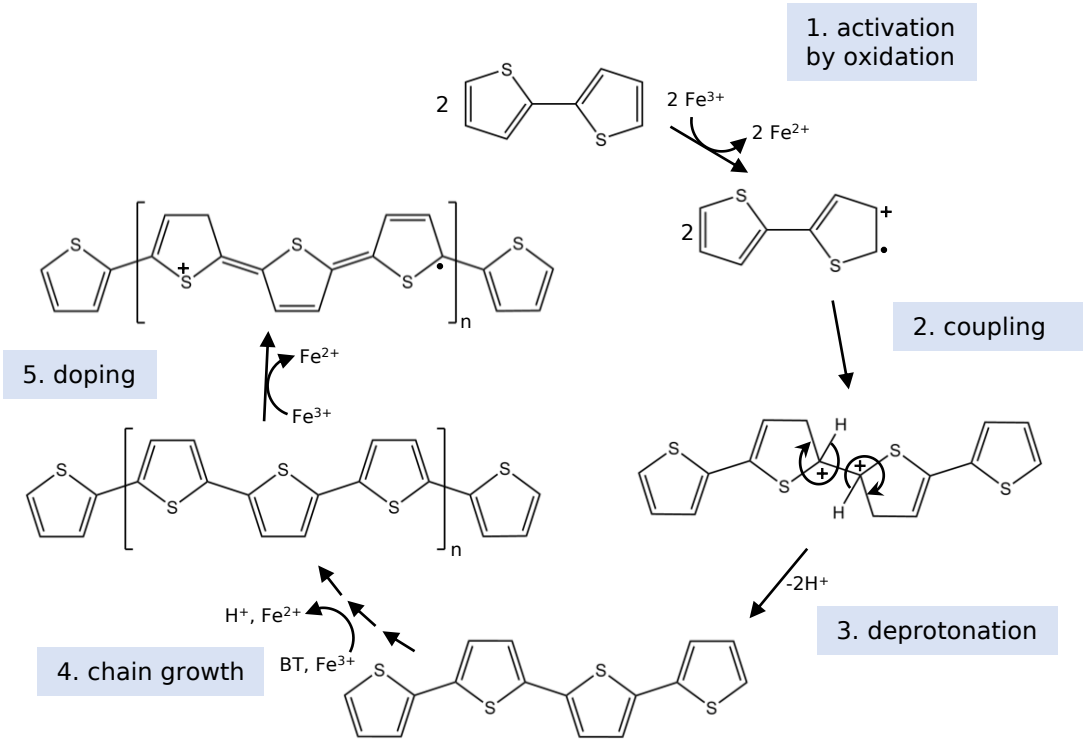

Figure 3.7.: Reaction mechanism of oxidative polymerization of bithophene using Fe^{3+} as oxidizing agent. 1. Activation of bithiophene (BT) by Fe^{3+} to radical cation followed by 2. dimerization through α-coupling and 3. deprotonation to aromatic oligomer. 4. The ongoing polymerization follows the same basic principle of activation by oxidation, bond formation by radical coupling, and finally deprotonation at each newly formed bond. 5. Finally, oxidation of already existing chains by excess Fe^{3+} leads to chemical doping.

and oxidizing agent for the polymerization reaction alone. If the oxidant is employed in excess, however, an additional oxidation of the already existing polymer chains can be achieved. This results in the presence of unbound charge carriers in the polymer and is therefore referred to as chemical doping, as discussed in section 3.1.

This doping reaction has a strong impact on the structure of the polythiophene chains, which is shown in figure 3.8. Due to the removal of electrons from the aromatic system, the charge distribution along the chain is significantly changed. [53, 54] The undoped, semiconducting chain features carbon-carbon single bonds between the thiophene rings, while a higher electron density is found within the rings. This is also referred to as benzoid structure and results in a high flexibility of the polymer chain, as torsions around the single bonds possess low energetic barriers. Upon oxidation, however, the electronic structure is changed strongly with the bonds between the rings obtaining a double-bond

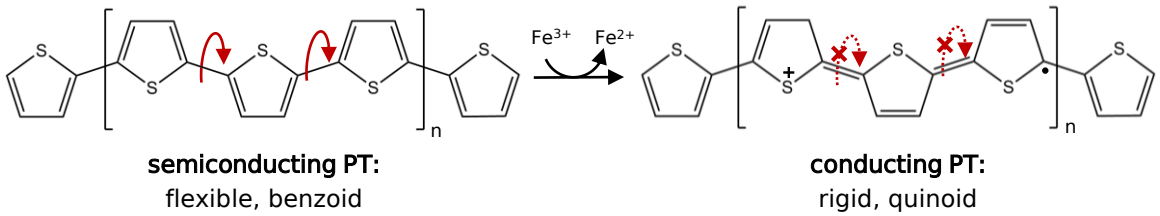

Figure 3.8.: Structural impact of doping on polythiophene. Left: Undoped, semiconducting PT chain in its flexible, benzoid form with torsion possible around the C-C single bonds between the thiophene rings (red arrows). Right: Doped, conducting PT chain after further oxidation. Rigid, quinoid structure prevents rotation due to existence of C=C double bonds between the thiophene rings.

character. Hence, the chain stiffness is strongly increased with a decreased probability of ring torsions. Additionally, the charges on the chain are stabilized by electrostatically bound anions, typically the anions of the oxidizing agent. In the formation of a solid polymer structure, these remain incorporated in the polymer matrix, thereby also changing the polymer morphology. [55]

In situ polymerization: metastable reaction mixtures

For fabrication of insoluble polymer thin films, such as unsubstituted polythiphene, it is necessary to perform the polymerization reaction directly on the substrate. This is achievable by application of an electrochemical approach, in which the polymer is formed directly on the anode. Depending on the application an upscaling of this method is anyhow not easily possible, as the substrate is required to be conducting and stable upon flow of electrical current. A chemical *in situ* polymerization on the other hand does not require a special substrate. Here, the monomer and oxidant are deposited to the substrate either subsequently or simultaneously by means of evaporation or solution.

A very convenient solution-based approach is the application of metastable reaction mixtures. [32, 56] These are solutions containing both, the monomer and the oxidizing agent, without an onset of the polymerization reaction as long as the concentration is sufficiently low. The polymerization starts when the metastable mixture is deposited to the substrate and the reactant concentrations are significantly increased upon solvent evaporation. Moreover, a thin film fabrication with such approach is not linked to the usage of a specific processing technique. Hence, lab-scale techniques such as spin coating are just as feasible as for example large-scale printing.

The required metastability of the solution is obtained by choosing an oxidizing agent whose oxidation potential is close to but still lower than that of the monomer. [32] The

chemical equilibrium of the initial redox reaction is therefore thermodynamically controlled and defined by the Nernst equation according to

$$E = E_0 + \frac{RT}{zF} ln \frac{[Ox]}{[Red]} \tag{3.5}$$

with E_0 and E as the (standard) redox potential, R the ideal gas constant, F the Faraday constant, and $[Ox]$ and $[Red]$ as the concentrations of oxidized and reduced species, respectively. Due to the proximity of the redox potentials of the two reactants an equilibrium of the redox reaction is already achieved when only a minor fraction of the monomers have been oxidized. As a consequence, the following steps are strongly controlled by the overall concentration of the solution. While it is still in a dilute regime, the probability of two radical cations actually colliding and forming dimers is relatively low. Hence, no polymerization is observed in the solution. Upon solvent evaporation after deposition, however, the concentration increases rapidly, leading to a strong increase in the polymerization rate. Of course, the uptake of monomer radical cations in the polymerization also leads to a shift of the redox equilibrium and an ongoing activation of more molecules. Moreover, the oxidation potential of the formed oligothiophenes decreases with chain length, additionally leading to increased polymerization rates during the course of the reaction.

3.3. X-ray scattering

As introduced in the previous sections, the morphology plays a crucial role in semiconducting polymer thin films. More precisely, two different length scales are of special interest when it comes to the performance in final devices. First of all, the polymer aggregation and crystallinity have a strong impact on the intermolecular interaction and the resulting electronic characteristics such as charge carrier mobility. Additionally, also larger morphological features such as the extension and spatial distribution of crystalline domains or the phase separation between two different material types can play a significant role.

X-ray scattering is a tool that enables the investigation of the volume morphology in polymer films on different length scale regimes. In this work, grazing incidence techniques (section 3.3.2) are employed which are differentiated into wide-angle and small-angle scattering. The general concept of X-ray scattering is briefly introduced in section 3.3.1.

3.3.1. Basic principle

X-ray scattering experiments exploit the interaction of electromagnetic waves with electrons in the medium they are traveling through. The photons with wave vector $k = |\vec{k}_i| = \frac{2\pi}{\lambda}$

and wavelength λ are described by an electromagnetic wave with respective electric field vector

$$\vec{E}(\vec{r}) = \vec{E}_0 \cdot e^{i\vec{k}_i\vec{r}} \tag{3.6}$$

with $\vec{r}$ as position vector and $\vec{E}_0$ as amplitude and polarization of the electric field. The propagation of the electric field through a medium is described in terms of the Helmholtz equation [57]

$$\Delta\vec{E}(\vec{r}) + k^2 n^2(\vec{r}) \cdot \vec{E}(\vec{r}) = 0. \tag{3.7}$$

Here, $n(\vec{r})$ denotes the refractiv index of the medium, which for X-rays is typically slightly less than unity and defined as

$$n(\vec{r}) = 1 - \delta(\vec{r}) + i\beta(\vec{r}) \tag{3.8}$$

with dispersion δ and absorption β. Both contributions are wavelength-dependent and can be written as

$$\delta(\vec{r}) = \frac{\lambda^2}{2\pi}\rho(\vec{r}) \tag{3.9}$$

and

$$\beta(\vec{r}) = \frac{\lambda}{4\pi}\mu(\vec{r}). \tag{3.10}$$

$\rho = r_e\rho_e$ is the scattering lentgh density (SLD) of the medium, which depends on the material's electron density ρ_e and the electron radius r_e $= 2.814 \cdot 10^{-5}$ Å. μ denotes the linear absorption. In the X-ray wavelength regime the dispersion is commonly several orders of magnitude larger than the absorption. For that case, and in homogeneous media, the critical angle α_c can be approximated by

$$\alpha_c \approx \sqrt{2\delta}. \tag{3.11}$$

The respective difference in n between two phases *1* and *2* is referred to as contrast and given by

$$\Delta\delta^2 + \Delta\beta^2 = (\delta_1 - \delta_2)^2 + (\beta_1 - \beta_2)^2. \tag{3.12}$$

Hence, the contrast between two phases and therefore a scattering at their interface strongly depends on their difference in SLD and respectively electron density.

Scattering from a plane sample is depicted in figure 3.9, with specular scattering in 3.9a and diffuse scattering in 3.9b. In both cases, an incident beam $\vec{k_i}$ hits the sample under the incident angle α_i. Under specular conditions the resulting reflected beam $\vec{k_f}$ exits the sample under a final angle α_f which is equal to α_i and does not leave the xz-plane of the incoming beam. The momentum transfer of the scattered beam is given by the scattering vector

$$\vec{q} = \vec{k_f} - \vec{k_i}. \tag{3.13}$$

The magnitude of incoming and outgoing wave vector are $k = 2\pi/\lambda$. In diffuse scattering the exiting beam additionally possesses an angle Ψ_f in the xy-plane.

3.3.2. Grazing-incidence scattering

The diffuse scattering from thin films is usually measured in grazing-incidence to increase the X-ray path length through the sample and thereby increase statistics as well as signal intensity. In order to achieve that, a very shallow incident angle of $\alpha_i < 1$ is chosen which results in a large illuminated footprint on the sample. The experimental geometry is depicted in figure 3.9b. The incident beam hits the sample under a fixed angle, while the diffuse scattering is recorded on an area detector. Each pixel on the detector can be assigned a value of the scattering angles α_f and Ψ_f, respectively. These can then be transformed into scattering vectors according to

$$\vec{q} = \frac{2\pi}{\lambda} \begin{pmatrix} cos(\Psi_f)cos(\alpha_f) - cos(\alpha_i) \\ sin(\Psi_f)cos(\alpha_f) \\ sin(\alpha_i) + sin(\alpha_f) \end{pmatrix} \tag{3.14}$$

Depending on the sample-detector distance (SDD) a different range of scattering angles and therefore q-range is accessible. Consequently, two different techniques are distinguished and to be introduced in the following: grazing-incidence wide-angle X-ray scattering (GIWAXS, small SDD) and small-angle scattering (GISAXS, larger SDD).

GIWAXS

Wide-angle scattering under grazing incidence enables the analysis of crystalline structures in thin films. For illustration, the scattering happening at the atoms is often depicted as reflection at the crystal lattice planes, such as shown in figure 3.10a. The inter-plane distance in one direction of the unit cell is referred to as d_{hkl}, leading to a difference

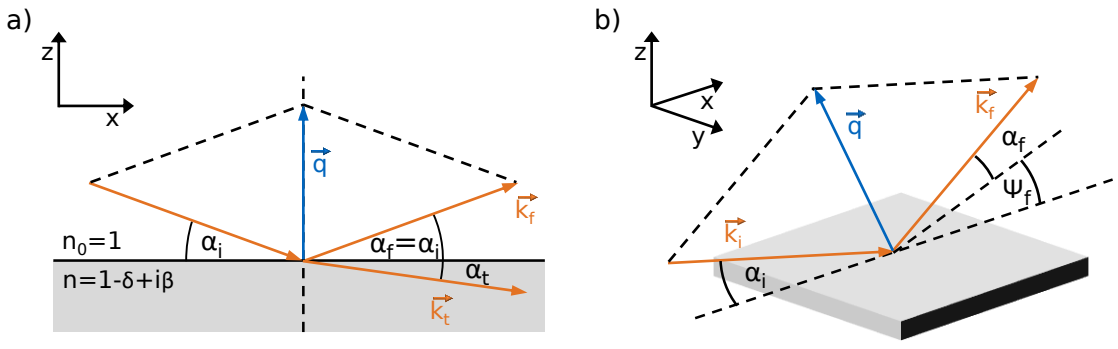

Figure 3.9.: Geometry of specular (a) and diffuse (b) scattering. Under specular conditions incoming beam is reflected with $\alpha_f = \alpha_i$, while diffuse scattering happens under additional angle Ψ_f in xy-plane.

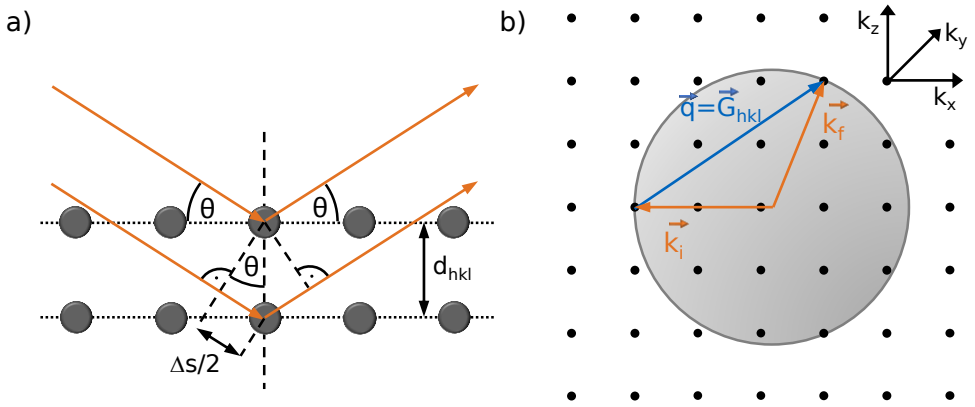

Figure 3.10.: a) Bragg condition: X-ray diffraction from crystal lattice planes with distance d_{hkl}. Beam impinges and exits lattice under angle Θ. Constructive interference if path difference of adjacent waves equals an integer multiple of the wavelength. b) Ewald sphere: Constructive interference occurs where sphere of radius $|\vec{k_i}|$ intersects with reciprocal lattice points.

in beam path length of Δs. Depending on the incident angle Θ, the interference of the scattered X-rays is either constructive or destructive. Constructive interference takes place, when the Bragg condition is fulfilled:

$$n\lambda = 2d_{hkl}sin(\Theta). \tag{3.15}$$

This principle, which is true for diffraction under specular conditions, can be further expanded to diffraction from multiple crystallites in different orientations. For that purpose, each scatterer in the system is considered as the origin of an elementary wave. This results in constructive interference when the scattering vector $\vec{q}$ matches a reciprocal lattice vector $\vec{G}_{hkl}$. Since only elastic scattering takes place, the momentum is conserved and $|\vec{k_i}| = |\vec{k_f}|$. This concept is conveniently visualized by the Ewald sphere shown in figure 3.10b. In this representation the reciprocal lattice points are superimposed by a circle of radius $|\vec{k_i}|$, that displays where momentum is conserved. A diffraction pattern is only observed, where this Ewald sphere touches lattice points.

A closer look at the Ewald construction reveals that for a given incident wave vector $\vec{k_i}$, the scattered wave vector cannot contain a k_z component without contributions in x or y direction. This is always the case for GIWAXS measurements, where scattering in the specular plane (at $k_y = 0$) is necessarily a combination of k_z and k_x. Consequently, a part of the q-range in vertical direction is inaccessible in GIWAXS. This is geometrically accounted for by insertion of the so-called 'missing wedge'. Further corrections such as accounting for radiation polarization and solid angles of the different pixels are discussed in much detail in literature. [58, 59]

The diffraction peaks allow the extraction of different quantities characterizing the crystalline domains in the sample. As already discussed above, the peak position in q-space is inversely proportional to the distance d_{hkl} in the crystal lattice. Moreover, the peak amplitude is related to the amount of crystals. The Scherrer equation enables the extraction of a lower limit of the crystallite size D_{hkl} from the full width at half-maximum (FWHM) $\Delta(2\Theta_{hkl})$ according to

$$D_{hkl} = \frac{K\lambda}{\Delta(2\Theta_{hkl})cos(\Theta_{hkl})} \tag{3.16}$$

with wavelength λ and Scherrer constant $K \approx 0.93$. [60] A transformation of the equation to reciprocal space finally gives

$$D_{hkl} = \frac{2\pi K}{\Delta q_{hkl}}. \tag{3.17}$$

While peak broadening due to instrumental settings or paracrystalline disorder especially in organic systems are not accounted for in such an approach, the Scherrer relation gives a good estimate of the lower limit of the average crystal size in the sample.

GISAXS

Grazing-incidence small-angle X-ray scattering enables the investigation of structures larger than typical crystal lattices. With GISAXS it is possible to get an insight on domain sizes of a few nanometers up to micrometers, which typically covers the relevant structure sizes in for example organic solar cells. It is possible to investigate the structures and their distribution in vertical and lateral direction. Other than in GIWAXS, the contributions of q_x to $\vec{q}$ in vertical direction are neglected due to the very small scattering angles. In the framework of this thesis, GISAXS is employed to investigate the porosity and its origin in polythiophene thin films.

A very prominent feature in vertical direction is the Yoneda peak. [61] This enhanced scattering intensity arises where the scattering angle α_f matches the critical angle α_c of the material. As introduced in equation 3.11, the critical angle depends on the SLD and accordingly the density of the film. By extracting the latter from the Yoneda peak position, it is possible to calculate the film porosity ϕ as

$$\phi = 1 - \frac{\rho_m}{\rho_t} \tag{3.18}$$

with ρ_m and ρ_t as measured and theoretical densities of the densely packed bulk material.

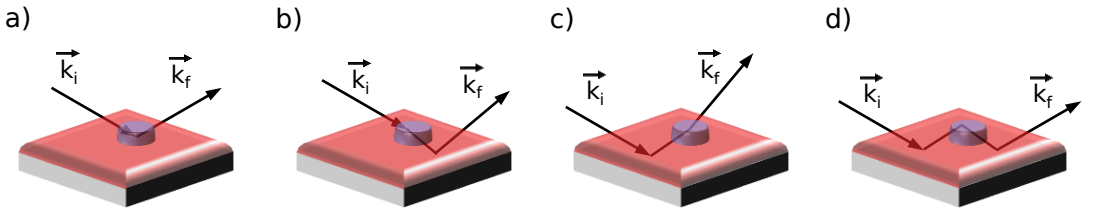

Figure 3.11.: Schematic representation of all contributions within DWBA framework: a) directly scattered beam, b) first scattered then reflected beam, c) first reflected then scattered beam, d) reflected-scattered-reflected beam.

Diffuse scattering originates from lateral structures in the thin films. These may be domain sizes in a material composition or, as in this work, the distribution of pores in a polymer matrix. Additionally, the measurement geometry results in reflections at the sample or substrate surface that contribute to the scattering pattern. These effects can be accounted for in the distorted wave Born approximation (DWBA). [62,63] Within this framework, the incoming wave hitting on an object is approximated as a combination of direct and previously reflected waves. The same holds for the exiting wave, which might be directly scattered from the object, scattered and subsequently reflected, or reflected prior and after the scattering event. Figure 3.11 schematically shows all the cases considered in DWBA. The final scattering intensity is a superposition of all four cases.

In order to reduce the computing power it is possible to reduce the two-dimensional GISAXS data to horizontal line cuts for analysis. These integrations are typically performed at the Yoneda positions of the respective materials for an enhanced intensity and an increased material sensitivity. The effective interface approximation is applied for simplification, considering only lateral correlations in the system with q_z as a constant.

The diffuse scattering signal in the horizontal cuts is modeled by assuming different sets of objects distributed laterally in the film. Each object class is assigned a certain size and shape, the form factor $F(\vec{q})$, which is the Fourier transform of the electron density of the selected object. Additionally, the form factor is combined with a spatial arrangement of the objects, the structure factor $S(\vec{q})$. In the case of N identical objects with given size, arrangement, and random orientation, the diffuse scattering factor [64]

$$P_{diff}(\vec{q}) \propto NS(\vec{q}) \; |F(\vec{q})|^2 \tag{3.19}$$

is a direct measure of the recorded scattering intensity. In the analyses performed in this thesis, the form factor is of cylindrical shape and contains all the DWBA contributions introduced earlier on. The structure factor is approximated as a one-dimensional paracrystalline lattice without orientation. In such, the objects are distributed periodi-

cally but with only short range order. Upon increasing distance from the lattice origin the positions become more disordered. If several form and structure factors are employed, the different objects are combined in the local monodisperse approximation (LMA), in which every object only scatters with other objects from the same class of structure and form factor. The final intensity is the sum of all the contributing factors.

4. Characterization methods

The aim of this thesis is to investigate thin polythiophene films, with special focus on the influence of synthetic parameters on morphology and (opto)electronic properties. For that purpose, a combination of several characterization techniques is employed. These methods are introduced in this chapter, giving an insight on data collection and analysis as well as device specifications. The films are investigated by spectroscopic methods (section 4.1), regarding their electronic properties (section 4.2), and finally on a structural level (section 4.3).

4.1. Spectroscopic characterization

The spectroscopic behavior of semiconducting polymer films gives an insight on the molecular properties of the polymer chains. The intrinsic energetic landscape can be investigated just as aggregation properties and polymer crystallization. Moreover, the composition of a material mixture can be determined by the compound specific light-interaction. Within this thesis, UV/Vis absorbance (section 4.1.1) and photoluminescence spectroscopy (section 4.1.2) are employed, which are introduced in the following two sections.

4.1.1. UV/Vis spectroscopy

UV/Vis spectroscopy allows to study the wavelength-dependent absorption of light by for example polymer films. Within this thesis, two different types of UV/Vis spectroscopic investigations are performed, each with a different focus.

For analysis of polymer aggregation and band gap determination static measurements are performed. These experiments are executed using a Lambda 650S from PerkinElmer, which allows to detect the light transmitted through the sample or reflected by it inside an integrating sphere (Spectralon R highly reflective 150 mm spherical chamber). This way, scattered light is taken into account. A combination of a deuterium (UV range) and a tungsten halogen lamp (visible and near-infrared) provides a wavelength range of 250 nm - 900 nm. The light source is switched at 320 nm. The measurements are performed

at scanning rates of 267 nm·min^{-1} and with 1 nm slits. Prior to the sample measurements, an autozero calibration is performed. The employed glass substrates are not measured individually and subtracted from the spectra, as they do not exhibit an absorbance beyond 330 nm.

For transmission measurements, the sample is placed in front of the integrating sphere. This way, only the transmitted light reaches the detector. If the sample is placed behind the sphere, only scattered and reflected light are detected. The measured transmission $T(\lambda)$ and reflection $R(\lambda)$, which are both defined as the fraction of respective detected to initial light intensity, are combined for calculation of the absorbance $A(\lambda)$ by

$$A(\lambda) = 2 - log_{10}\left(\frac{T(\lambda)}{100 - R(\lambda)} \cdot 100\right) \tag{4.1}$$

with $T(\lambda)$ and $R(\lambda)$ given out by the instrument in percentage. According to the Lambert-Beer law (equation 3.4) the absorption coefficient can be extracted form the absorbance according to

$$\alpha(\lambda) = \frac{A(\lambda)}{d \cdot log_{10}(e)} \tag{4.2}$$

with the film thickness d. $\alpha(\lambda)$ can be exploited for determination of the band gap E_g of the investigated material. This is done with regards to the Tauc equation

$$(\alpha E)^n = B(E - E_g) \tag{4.3}$$

with exponent $n = 1/2$ for allowed indirect or $n = 2$ for direct transitions, constant B for different transitions, and energy of the light E. [65,66] Plotting $(\alpha E)^n$ against E and linearly extrapolating the low energy flank gives the band gap as x-axis intercept.

Furthermore, the shape of the absorption spectra gives an insight on the inter- and intramolecular interactions in the polymer thin films. Within this thesis, an interpretation of the respective spectra with respect to polymer crystallinity and chromophore coupling is done mostly in a qualitative way, due to a lack of information on the absorbance of all-amorphous polythiophene.

Time-resolved transmission measurements are performed with a Nanocalc-XR-NIR purchased from Ocean Optics with the software OceanView. Here, white light is guided to the sample by flexible optical fibers incorporated into a printing setup, as presented in more detail in chapter 8. The data are resolved to wavelength-specific transmission by the software. Due to the chosen setup, reflection from the sample surface cannot be taken into account and the absorbance is simply calculated by

$$A(\lambda) = 2 - log_{10}(T(\lambda)). \tag{4.4}$$

Here, a background calibration initially determines the light intensity of the environment, as the measurement is not performed in a closed setup. The obtained spectra are employed for determination of solution and film composition during *in situ* polymerization.

4.1.2. Photoluminescence spectroscopy

The photoluminescence (PL) response of a polymer film after electronic excitation gives additional information on energetic landscape and type of chromophore interaction in the polymer films. In PL measurements, the material is initially excited with photons of energy slightly higher than the corresponding absorbance maximum. The resulting emission arises from two different mechanisms: phosphorescence and fluorescence. The prior is a slow relaxation process upon a change in spin multiplicity and is not of relevance in this work. Fluorescence, however, is a rapid process from an excited singlet to the electronic ground state of the molecules. This typically happens after the electrons have already lost energy by diffusion to more crystalline parts of the polymer, as introduced in chapter 3.1.1.

The emission spectra presented in this thesis are recorded in an LS55 fluorescence spectrometer by PerkinElmer controlled with the corresponding software FL-Winlab. The sample is illuminated for excitation by a Xenon discharge lamp with a pulse FWHM shorter than 10 µs. The scan rate is 500 nm·min^{-1}, the slit width 10 nm. Since the measurements are performed in reflection and glass gives a broad luminescence response, the thin films investigated in PL are prepared on silicon wafers as substrates.

4.2. Electronic characterization

An electronic characterization of the investigated polythiophene films is performed in order to proof their applicability in the active layers of organic solar cells and measure the impact of synthetic parameters on their conductivity and charge carrier mobility. Polymer hole mobilities are determined by means of a technique called *metal-insulator-semiconductor-charge extraction by linearly increasing voltage* (MIS-CELIV) which is introduced in section 4.2.1. Electrical conductivities are measured by four-point probe measrurements (section 4.2.2). Finally, the solar cell performance is analyzed by current-voltage characterization as presented in section 4.2.3.

4.2.1. MIS-CELIV

Metal-**I**nsulator-**S**emiconductor-**C**harge **E**xtraction by **L**inearly **I**ncreasing **V**oltage (MIS-CELIV) is an experimental measurement technique for determination of vertical charge carrier mobilities in semiconducting organic thin films. [67,68] Depending on the employed device architecture it enables the separate quantification of electron and hole mobilities, respectively. Within this thesis, however, only hole mobilities of polythiophene thin films are determined and therefore only the corresponding functional layer stack is introduced.

The device architecture for determination of hole mobilities is depicted in figure 4.1. The polythiophene layer is sandwiched between the conducting ITO covered glass substrate and a thin insulating layer. On top, a metal electrode is deposited by evaporation. For measuring the mobilities, the device is connected to a wave generator (LeCroy WaveStation 3082: Waveform generator), an oscilloscope (Teledyne Lecroy Wavejet touch 354, 500 MHz Oscilloscope 2GS/s), and a current lock-in amplifier (FEMTO DHPCA-100) as depicted in the schematic circuit diagram in the figure.

In the first step of the measurement routine, an offset voltage is applied that results in the enrichment of positive charge carriers at the polymer-insulator interface. Afterwards, the voltage is increased linearly allowing the holes to move away from the interface and out of the layer stack. The time they take to travel through the semiconducting layer is referred to as transit time t_{tr}, with $t = 0$ being the start of the current increase. The current increases beyond the displacement current j_0, which is a product of the device capacitance and the slope of the applied voltage, until it finally depletes. When the device

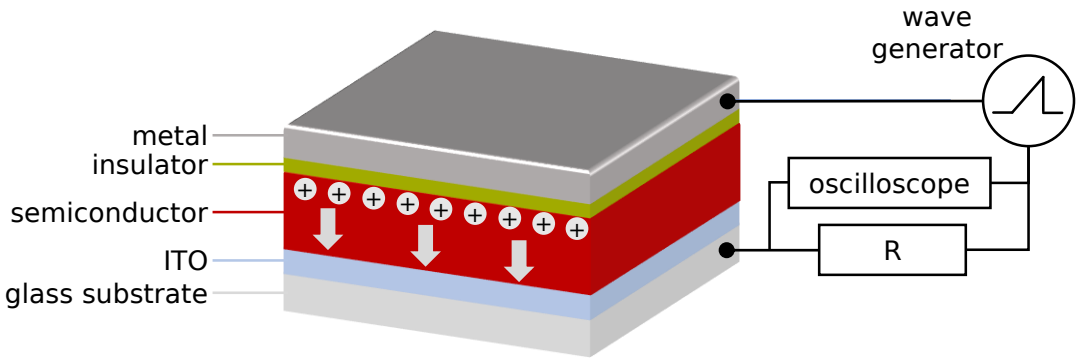

Figure 4.1.: Illustration of MIS-CELIV measurement setup. Device layer stack with insulating layer sandwiched between semiconductor and metal, ITO-covered glass serves as conductive substrate. Holes are initially accumulated at semiconductor-insulator interface and subsequently extracted by linearly increasing the applied voltage.

is depleted, the current density again decays to j_0. The mobility μ can be calculated according to

$$\mu = \frac{2d_s^2}{At_{tr}^2 \cdot \left(1 + \frac{\epsilon_s d_i}{\epsilon_i d_s}\right)} \tag{4.5}$$

with layer thicknesses d_s and d_i of semiconductor and insulator, respectively, voltage slope $A = dU/dt$, and dielectric constants of semiconductor ϵ_s and insulator ϵ_i. The transit time corresponds to the time at which the current density j is the twofold displacement current density j_0 by

$$t_{tr} = t_{2j_0} \cdot \frac{4}{\pi}. \tag{4.6}$$

For each sample, the mobility is determined for different offset voltages and finally averaged. A detailed description on the measurement setup and protocol are given in the Bachelor's thesis of Salma Mansi. [69]

4.2.2. Four-point probe measurements

Four-point probe measurements allow to measure the sheet resistances of conducting thin films, from which the lateral conductivities can be extracted.

The measurements presented in this thesis are performed with a measurement setup by Cascade Microtech (C4S-54/5) that consists of four tungsten carbide probes with radii of 125 µm spaced at a distance of 1 mm. The penetration of the tips into the film is reduced by springs in the setup. Upon sweeping the current through the outer two tips, the voltage drop between the inner tips is recorded. The sheet resistance is extracted from the slope of the linear current-voltage curve.

The electrical conductivity σ of samples with arbitrary shape is given by

$$\sigma = \frac{1}{\rho} = \frac{I}{V} \cdot \frac{1}{2\pi l F} \tag{4.7}$$

with ρ the resistivity, l the distance between the measurement tips, and F the correction factor for finite sample thickness. In thin film geometry, the film thickness is much smaller than the tip distance. Therefore, the sheet resistance can be expressed as

$$R_\square = \frac{1}{\sigma d} = \frac{\rho}{d} = \frac{I}{V} \cdot \frac{\pi}{ln(2)}. \tag{4.8}$$

As a result, the sheet resistance is independent of film thickness. It is given in dimensions of $\Omega/\square$ or $\Omega/\ ^2$ ('ohm per square').

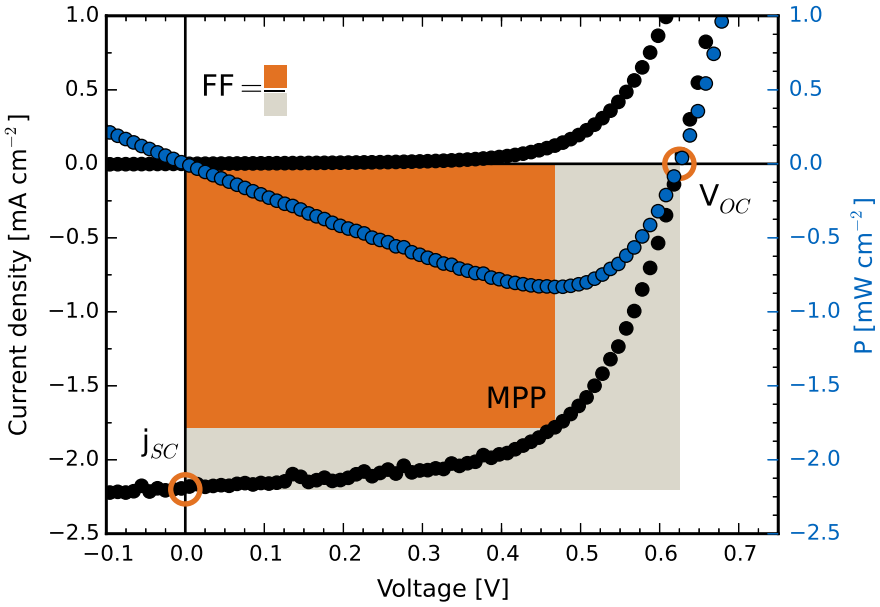

Figure 4.2.: Exemplary current-voltage curve of organic solar cell with key parameters highlighted. Light (bottom black curve) and dark I-V curve (top black curve) obtained for the device with and without AM1.5 illumination, respectively. Resulting power-voltage curve (blue) with its absolute maximum value at maximum power point (MPP). j_{SC} and V_{OC} as well as calculation of resulting fill factor (FF) are indicated.

4.2.3. I-V characterization

Solar cells are typically characterized by measuring their current-voltage (I-V) curves. For that purpose, the electric current density is measured as a function of applied voltage. This is done under illumination of the solar cell as well as in dark.

The solar cells are illuminated by a solar simulator (LOT0108, LOT-QuantumDesign GmbH) which emits the air mass 1.5 global solar spectrum (AM1.5, 100 mW·cm^{-2}). The solar simulator is equipped with an electrical shutter for switching between measurements with (light curves) and without illumination (dark curves). The illuminated pixel area is controlled by covering with an aluminum mask to 0.1 cm^2. The current-voltage curves are measured by connection of the solar cell with a Keithley 2400 source meter that is controlled by a self-developed LabView program. The resulting current is recorded upon sweeping the voltage from -1 V to 1 V in steps of 0.01 V with a delay of 1 ms. In order to obtain the current density, the current is normalized by the active (illuminated) pixel area.

Figure 4.2 shows exemplary I-V curves in light and dark with the extractable solar cell parameters. From the light curve it is possible to extract the short circuit current density

j_{SC} at the intercept with the voltage axis ($V = 0$) and the open circuit voltage V_{OC} at zero current ($j = 0$). The point, at which the power density $P = j \cdot V$ reaches its absolute maximum is referred to as maximum power point (MPP). From these parameters, it is possible to calculate the fill factor FF of the solar cell according to

$$FF = \frac{j_{MPP} \cdot V_{MPP}}{j_{SC} \cdot V_{OC}}. \tag{4.9}$$

The FF can nicely be illustrated as the ratio between the areas of the rectangles spanned by the current density and voltage at the MPP (grey), and j_{SC} and V_{OC} (orange), respectively. The power conversion efficiency η of the device is defined as the ratio of extracted power P_{out} to incident power P_{in} ($100\,\mathrm{mW{\cdot}cm^{-2}}$), according to

$$\eta = \frac{P_{out}}{P_{in}} = \frac{V_{OC} \cdot j_{SC} \cdot FF}{P_{in}}. \tag{4.10}$$

4.3. Structural characterization

The aim of this thesis is to investigate the impact of several synthetic parameters on the properties of *in situ* polymerized PT thin films, and how the observed changes are correlated to the film morphology. Hence, the film structure needs to be investigated on different length scales, requiring the combination of complementary measurement techniques.

Optical microscopy (section 4.3.1) and scanning electron microscopy (section 4.3.2) are employed for investigations of sample surfaces, with respect to film quality and homogeneity. Polymer film thicknesses are obtained by performing profilometric measurements (section 4.3.3). And finally, grazing-incidence X-ray scattering experiments (section 4.3.4) give an insight on the inner structure of the polymer films, by investigating crystallinity as well as morphology.

4.3.1. Optical microscopy

Optical microscopy is employed for the analysis of film surface structure and homogeneity on microscopic length scales. A Leica DM2700 is combined with a charged coupled device (CCD) camera (Leica MC170HD) in this work. The recorded images are processed by means of the software ImageJ. [70] Real-space distances are calculated from the images according to objective characteristics given in table 4.1.

Table 4.1.: Pixel sizes of objectives with different magnification from Leica DM2700.

magnification	pixel size [µm]
1.25x	11.7 ± 0.1
5x	2.9 ± 0.1
10x	1.5 ± 0.1
20x	0.7 ± 0.1
50x	0.3 ± 0.1
100x	0.2 ± 0.1

4.3.2. Scanning electron microscopy

Scanning electron microscopy (SEM) enables the investigation of solid-sample surfaces with sub-nanometer resolution. Hence, the resolution is strongly increased when compared to optical microscopy. This results from the application of electrons instead of optical light, which can have much smaller wavelength. In this work, SEM images are recorded of polythiophene film surfaces.

The electrons in an SEM are typically generated by either an electrostatic field or from a hot filament. They are accelerated with a voltage of several kV and focused on the sample surface by help of magnetic and electrostatic lenses. The resulting electron beam is focused onto the sample surface, which emits secondary electrons. These are detected by the detector. Usually, the sample surface is scanned with the beam in a line-wise fashion. The intensity of the secondary electrons at every position depends on the material and the sample-detector distance. Therefore, different materials and topographic changes are detected, enabling the mapping of the sample surface.

Within this thesis, an NVision40 field emission SEM from CarlZeiss AG is employed for measurements on the polymer thin film. To prevent an electric charging of the samples, the films are prepared on conducting ITO coated glass substrates.

4.3.3. Profilometry

Profilometry enables a fast recording of height-profiles with a sub-micrometer resolution. This is exploited for measuring polymer film thicknesses as explained in the following. The films are scratched by help of a syringe needle and a height profile is measured across the scratch by a profilometer. During the scanning procedure, the sample is placed on a horizontal stage, which is equipped with an additional actuator to ensure a smooth movement below the profilometer tip. The scanning direction is always perpendicular to

the scratch direction. Initially, the diamond tip is lowered to the sample at constant force controlled by an inductive tip actuator. Upon moving of the sample, a one-dimensional height profile is recorded.

The profilometer employed in this thesis is a DektakXT by Bruker Nano Surfaces Division, with a diamond tip radius of 2 µm. The tip presses onto the sample surface with a weight of 1 mg. For measurements of polythiophene film thicknesses, the *in situ* synthesis is performed on ITO-covered glass substrates. This way, the prior application of an adhesive polymer layer is not required. ITO, in comparison to polymers, is assumed not to be affected by a careful removal of the PT during scratching.

4.3.4. Grazing-incidence X-ray scattering

Grazing-incidence X-ray scattering (GIXS) is a powerful technique enabling structural investigations in organic thin films covering a large range of analyzable length scales. Morphological studies with GIXS can provide information on crystallinity, crystal orientation, and morphology without destruction. For crystallographic information, large scattering angles (i.e. small real space distances) are detected by means of grazing-incidence wide-angle X-ray scattering (GIWAXS). Scattering at small angles (GISAXS) arises from larger structures. Figure 4.3 depicts the general setup for both measurement geometries. A theoretical introduction to the physical background is given in section 3.3.

The scattering data discussed in this thesis are obtained in three different experimental setups or configurations:

i) static GIWAXS for analysis of polythiophene (PT) crystal structure and orientation (chapter 7), performed at beamline 7.3.3 at the Advanced Light Source (ALS) [71]

ii) time-resolved GIWAXS for tracking of the film formation during *in situ* polymerization (chapter 8), performed at the SIRIUS beamline at Soleil Synchrotron [72]

iii) static GISAXS measurements for analysis of PT film porosity (chapter 9), likewise measured at the SIRIUS beamline.

In all three experiments the scattering pattern is detected on a Pilatus 1M area detector, which consists of two columns of five detector modules each. These are separated by the detector gaps, that are visible as vertical and horizontal lines of no intensity in figure 4.3. The overall area of the detector is 168.7 x 179.4 mm^2 with 981 x 1043 pixels. To prevent over-illumination, parts of the detector are shielded by a beamstop to cover areas of very high intensity (such as the direct and specular beam).

Specifications on data recording and analysis are presented for each of the respective experiments separately in the following.

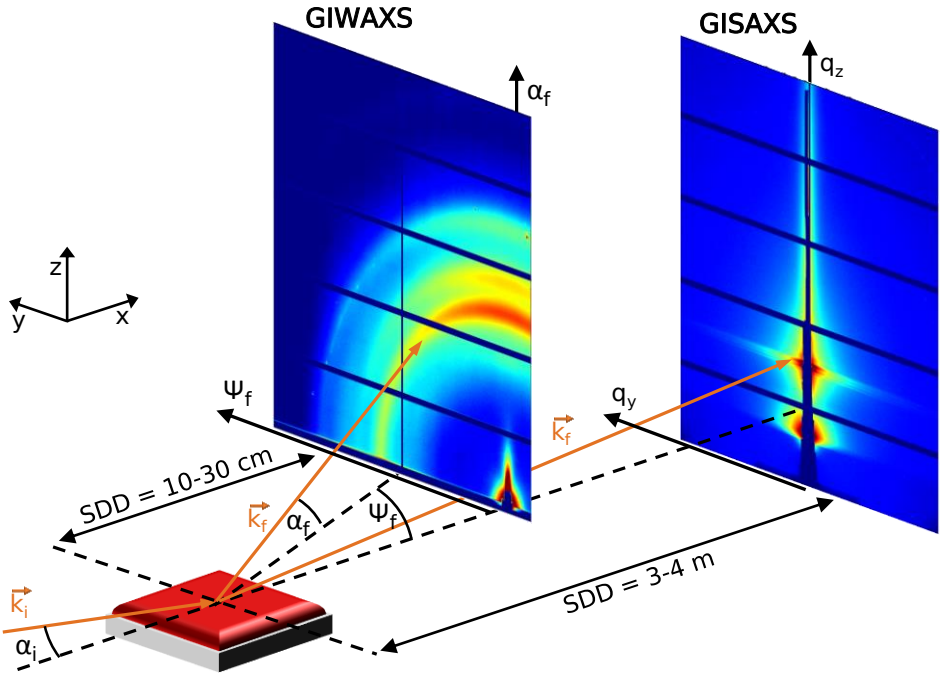

Figure 4.3.: Experimental setup for grazing-incidence scattering experiments. The incoming beam $\vec{k_i}$ impinges the sample under incident angle α_i, scattered beam $\vec{k_f}$ with scattering angles α_f and Ψ is detected on area detector. Depending in the sample-detector distance (SDD), either wide (GIWAXS) or small scattering angles (GIWAXS) are detected.

Static GIWAXS

Static GIWAXS measurements on polythiophene thin films are performed at beamline 7.3.3 at the ALS, with an X-ray energy of 10 keV (wavelength $\lambda = 1.24$ Å). The incident angle α_i is set to 0.16°, which is between the critical angles of polymer and substrate, respectively. This way, a penetration of the glass substrate is reduced to a minimum, preventing additional scattering signals on the detector.

The data are corrected prior to analysis, as described in section 3.3. These corrections and all further data reduction are performed applying the software GIXSGUI. [58] The data are reduced to one dimensional intensity profiles. In order to analyze the Bragg peak positions, intensities, and widths, the inensity is radially integrated in vertical direction between azimuthal angles of $0° < \chi < 15°$, to access the scattering profile close to q_z. Horizontal intensity profiles are obtained by radial integration at angles $75° < \chi < 85°$. The respective areas are illustrated by orange arcs in the corrected scattering pattern in figure 4.4a. For a detailed analysis of the crystal orientation, the peak intensity is azimuthally integrated, as depicted by the green tube in figure 4.4a. All extracted intensity profiles

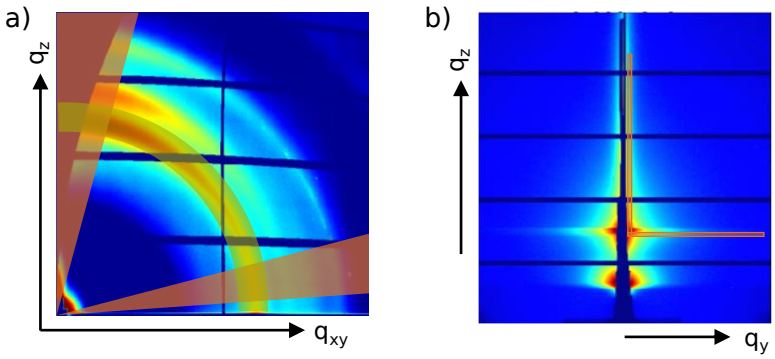

Figure 4.4.: Data reduction for extraction of one-dimensional intensity profiles from scattering pattern. a) GIWAXS data after geometrical correction, vertical and horizontal intensity profiles are obtained by radial integration of within for azimuthal angles highlighted by orange arcs. Orientation analysis is done by azimuthal integration as depicted by green ring. g) GISAXS data are reduced by integrating the intensity in thin slices in either vertical or horizontal direction, as illustrated by thin orange boxes.

are analyzed and fitted, taking into account adequate background functions, by means of self-written Python scripts. Details on the chosen mathematical fitting functions are given in chapter 7.

Time-resolved GIWAXS

Time-resolved GIWAXS measurements are performed at the SIRIUS beamline at Soleil Synchrotron, with an X-ray energy of 10 keV (wavelength $\lambda = 1.24$ Å). Scattering pattern are recorded during *in situ* polymerization in a custom slot-die coater, with an α_i of 0.2° at with a time resolution of 10 images per second. Analogously to the data treatment for static GIWAXS measurements, the data are corrected and reduced to one-dimensional intensity profiles. Due to the isotropy of the scattering signals, the intensity profile is not created in vertical and horizontal direction separately, but the intensity is integrated over a larger range of azimuthal angles $30° < \chi < 70°$. Angles close to 0° and 90° are left out in order to avoid beamstop artifacts. This is described in more detail in chapter 8. Finally, the data are fitted by self-written Python scripts to follow the crystal growth during film formation.

Static GISAXS

Static GISAXS measurements are performed at the SIRIUS beamline at Soleil Synchrotron, with an X-ray energy of 8 keV (wavelength $\lambda = 1.55$ Å). In comparison to GIWAXS, the sample-detector distance is much larger, enabling the detection of struc-

ture sizes between a few up to several hundreds of nm. A helium-filled flight tube is placed between the detector and the sample, in order to reduce air scattering contributions on the long path.

For analysis, line integrals are taken in vertical and horizontal direction, respectively, as indicated by the thin orange boxes in figure 4.4b. The vertical integral is taken directly next to the vertical detector gap at very low q_y. Horizontal integrals are typically taken at the Yoneda positions of the material of interest for increased scattering intensity and material selectivity. However, within this thesis some integrations are performed at high q_z to increase the intensity of certain scattering features, as described in chapter 9. The data reduction is performed with the software package DPDAK from DESY. [73] Custom made macros are used to model the horizontal intensity profiles, assuming a combination of up to three cylindrical form factors with Gaussian size distribution and 1d paracrystals as corresponding structure factors. The modeling is performed in the framework of the Distorted Wave Born Approximation (DWBA) and the local monodisperse approximation (LMA), which assumes scattering only from objects of same size. More details on the applied model are given in section 3.3.2.

5. Experimental section

Within this thesis, an *in situ* polymerization technique for polythiophene (PT) thin films is developed. The investigated and discussed films are prepared with varying parameters, in order to gain an insight on the film formation processes. Section 5.1 introduces all employed basic chemicals and polymers involved in the sample preparation. The general routine established for PT thin film fabrication and solar cells is introduced in section 5.2. Finally, the experimental specifications for each of the chapters 6-9 are summed up in section 5.3.

5.1. Materials

In the following, the specifications of all employed basic chemicals and polymers are presented. Their chemical structures are given in figure 5.1.

2,2'-Bithiophene (BT)

2,2'-Bithiophene (α-bithiophene) is employed as monomer for the oxidative polymerization of polythiophene. It is purchased from Alfa Aesar and processed without further purification. Due to its low melting point (33 °C) it is stored at 4 °C. The molar mass of BT is 166.26 g·mol^{-1}, its oxidation potential is 1.31 V (SCE). [30, 74]

Phosphomolybdic acid (PMA)

Phopshomolybdic acid hydrate ($12MoO_3{\cdot}H_3PO_4{\cdot}xH_2O$, 1825.25 g·mol^{-1}) has been introduced as oxidizing agent for the *in situ* polymerization of PT by Bravo-Grimaldo et al. [32] Its oxidation potential is 0.36 V (SCE) and therefore sufficiently low to oxidize BT for polymerization. [75] The here employed PMA is obtained from Sigma Aldrich and used without further purification.

Iron p-toluenesulfonate (FeTos)

Iron(III) p-toluenesulfonate ($(CH_3C_6H_4SO_3)_3Fe{\cdot}6H_2O$, 677.52 g·mol^{-1}) has been introduced by Bayer in 1988 for the *in situ* polymerization of poly(3,4-ethylenedioxythiophene) (PEDOT) from solution. [76] The oxidation potential of the Fe^{2+}/Fe^{3+} redox couple is 0.77 V. [77] In comparison to more common iron(III) salts, however, the tosylate is soluble in organic solvents such as alcohols and therefore suitable for the *in situ* synthesis of organic polymers. FeTos is purchased from Sigma Aldrich and employed without further purification.

Phenyl-C61-butyric acid methyl ester (PCBM)

In the organic solar cells presented in this thesis phenyl-C61-butyric acid methyl ester is employed as electron acceptor material. The soluble derivative of the C_{60} fullerene has its HOMO and LUMO level at -6.0 V and -4.3 V, respectively. [78] PCBM is purchased from 1-Material and employed without further purification.

Poly(3,4-ethylenedioxythiophene):polystyrene sulfonate (PEDOT:PSS)

PEDOT:PSS is a blend of the semiconducting PEDOT, a polythiophene derivative, and the nonconducting counter ion PSS, which are combined to achieve a water soluble material composition. Because of their high light transmission and hole conductivities, PEDOT:PSS thin films are often employed as electron blocking layers in organic solar cells. [47] The employed dispersion of PEDOT:PSS in water is obtained from Ossila (Al 4083, PEDOT:PSS ratio 1:6) and stored at 4 °C. Before processing, the dispersion is sonicated for 10 min and subsequently filtered with a PVDF filter with pore size of 0.45 µm to remove larger aggregates.

Adhesive layers

Since the *in situ* polymerized PT does not provide a sufficient adhesion to glass and silicon, the respective substrates are coated with adhesion layers first. [79] For this purpose, thin films of *polypropylene* (PP, chlorinated, $M_w = 100000$ g·mol^{-1}, 26 wt% chlorine loading, Sigma Aldrich) or *polystyrene sulfonate* (PSS, $M_w = 18300$ g·mol^{-1}, $PDI = 1.13$, counter ion: Li^+, Polymer Standards Service GmbH Mainz) are deposited prior to the actual *in situ* synthesis. Both polymers are electrically insulating and transparent and should therefore not influence the performed analyses. The materials are employed as purchased without purification.

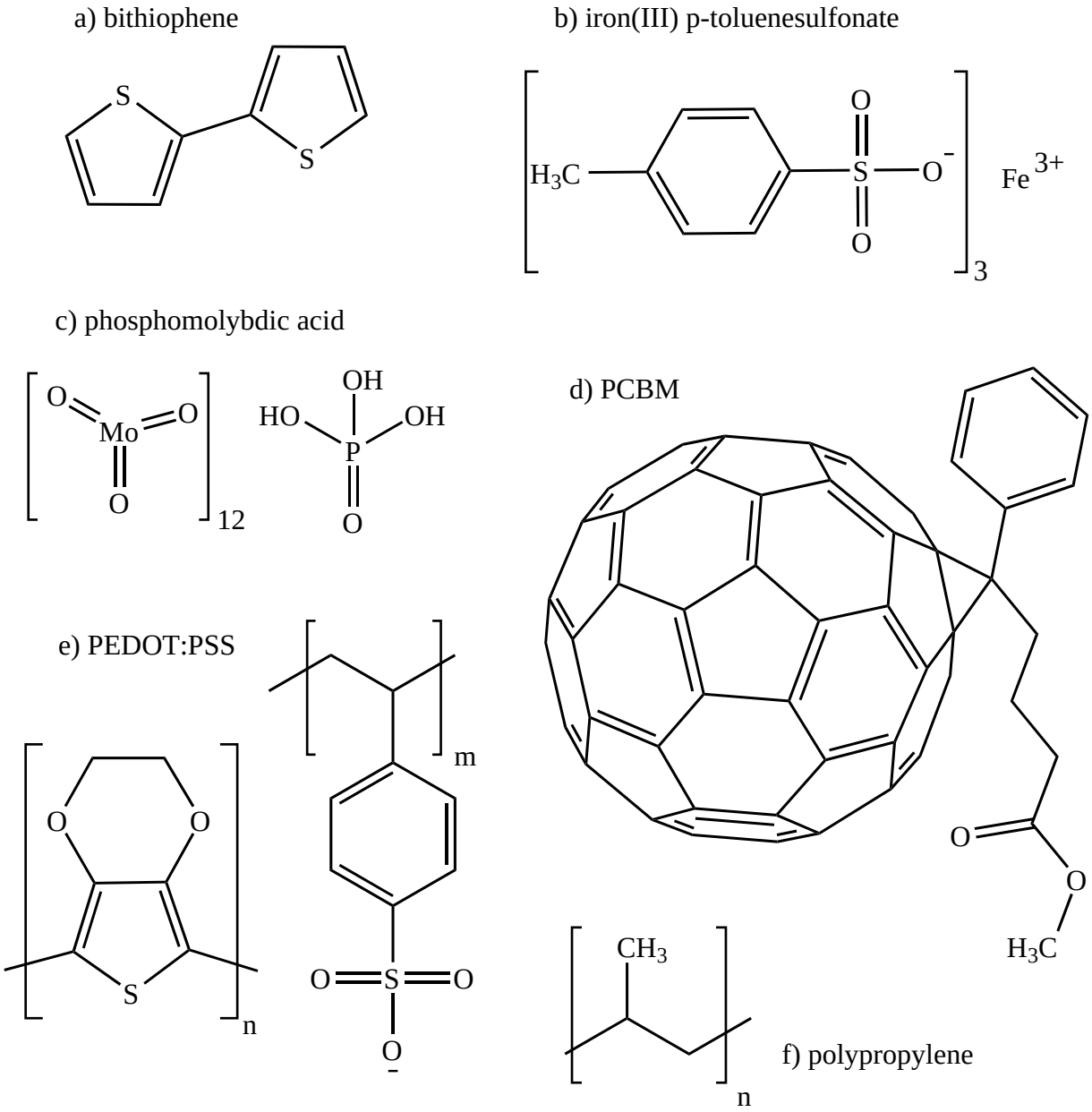

Figure 5.1.: Chemical structures of the basic chemicals and polymers employed in this work.

Solvents

Acetonitrile (HPLC grade, Sigma Aldrich) is employed as solvent for the polymerization of PT with PMA as oxidizing agent and moreover for rinsing the films.

1-Propanol ($\geq$ 99.5 %, Roth) serves as solvent for the polymerization of PT with FeTos as oxidizing agent.

1-Propanol (anhydrous, Sigma Aldrich) is employed as solvent for the *in situ* polymerized

PT films discussed in chapter 9. For additional drying, it is stored over molar sieve in nitrogen atmosphere for at least 12 hours.

Ethanol (technical grade) is employed to rinse the PT films after fabrication and to dedope them to obtain semiconducting PT.

Chlorobenzene ($\geq 99.5\,\%$, Roth) is employed for dissolving the adhesive polymers, PP and PSS, as well as the electron acceptor PCBM.

The solvents are employed as purchased and without additional purification, unless specifications are given above.

Substrates

Glass slides from Carl Roth (76x26x1 mm^3) are employed as standard transparent substrates and cut into the desired size with a glass cutter.

Silicon wafers from Si-Mat (p-doped, (100)-orientation) are cut into the desired size with a diamond cutter and serve as substrates for photoluminescence measurements.

ITO (indium tin oxide) coated glass purchased from Solems serves as standard transparent electrode in the discussed organic solar cells. The 20x20x1 mm^3 are coated with a 100 nm layer of ITO with a sheet resistance of 25-35 $\Omega \cdot sq^{-1}$.

All substrates are cleaned prior to their utilization. The details of the cleaning routines are given in section 5.2.1.

5.2. General sample preparation

The sample preparation is divided into the subsections substrate pre-treatment, *in situ* polymerization/thin film deposition, and solar cell fabrication.

5.2.1. Substrate pre-treatment

Prior to the thin film deposition the substrates are cleaned to remove residual dirt from the fabrication or storage and to obtain reproducible surface properties. In the framework of this thesis, three different cleaning routines or combinations thereof are applied:

Acid bath: The substrates are placed in a mixture of deionized water, hydrogen peroxide solution (H_2O_2, 30 %), and concentrated sulfuric acid (H_2SO_4) (respective volume fractions 1:1.6:3.7) at 80 °C for 15 min. Afterwards, they are rinsed in deionized water and spin-dried in a spin coating setup.

Organic cleaning: The substrates are subsequently immersed in baths of Alconox® in deionized water (10 g·L^{-1}, Sigma Aldrich), ethanol, acetone, and 2-propanol (all organic solvents in technical grade). In each step, the bath is placed in an ultrasonic bath for 10 min at 40 °C. Finally, the samples are blown dry in a nitrogen flow.

Oxygen plasma: The samples are placed on a glass plate in between the electrodes of a plasma oven (SmartPlasma from plasma technology GmbH). Inside the chamber the pressure is reduced to 0.3 mbar and an oxygen plasma is generated for 3 min.

Additionally, glass and silicon substrates need to be pre-coated with an polymer layer to enhance the adhesion of the *in situ* polymerized polythiophene films. The coating polymers (PP or PSS) are dissolved in chlorobenzene (15 g·mol^{-1}) and applied by spin coating (3000 rpm, 60 s). Finally, the samples are placed on a heating plate at 150 °C for 10 min to remove potential solvent residuals that could influence the adjacent polymerization reaction.

5.2.2. *In situ* polymerization: PT thin film deposition

The *in situ* polymerization is performed from metastable reaction mixtures of monomer BT and respective oxidizing agent (PMA or FeTos). For preparation of the precursor solution, the two components are first dissolved separately in two stock solutions to enable a complete dissolution. Afterwards, they are combined at the molar ratio desired for the respective experiment. Thereafter, the metastable solution is processed within a few minutes after the mixing to prevent an early reaction onset in the solution. The thin film deposition is performed by either *spin coating* or *slot-die printing*, a short insight on the two fabrication methods is given later on in this section.

The polymerization reaction takes place during the deposition, i.e. while the solvent of the solution evaporates. While the reaction with PMA in acetonitrile starts already at room temperature, the polymerization with FeTos is initiated by heating the substrate holder (spin coater chuck or printing stage) to an elevated temperature. For 1-propanol as solvent, the substrate needs to be heated to at least 85 °C. Especially for spin coating it is necessary to ensure a complete drying of the film before the spinning is stopped in order to obtain a smooth polymer film in the end. After the polymerization, the films are immersed in rinsing baths of ethanol or acetonitrile to remove the residual educt molecules and undesired byproducts and to receive pure polythiophene films in conducting (acetonitrile bath) or semiconducting state (ethanol bath) for 30 min. Subsequently, the samples are carefully blown dry in a nitrogen flow. Finally, the semiconducting PT films are thermally annealed by placing the substrates on a heating plate for 10 min at ambient atmosphere.

In the following, the technical details regarding the deposition techniques spin coating and slot-die coating are introduced.

Spin coating

Spin coating is a technique widely employed for the preparation of thin homogeneous films on a laboratory scale. It is most convenient for the fabrication of films on small substrates and from solutions with volatile solvents. The substrate is centrally fixed on the rotation chuck by means of small pins. For application of the film, the solution is dispersed over the whole sample surface followed by a fast rotational spinning at chosen speed in revolutions per minute (rpm), acceleration rate and time period. Initially, the centrifugal forces spin off excessive solution. Thereafter, the remaining solvent evaporates, leaving a thin, solid film. In general, the obtained film thickness depends on the applied rotational speed as well as the concentration and molar mass of the solute. In an *in situ* polymerization, however, the achieved film thickness is additionally governed by the reaction kinetics and the resulting strong change in the solution properties (e.g. viscosity) during the reaction process.

In the framework of this thesis a conventional spin coater (E441 from Ossila) is adapted by exchanging the original rotation chuck by one with a built-in heating plate. The chuck is itself composed of Teflon in order to maintain the necessary solvent resistance. A 3 mm thick copper plate is screwed on top of the chuck to serve as heating plate. Underneath lies a Peltier element (Quick-Cool QC-127-1.0-3.9) that electrically heats the copper plate. The temperature is maintained during the actual spinning by application of carbon brushes as sliding contacts. In order to control the temperature, an infrared temperature sensor (IRC-PC21MT-0 from ASM GmbH) is placed above the chuck. In order to reliably detect the temperature, the emissivity of the copper is increased by painting it black regularly. The sensor is connected to a temperature control unit consisting of a PID modulator (UR3274S1 from Wachendorff Prozesstechnik GmbH & Co. KG) and a solid-state relay (A-senco SSR-500), which switch the Peltier element on/off after processing the sensor signal. The current needed for the heating is provided by a connected power supply.

The prototype of this heatable rotation chuck as well as the necessary temperature control unit have been designed and implemented by Leonhard Hofbauer within the framework of his Bachelor's thesis. [80]

The *in situ* polymerization is performed by spin coating the metastable reaction mixture at 2500 rpm for 60 s. When FeTos is employed as oxidizing agent the chuck is heated to 90 °C if no other information is given.

Slot-die coating

A lab-scale printer with a slot-die head is employed for deposition of the reaction mixture for the time-resolved scattering experiments presented in chapter 8. The printer has been designed especially for implementation into synchrotron beamlines in order to follow the morphology evolution during film fabrication. Detailed technical information on the printer setup is found in the publication by Pröller et al. [81]

For printing the metastable reaction mixture the substrate is initially placed under the print head on the motorized, heated sample stage. The height from substrate surface to print head, the gap clearance, is an essential parameter for adjusting the amount of solution deposited and is therefore controlled via a 10x-magnification optical objective connected to a CMOS camera and additionally through a force sensor connected to the vertical motor responsible for regulating the print head height. The solution is fed to the print head by a syringe pump at a chosen pump rate. Upon pumping the solution through the print head a meniscus is forming in the gap clearance. By moving the sample stage with a horizontal motor underneath the print head, the meniscus is transferred onto the sample. The resulting film thickness is governed by several parameters such as the concentration of the solution, the height of the gap clearance and the resulting meniscus volume, the pumping rate, and the printing speed at which the substrate moves underneath the head.

The *in situ* polymerization discussed in chapter 8 is performed with a substrate to print head distance of 0.3 mm, the solution is fed to the print head at $0.25\,\mathrm{mL{\cdot}min^{-1}}$, and the printing speed is set to $20\,\mathrm{mm{\cdot}s^{-1}}$.

5.2.3. Solar cell fabrication

The solar cells presented and discussed in this thesis are prepared in several subsequent steps. In the following, the optimized parameters of the fabrication routine are presented. Figure 5.2 graphically summarizes the order of the sample preparation steps.

In a first stept, a 0.5 cm wide stripe of the ITO is chemically removed from the glass substrates by etching with zinc powder and hydrochloric acid (figure 5.2b). This is necessary in order to prevent short circuits through the thin films when the final solar cells are characterized. After rinsing away potential residuals of the etching chemicals the substrates are cleaned organically and by oxygen plasma treatment according to the routines described in section 5.2.1.

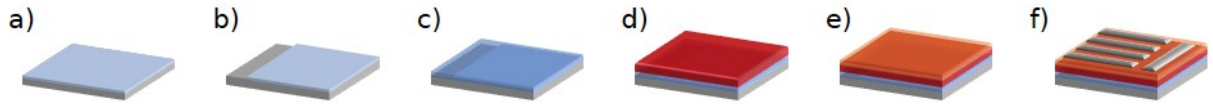

Figure 5.2.: Illustration of solar cell preparation steps: ITO covered glass substrates (a) are partly etched and subsequently cleaned (b). Thereafter, an electron blocking layer of PEDOT:PSS is spin coated onto the transparent back electrode (c). The active layer is deposited in a bilayer geometry of *in situ* polymerized PT as electron donor (d) and PCBM as electron acceptor on top (e). Finally, aluminum electrodes are thermally evaporated as back electrodes (f).

PEDOT:PSS serves as electron blocking layer in the chosen solar cell layer stack (figure 5.2c). It is deposited onto the substrates immediately after the oxygen plasma treatment by spin coating at 3000 rpm for 60 s. Afterwards, the films are thermally annealed at 150 °C for 10 min at ambient atmosphere to remove all traces of water from the hygroscopic PEDOT:PSS layer. The active layer of the solar cells is deposited in two subsequent steps, as the insolubility of the *in situ* polymerized PT requires a bilayer geometry. PT is deposited by performing an *in situ* polymerization according to the description given in section 5.2.2 (figure 5.2d). After rinsing the films in ethanol, they are thermally annealed at 200 °C for 10 min. Thereafter, the electron acceptor layer PCBM is applied by spin coating from a solution in chlorobenzene (13.5 g·mol^{-1}) at 1000 rpm for 60 s (figure 5.2e). As last layer, the aluminum (ChemPUR, 99.99 % purity) contacts are thermally evaporated at pressures below 10^{-5} mbar using a CREAMET 301 V2 evaporation system from Creative Vakuumbeschichtung GmbH. The thickness of the aluminum layer (100 nm) is adjusted by a deposition controller (SQC-122c from Sigma Instruments). As a last step, the whole stack is thermally annealed at 100 °C for 10 min in inert nitrogen atmosphere.

5.3. Measurement specifications

Within the framework of this thesis, four different projects are presented and discussed. The respective specifications on sample preparation and characterization techniques are given in the following sections.

Experimental details on chapter 6

The aim of this investigation is to establish an *in situ* polymerization for semiconducting PT thin films for application in organic solar cells by adapting a literature-known synthesis. The polymerization of PT according to Bravo-Grimaldo et al. is performed from metastable reaction mixtures of bithiophene (BT) and phosphomolybdic acid hydrate (PMA). [32] The glass substrates are acid-cleaned and coated with polystyrene

sulfonate (PSS) as adhesive layer. The polymerization is performed by spin coating a solution of 0.10 mol·L^{-1}BT and 0.12 mol·L^{-1} PMA in acetonitrile. Afterwards, the films dry for 30 minutes at ambient conditions and are subsequently rinsed in either ethanol or acetonitrile. Thermal annealing is performed on a heat plate for 10 minutes in ambient atmosphere. For an optimization of the post-treatment the annealing temperature is varied between 100 °C and 250 °C. Thereafter, all films are annealed at 200 °C.

The synthesis is later on adapted by exchanging the original oxidizing agent with iron(III)p-toluenesulfonate hexahydrate (FeTos). The solution contains 0.10 mol·L^{-1} BT and 0.2 mol·L^{-1} FeTos in 1-propanol, respectively. The *in situ* polymerization is performed with a spin coater featuring a heatable substrate holder at 90 °C. Thereafter, the films are rinsed in ethanol and annealed at 200 °C for 10 minutes in ambient atmosphere. Organic solvent cleaned ITO substrates are employed to enable thickness measurements without another polymer layer underneath the PT. The solar cells are fabricated and characterized according to the routine given in chapter 5. For the thickness variation of the PT layer, the molar concentration ratio between BT and FeTos is set to 1:2, while the overall concentration is varied between 0.06 mol·L^{-1} and 0.15 mol·L^{-1}.

Characterization: The absorbance of the film is determined by measuring the UV/Vis transmission. Possible reflection and scattering contributions are neglected. The electronic state of the films is analyzed by means of four-point probe measurements. The given current-voltage curves are measured by a current sweep from -0.01 to 0.01 mA. Optical microscopy images are recorded at magnifications of 10x and 100x. Film thicknesses are determined by profilometry.

Experimental details on chapter 7

The investigated polythiophene thin films are produced by spin coating from the metastable reaction mixture of BT and FeTos as described in chapter 5. Afterwards, the films are rinsed in either acetonitrile, to obtain PT in its doped and conductive state, or in ethanol, to reduce it back to the uncharged, semiconducting state. The molar ratio between monomer and oxidizing agent is varied between 3:1 and 1:3, to cover the conditions of having the oxidizing agent both in deficiency and excess, respectively. The total concentration in the reaction mixture, meaning the sum of both reactant concentrations, is adjusted according to the film thicknesses required for the specific measurement technique.

For *four-point probe measurements*, PT is spin coated onto PP coated glass substrates. The total concentration for each ratio is 0.2 mol·L^{-1}. The film thickness, which is necessary for the calculation of the electrical conductivity, is obtained by profilometry. For this purpose, the same reaction mixtures are spun onto ITO coated glass substrates and the

height profile is measured across a scratch. Conductivity measurements are performed on the doped PT films only.

The discussed *GIWAXS* measurements are performed at the beamline 7.3.3 at the Advanced Light Source (ALS). [71] The employed wavelength is $\lambda = 1.24\,\text{Å}$, corresponding to a photon energy of 10 keV. The measurements are performed at a sample-detector distance of 299 mm, the incident angle is set to 0.16° and therefore above the critical angle of the investigated polymer. The shown solid angle corrected 2d pattern and respective radially and azimuthally integrated intensities are obtained using the GIXSGUI 1.6 software of Argonne National Laboratory, taking into account the necessary corrections. [58, 59] For GIWAXS PT is spin coated onto PP covered glass substrates from reaction mixtures with total concentrations of $0.7\,\text{mol}\cdot\text{L}^{-1}$ (ratios 3:1, 2:1), $0.4\,\text{mol}\cdot\text{L}^{-1}$ (1:1) and $0.3\,\text{mol}\cdot\text{L}^{-1}$ (1:2, 1:3), respectively. GIWAXS measurements are performed on both doped and undoped PT films.

For the *transmission and reflection measurements*, PT is spin coated on PP coated glass (transmission and reflection) and silicon (luminescence), respectively. The total concentration is kept at $0.2\,\text{mol}\cdot\text{L}^{-1}$ for all samples. The emission spectra, which are only recorded for semiconducting PT films, are measured after excitation with a wavelength of $\lambda = 500\,\text{nm}$.

MIS-CELIV measurements are performed to measure the vertical hole mobilities of the undoped PT films. For this purpose, PT is spun onto etched ITO substrates in three iterations, to obtain film thicknesses of about 200 nm. The total concentration of the mixtures is set to $0.7\,\text{mol}\cdot\text{L}^{-1}$ (ratios 3:1, 2:1), $0.4\,\text{mol}\cdot\text{L}^{-1}$ (1:1) and $0.3\,\text{mol}\cdot\text{L}^{-1}$ (1:2, 1:3), respectively. Finally, 50 nm MgF_2 and 100 nm aluminum are evaporated on top. The mobility measurements are performed using different offset voltages and the obtained mobility values are averaged for each sample.

Experimental details on chapter 8

The film formation processes during the *in situ* polymerization of polythiophene are the center of this investigation. For this purpose, the film fabrication is performed *via* deposition of the metastable reaction mixture by slot-die coating to enable the examination of the film formation *in situ* during drying. The employed reaction mixtures have bithiophene to FeTos molar ratios of 1:3 (excess) and 2:3 (deficiency), respectively. The overall educt concentration in 1-propanol is $0.3\,\text{mol}\cdot\text{L}^{-1}$in both experiments. The substrates are precleaned by acid cleaning and covered with PEDOT:PSS by spincoating prior to the PT deposition to ensure the adhesion of the resulting PT layer. Afterwards, the films are rinsed in ethanol for ten minutes and thermally annealed at 200 °C in ambient atmosphere for another ten minutes.

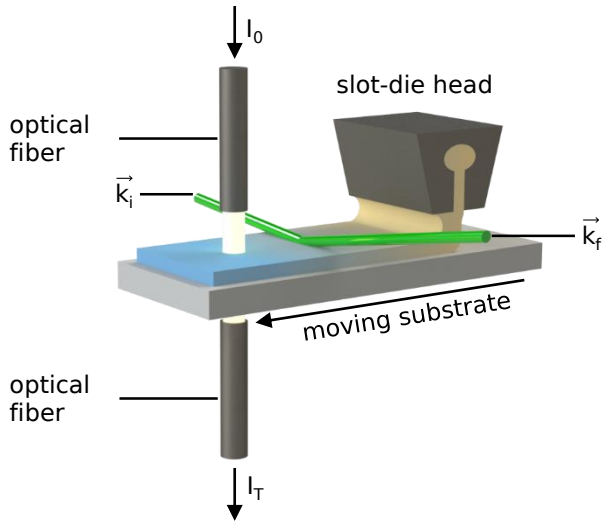

Figure 5.3: Schematic illustration of experimental setup of simultaneous GIWAXS and transmission measurements. Reaction mixture is deposited onto preheated substrate through slot-die print head by moving of the sample stage. White light of initial intensity I_0 and transmitted intensity I_T is guided by optical fibers. Incoming X-ray beam ($\vec{k_i}$) impinges film, scattered and reflected intensity ($\vec{k_f}$) are detected on an area detector. In the course of the reaction the solution turns from orange to blue.

The *slot-die printing* of the metastable reaction mixture is performed with a customized printing setup which was designed for simultaneous time-resolved measurements at synchrotron X-ray beamlines. [81] The print head is located inside an atmospheric chamber for environmental control. The substrate is placed on the sample stage that is heated to 85 °C. The print head is adjusted at a height of 0.3 mm above the substrate and fed with the solution via a syringe pump at a rate of 0.25 mL·min^{-1}. After the formation of a solution meniscus between print head and substrate, the sample stage is moved laterally with a speed of 20 mm·s^{-1} for coating the substrate. Figure 5.3 schematically depicts the process of the slot-die printing as well as the position of the simultaneous irradiation with X-rays and white light for structural and composition analysis, respectively.

The *in situ GIWAXS* experiments are performed at the Sirius beamline at Soleil synchrotron. [72] The X-ray energy is set to 10 keV corresponding to a wavelength of 0.124 nm. The beam enters the printer chamber through a Kapton® entrance window and hits the sample under an incident angle of 0.20°. The scattered X-rays exit the chamber through a second window and are collected on a Pilatus 1M detector at a sample-to-detector distance of 366 mm. The time-resolved data are recorded at a rate of ten measurements per second at a counting time of 0.90 s per measurement. Subsequently to the time-resolved measurements, static GIWAXS experiments are performed with a counting time of 60 s. The intensities are later normalized to the respective irradiation times for comparison. The raw data are converted into reciprocal space and reduced by application of the software GIXSGUI. [58] The radial integration is peformed between polar angles of 20-85°. The material characteristic scattering peaks are analyzed by fitting with self-written Python scripts. The fitting procedure is introduced in detail in section 7.2.

The *in situ transmission* measurements are performed simultaneously at a rate of two measurements per second, each measurement being the average of 30 scans with 0.016 ms

counting time to reduce the noise. Prior to the data collection, the background spectrum of the empty chamber is recorded to obtain the wavelength-dependent initial intensity I_0 of the white light. The recorded transmission spectra are employed for calculation of the absorbance without taking possible reflections into account. Finally, the absorbance of the PEDOT-coated substrate is subtracted. The fitting of the resulting spectra is performed with self-written Python scripts. The fitting functions are introduced in detail in section 7.1.

Finally, the results of the two simultaneously performed measurements are correlated. The first measurement after the sample stage reaches its final position is set to be the starting point at t = 0 s, since a recording of the transmission is only possible in that position, which is roughly two seconds after the solution deposition.

Experimental details on chapter 9

The thin films discussed in this chapter are prepared by spin coating from metastable reaction mixtures, such as described in detail in chapter 5. Initially, two individual stock solutions of monomer bithiophene (0.2 mol·L^{-1}) and FeTos (0.4 mol·L^{-1}) are prepared in propanol, respectively. The final metastable precursor solutions are obtained by mixing these stock solutions with different amounts of water and additional propanol with the volumes given in table 5.1.

Table 5.1.: Volumes of stock solutions of BT (0.2 mol·L^{-1} in propanol) and FeTos (0.4 mol·L^{-1} in propanol), additional propanol, and water for preparation of metastable reaction mixtures with varied water fractions.

water fraction	V_{BT} [mL]	V_{FeTos} [mL]	$V_{propanol}$ [mL]	V_{water} [mL]
0 %	0.150	0.150	0.100	0
5 %	0.150	0.150	0.080	0.020
10 %	0.150	0.150	0.060	0.040
15 %	0.150	0.150	0.040	0.060
20 %	0.150	0.150	0.020	0.080
25 %	0.150	0.150	0	0.100

After the synthesis, the films discussed in section 9.1 are rinsed in ethanol for dedoping and removal of precursor residuals and byproducts and finally thermally annealed. The films investigated in section 9.2 are left as-prepared.

For *scanning electron microscopy* the PT films are prepared on ITO coated glass for increased sample conductivity. The measurements are performed with an accelerating voltage of 5 keV and at a working distance of 3.0 mm.

The discussed *GIWAXS* and *GISAXS* measurements are performed at the Sirius beamline of Soleil synchrotron. [72] The employed wavelength is $\lambda = 1.55$ Å corresponding to a photon energy of 8 keV. For GISAXS, the sample-detector distance (SDD) is set to 447 m. An incident angle α_i of about 0.3° is adjusted by help of an X-ray camera. Slight deviations from that angle are determined and accounted for by help of the sample horizon position in the detector image. The GISAXS data are reduced for analysis using DPDAK version 1.2.0 from the Deutsches Elektronen-Synchrotron (DESY). [73] The resulting horizontal cuts are modeled in the framework of the distorted wave Born approximation (DWBA) and the local monodisperse approximation (LMA) using three cylindrical form factors, each assigned with a structure factor representing a 1d paracrystal. More details on the employed model are given in section 3.3. GIWAXS measurements are performed at an SDD of 33 vm and with an incident angle of 0.18°. The shown solid-angle corrected two dimensional pattern are obtained using the GIXSGUI 1.5 software of Argonne National Laboratory, taking into account the necessary corrections. [58, 59] For scattering experiments, the polythiophene films are fabricated on polypropylene coated glass slides.

6. Establishing an *in situ* polymerization

The aim of this project is to establish a solution-based fabrication technique for thin films of semiconducting native polythiophene (PT). The synthesis shall employ a chemical oxidative polymerization mechanism which is based upon the monomer activation by help of an oxidizing agent. In comparison to the electrochemical approach, such chemical oxidation enables the film synthesis independently of the employed substrate type. Finally, the fabrication routine is optimized with respect to the applicability of the resulting semiconducting PT films in the active layer of organic solar cell devices.

Bravo-Grimaldo et al. have previously presented an oxidative *in situ* polymerization routine employing a metastable reaction mixture of a monomer and an oxidizing agent. [32] In their approach, bithiophene (BT) and terthiophene are successfully polymerized upon application of phosphomolybdic acid hydrate (PMA) as oxidizing agent. While they fabricated conducting, doped PT films with their routine, they did not explore the possibilities of dedoping the films to their fully semiconducting state. Moreover, the applicability in organic electromic devices has not been the focus of their work. Nevertheless, the polymerization technique introduced by Bravo-Grimaldo et al. serves as starting point for the development of an *in situ* synthesis in this thesis.

Section 6.1 discusses the adaption of the original routine to enable the fabrication of semiconducting films. Thereafter, the oxidizing agent PMA is replaced by iron(III) p-toulenesulfonate (FeTos) in order to increase the film homogeneity. This is discussed in section 6.2. Finally, the films are employed in solar cell devices in section 6.2.

6.1. Oxidative polymerization with PMA

At first, polythiophene thin films are polymerized *in situ* by employing the literature-known method of Bravo-Grimaldo et al. [32] In this approach, PMA serves as oxidizing agent for the monomer BT. Both educts are dissolved in the same metastable solution, whose stability arises from the similar redox potentials of the two reactants, as discussed

in chapter 3. Nevertheless, the original procedure needs to be modified to obtain PT in its semiconducting state for application in the active, light-absorbing layer of a solar cell. This is done by firstly inducing in chemical dedoping by a change of the rinsing routine that is necessary after the actual film fabrication, and secondly introducing a thermal annealing step subsequently to the rinsing in order to increase the polymer interaction in the film and potentially improve the film quality.

Dedoping to semiconducting state

It is known that rinsing doped polythiophene with alcoholic solvents can dedope the chains to their neutral semiconducting state. [33] To ensure the applicability of this procedure to the here investigated synthetic process, the films are rinsed in acetonitrile or ethanol, respectively, after spin coating to compare the influence of a non-alcoholic to an alcoholic rinsing solvent on the film properties. At first sight, the resulting films already vary in color, with the acetonitrile-rinsed films being grayish-blue and the ethanol-rinsed ones rather orange. A more detailed analysis of the solvents' impact on the electronic state of the resulting PT films is performed by means of UV/Vis spectroscopy and four-point probe measurements. Figure 6.1 shows the resulting absorbance spectra (a) and I-V curves (b).

The absorbance spectra of the two films feature absorption bands at different wavelengths. The acetonitrile-rinsed film, on the one hand, has two main bands with maxima

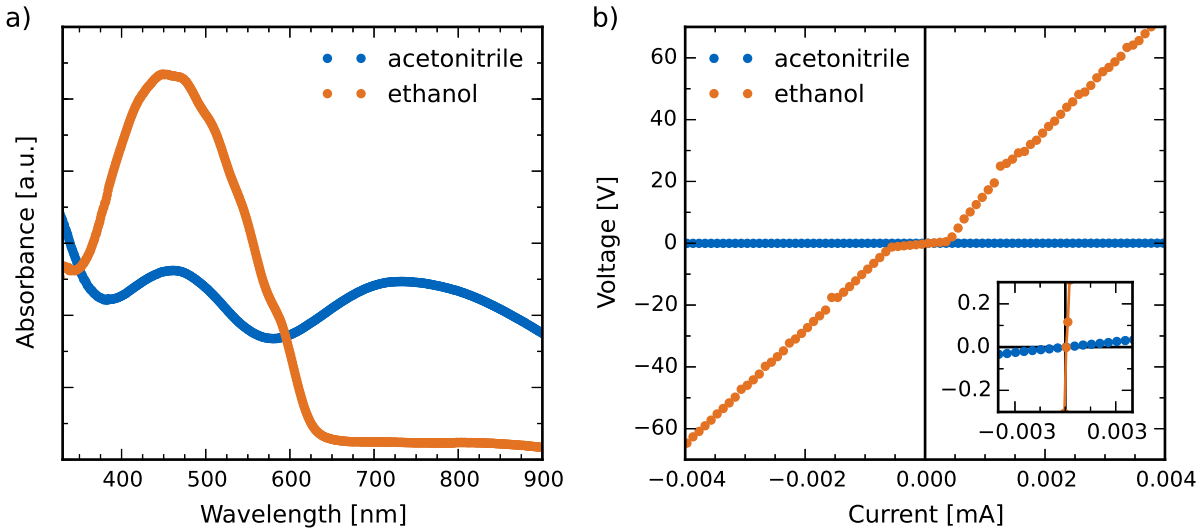

Figure 6.1.: Comparison of PT polymerized *in situ* with PMA after rinsing with acetonitrile (blue data) and ethanol (orange data), respectively. a) Absorbance of thin films, b) current-voltage curves as determined by four-point probe measurements, the inset shows only the low-voltage data points for clearer representation, orange line is guide to the eye.

located at 460 nm and 730 nm, respectively. While they are of similar intensity, the low-energy absorbance expands over a broader wavelength region. The ethanol-rinsed film, on the other hand, has one major absorption band between approximately 330 and 640 nm. Moreover, this band shows several shoulders in its lower-energy flank.

The two obtained spectra match very well the typical shape expected for the absorbance of doped and undoped PT, respectively. [27,33,82] Undoped PT intrinsically absorbs blue light while the charged thiophene chromophores absorb red and infrared light. [83] Hence, rinsing the film with acetonitrile keeps it in its chemically doped state, with both neutral (absorbance band at 460 nm) and charged species (730 nm) present in the film. By rinsing with ethanol, these charged species are neutralized, resulting in a completely neutral PT film.

The effect of this neutralization on the polymer electrical conductivity is investigated by four-point probe measurements. Figure 6.1b shows the I-V curves measured for the two different films. Again the data vary significantly for the respective samples. For the ethanol-rinsed PT the detected voltage expands from approximately -60 to 60 V in the presented current regime, showing a high electrical resistance of the film. The slope of the voltage measured for the acetonitrile-rinsed film, on the other hand, only becomes visible in the inset given in the lower right corner of the graph which shows only a very small voltage regime. Hence, the resistance is much lower here. Putting the observations of both measurements together it is concluded that the state of the resulting PT films can indeed be adjusted to either charged and conducting by rinsing with acetonitrile or neutral and semiconducting by rinsing with ethanol.

Thermal annealing

After adapting the original fabrication route to obtain semiconducting PT thin films by exchange of the rinsing solvent, the post-treatment of the films is investigated further in order to improve its electronic properties. The electronic behavior of polymers is known to depend strongly on their crystallinity and film morphology. [16,17] Thermal annealing is commonly employed to induce polymer crystallization by heating the polymers above their glass transition temperature T_g to introduce sufficient mobility to allow the chains to reorganize into their energetically more favorable (semi) crystalline structure. Different values of 120 °C and 248 °C can be found in the literature for T_g of native PT. [84, 85] Moreover, studies have shown the thermal stability of PT up to at least 300 °C. [86]

In order to find the optimal annealing temperature for the here *in situ* polymerized PT films, it is varied between 100 °C and 250 °C to cover the range of the previously reported glass transition temperatures. Thereafter, the increase in polymer crystallinity is analyzed qualitatively by means of UV/vis absorption spectroscopy. A selection of the

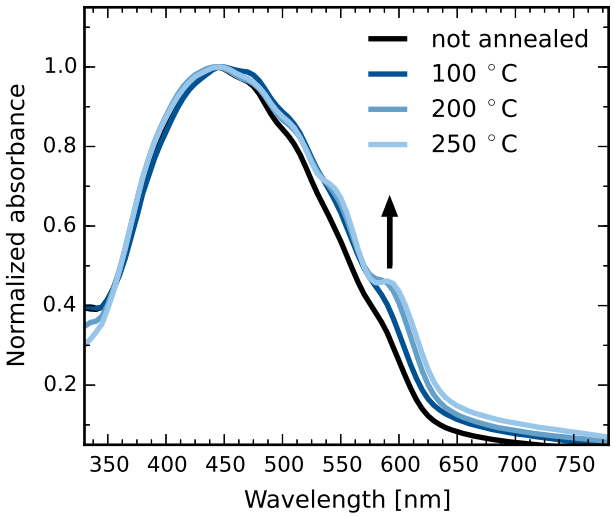

Figure 6.2: Normalized absorbance spectra of *in situ* polymerized PT films annealed at different temperatures. Each dataset is normalized to its respective maximum. Arrow indicates increase of shoulders suggesting increasing polymer crystallinity.

resulting spectra is displayed in figure 6.2. All samples show a broad absorption in the visible range. Nevertheless, there are some distinct differences between the differently post-treated films. The absorbance of the film obtained without thermal post-treatment (black curve) is rather featureless without any pronounced band structure. Comparing it to the sample annealed at 100 °C (dark blue curve) one finds an intensity gain beyond 450 nm accompanied by the evolution of several shoulders. Upon increasing the annealing temperature even further to 200 °C (medium blue curve) the shoulders become much more pronounced. Going to an even higher temperature of 250 °C (light blue curve) does not result in further significant changes of the absorbance shape.

The absorbance shoulders that form and increase upon thermal annealing typically form when semiconducting polymers aggregate in an ordered fashion and are attributed to the single vibronic transitions according to the Franck-Condon principle. [46, 87, 88] Hence, already a qualitative analysis of the UV/Vis spectra reveals an increased polymer interaction upon increased thermal annealing temperature. A more detailed interpretation of the PT absorbance and the information they contain on the polymer crystallinity is given in chapter 7. The thermal post-treatment is performed at 200 °C in all following experiments, inducing a significant increase in the PT aggregation according to the absorbance spectra. Annealing at yet higher temperatures is avoided to reduce the potential degradation of the other components of the respective samples.

Film quality

In order to serve as active layers in organic solar cells the thin films need to exhibit an adjustable, homogeneous thickness as well as a smooth surface to ensure an optimized interaction between the different functional layers of the device stack. The homogeneity

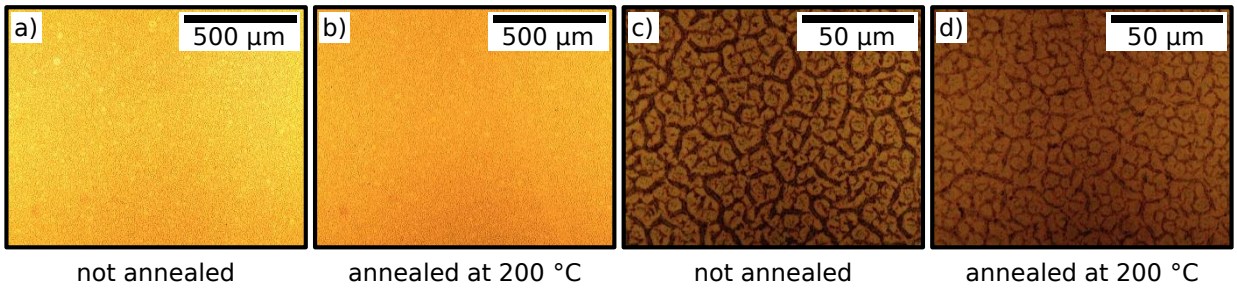

Figure 6.3.: Optical micrographs of PT films synthesized *in situ* with PMA taken before (a,c) and after (b,d) thermal annealing, taken at two different magnifications, respectively.

and surface quality are investigated by means of optical microscopy. Figure 6.3 shows the respective micrographs at two different magnifications of a PT film before and after thermal annealing.

At low magnification, the microscopy images (figures 6.3a and b) reveal that the employed *in situ* polymerization generates polymer films without the formation of any large grains or crystallites. Moreover, no dewetting of the film is observed and the film appears to be of a similar average thickness over a larger area. Comparing the films before and after annealing reveals no differences. At larger magnification, however, the film exhibits a strongly cracked surface prior to the thermal annealing (figure 6.2c). The cracks do not feature any distinct order. After annealing (figure 6.2d) the film appears to be smoother with a reduced depth of the cracks.

Application in solar cells

In a last step, the PT thin films obtained from the *in situ* synthesis with PMA are employed as donor layer in bilayer solar cells with PCBM as acceptor material. Specifications on the employed functional layers are given in section 5.2.3. The fabricated devices, however, do not show the current-voltage behavior that is characteristic for diode devices but only a linear slope. Hence, the device behaves like a resistor, most likely due to short circuits created by cracks in the PT layer. Therefore it is concluded that the employed polymerization is not suitable for the fabrication of semiconducting PT thin films that can successfully be applied in bilayer solar cells. However, the knowledge gained about the impact of different post-treatment steps can be transferred to the adapted synthesis presented in the next section.

In summary it is possible to adapt the synthesis proposed by Bravo-Grimaldo et al. to fabricate both conducting and semiconducting PT thin films by choosing the right rinsing solvent after the fabrication. Moreover, the crystallinity of semiconducting PT

is increased by a subsequent thermal annealing at 200 °C, as suggested by the evolution of vibronic shoulders in the UV/Vis absorbance spectra. Nevertheless, the films are not suitable for application in solar cells as they feature cracks and inhomogeneities that create short circuits in the bilayer device architecture. Hence, it is necessary to change the synthetic approach in order to achieve a compact polymer layer.

6.2. Oxidative polymerization with FeTos

As revealed in the last section, the *in situ* synthesis of PT from metastable reaction mixtures of BT and PMA does not result in PT films with sufficient homogeneity for the application in organic solar cells. Hence, the routine needs to be optimized further. This is done by exchanging the oxidizing agent PMA for iron(III) p-toulenesulfonate (FeTos). FeTos has been introduced by Bayer in 1988 for the *in situ* polymerization of poly(3,4-ethylenedioxythiophene) (PEDOT) from solution. [76] Since then, it has been employed as oxidant for the synthesis of high-quality PEDOT films with different fabrication techniques and for various electronic applications. [55, 89–93] Moreover, Kolodziejczyk et al. have employed FeTos in the vapor-phase *in situ* polymerization of PT. [36, 37] Although this has not been done so far, FeTos appears to be a promising candidate for a novel solution-based *in situ* synthesis of PT thin films. In the following, a routine is developed by combining the findings of the previous section with knowledge on the *in situ* polymerization of PEDOT with FeTos given in literature.

Synthetic routine

For a solution-based *in situ* polymerization of PEDOT with FeTos, a reaction mixture of EDOT monomer and FeTos dissolved in an alcoholic solvent is employed. The alcoholic solvent molecules interact with the formed polymer-oxidant complexes resulting in an improved packing of the PEDOT chains in the final film. [94] The PEDOT polymerization is performed by first coating the substrate with the two precursor molecules and heating it for the actual polymerization reaction afterwards. [89, 91, 93]

In order to find the optimal reaction conditions for the *in situ* polymerization of PT with FeTos, the reaction mixtures are prepared in ethanol, propanol, and butanol, respectively. Other than in the PEDOT fabrication, however, spin coating the solution at room temperature followed by a subsequent heating step does not result in homogeneous polymer films, although the polymerization reaction does take place. Therefore, the synthesis is performed with a spin coater with heated substrate plate. By heating the substrate prior to the solution deposition as well as during the actual spin coating process allows the reaction to take place during the spinning. The required temperature

depends strongly on the boiling temperature of the respective employed solvent, increasing from about 60 °C for ethanol to 100 °C for butanol. However, the fabrication from propanol at 90 °C results in the most homogeneous films. Hence, all following experiments are performed by fabrication of PT from a reaction mixture of BT and FeTos in propanol. The post-treatment steps already optimized in the previous chapter including a rinsing-step in ethanol and thermal annealing at 200 ° are adopted for the new synthesis.

Film quality

The quality of the PT thin films after rinsing in ethanol for dedoping and annealing at 200 °C is checked by optical microscopy. Figure 6.4 shows optical micrographs at two different magnifications. In both images the PT films appear to be very homogeneous, without any large-scale aggregate formation or material dewetting. Moreover, the films do not reveal the cracks that are obtained they feature when the synthesis is performed with PMA (see figure 6.3). Their applicability in organic solar cells will be verified later on in section 6.3.

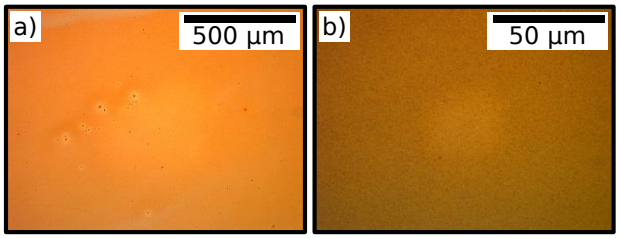

Figure 6.4: Optical micrographs of PT films synthesized *in situ* with FeTos taken after thermal annealing.

Optical properties

The optical properties of the resulting material are analyzed by means of absorption spectroscopy. For this purpose, the absorption coefficient α is calculated from the measured film absorbance and thickness. Subsequently, the optical band gap can be obtained from the respective Tauc plot. Both plots are displayed in figure 6.5. The absorption coefficient (figure 6.5a) shows the absorption over a broad wavelength range. The overall shape is very similar to that of PT obtained from a synthesis with PMA (figure 6.2), with a featureless absorbance in the low-wavelength regime and vibronic shoulders at wavelengths beyond the absorbance maximum. Hence, the polymer chains are also aggregated in an ordered structure here. With a maximum of $2.8 \cdot 10^5$ cm^{-1} at 504 nm the absorption coefficient is similar to that for PT synthesized for example by oCVD. [34] Moreover, α is more than three times higher than that of crystalline P3HT films due to the missing volume of the optically inactive side chains. [95]

The optical band gap E_g is related to α according to the Tauc equation 4.3. By plotting $(\alpha E)^{1/2}$ against E and fitting the energy range between 1.97 and 2.03 eV with a linear

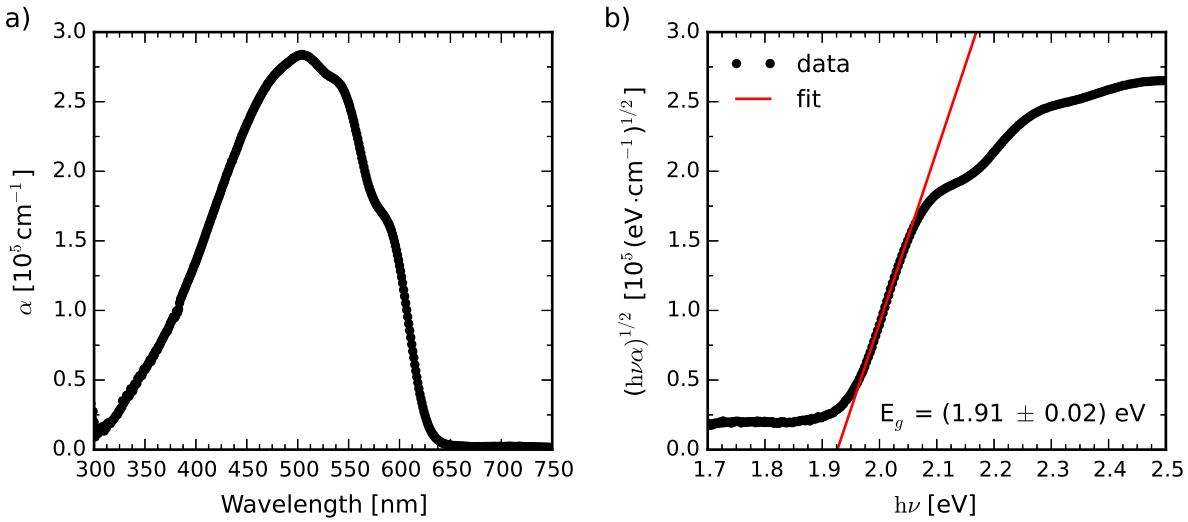

Figure 6.5.: Optical properties of PT synthesized with FeTos, a) absorption coefficient α as a function of wavelength, b) Tauc plot for determination of optical band gap by fitting low-energy flank of the curve. The band gap is obtained by averaging the values of four films, error corresponds to respective standard deviation.

function (displayed in figure 6.5b), E_g is determined as the x-axis intercept. This procedure is performed for four PT films of thicknesses between 15 and 42 nm. The resulting E_g is (1.91 ± 0.02) eV and therefore only slightly larger than that of P3HT which is reported to be between 1.85 and 1.9 eV. [40, 42]

Deposition technique

A major advantage of a solution-based thin film deposition is the flexibility with regards to employed fabrication technique and the potential up-scaling to larger substrates by for example roll-to-roll printing. [8] In order to investigate whether the here developed synthesis is transferable from spin coating to other solution deposition processes, the metastable reaction mixture is deposited to larger substrates by means of slot-die coating. For this purpose, a custom made lab-scale printing setup is employed, which enables a constant heating of the substrate plate. [81]

For *in situ* polymerization during printing, the synthetic routine previously optimized for spin coating is maintained in terms of solvent, substrate temperature, and post-treatment routine. The printing parameters are optimized with respect to resulting film appearance. The best film qualities are obtained by setting the substrate to print head distance to 0.3 mm, feeding the solution to the print head at 0.25 mL·min^{-1}, and printing at a speed of 20 mm·s^{-1}. More details on the printing procedure are found in chapter 5. Figure 6.6 shows an image of the printed films (after rinsing and thermal annealing)

Figure 6.6: Photograph of different sample types frabricated with here developed *in situ* polymerization of polythiophene: slot-die printed sample (left, $7.5 \times 2.5\,cm^2$), spin coated pure PT film (top right, $2.5 \times 2.5\,cm^2$), solar cell (bottom right, $2.0 \times 2.0\,cm^2$).

in comparison to the spin coated PT film on glass and a lab-scale PT:PCBM solar cell. All of these sample types are fabricated from the here developed *in situ* polymerization technique. As the picture shows, the absorption behavior of the films (semi-transparency, color) is very similar for printed and spin coated films. Therefore it is concluded that the established synthesis enables a film fabrication by different solution deposition techniques.

Overall, it is possible to obtain semiconducting PT thin films by employing FeTos as oxidizing agent in a solution-based *in situ* polymerization. The resulting films are of high homogeneity, as shown by optical microscopy, and feature a similar optical band gap as P3HT. Moreover, the synthesis enables a PT thin film fabrication by different solution-deposition techniques, as shown exemplary for slot-die coating. Finally, the applicability of the semiconducting films in the active layer of organic bilayer solar cells is discussed in the next section.

6.3. PT:PCBM bilayer solar cells

The two previous sections presented the development of an *in situ* polymerization technique for semiconducting PT thin films. Since these are desired to be applicable in organic solar cells, this section deals with the fabrication and characterization of the respective devices.

As introduced in chapter 3 the active layer is usually composed of two different materials, the donor and the acceptor. These compounds need to exhibit an offset between their

respective energy levels to support an efficient charge carrier separation. One of the most frequently employed and investigated donor-acceptor couples is P3HT:PCBM. [20, 21] As the characterization of the films showed, the band gap of the synthesized PT is very similar to that of its derivative P3HT. Moreover, the combination of PT:PCBM has already been reported to result in functioning solar cells when PT is synthesized by different approaches. [26, 33] Hence, the PT films prepared here are likewise combined with PCBM in a bilayer architecture.

The *in situ* polymerized PT films are employed in solar cells with a geometry of (ITO/PEDOT:PSS/PT/PCBM/Al). As the PT film is insoluble, the active layer is prepared in a bilayer geometry by subsequent spincoating of PT and PCBM. First, the general fabrication process is optimized with regard to the different annealing steps to improve the electronic properties of the individual layers as well as the contact between them. An optimal performance of the solar cells is achieved by the following processing routine:

1. etching and cleaning (organic solvents, oxygen plasma) of the ITO substrate
2. spincoating of PEDOT:PSS, thermal annealing at 150 °C
3. *in situ* polymerization of PT layer, rinsing in ethanol, thermal annealing at 200 °C
4. spincoating of PCBM layer
5. evaporation of aluminum electrodes, thermal annealing at 100 °C

For a more detailed description of the single relevant steps in the solar cell fabrication refer to chapter 5.

Table 6.1.: Solar cell parameters obtained for PT:PCBM bilayer devices with varied PT layer thickness set by variation of solution concentration, errors are standard deviations to given mean values of four solar cell pixels each. Thickness is derived from profilometry, concentration corresponds to sum of molar concentrations of BT and FeTos in metastable reaction mixture (at molar ratio BT:FeTos = 1:2).

PT layer thickness [nm]	**concentration [mol·L^{-1}]**	**j_{SC} [mA·cm^{-2}]**	**V_{OC} [V]**	**FF [%]**	**PCE [%]**
15 ± 2	0.06	0.1 ± 0.1	0.38 ± 0.05	25 ± 1	0.01 ± 0.01
20 ± 3	0.09	1.7 ± 0.3	0.53 ± 0.03	53 ± 5	0.5 ± 0.2
31 ± 3	0.12	1.9 ± 0.3	0.60 ± 0.05	58 ± 3	0.7 ± 0.2
42 ± 4	0.15	1.7 ± 0.2	0.63 ± 0.01	60 ± 1	0.6 ± 0.1

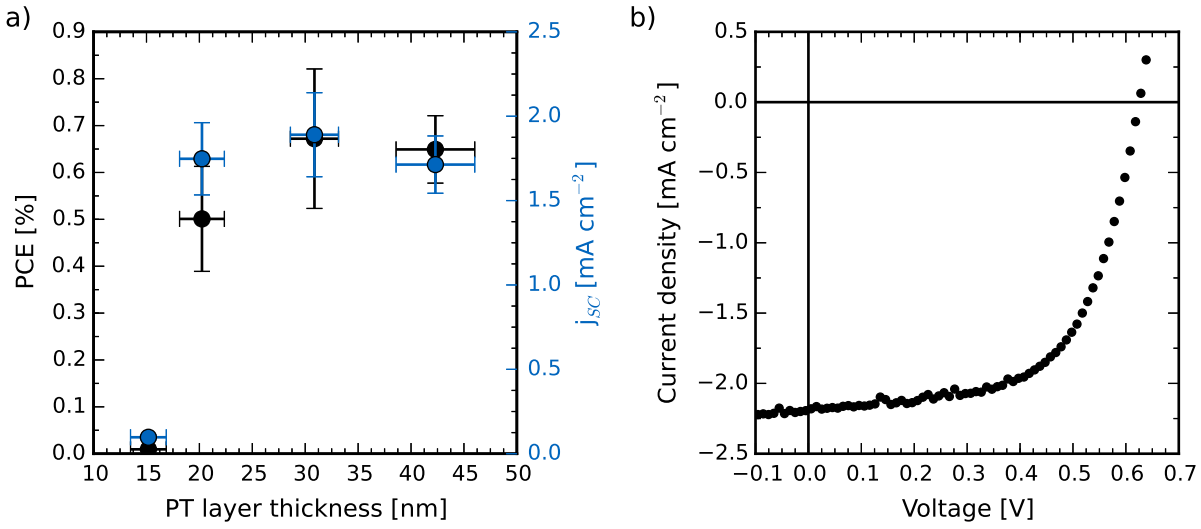

Figure 6.7.: Solar cell performance data of bilayer devices with varied PT layer thickness. a) PCE and j_{SC} of different thicknesses, error bars correspond to standard deviations of given mean values. b) Current-voltage characteristic of champion cell with PCE of 0.8 %.

Finally, the PT layer thickness is optimized by variation of the concentrations of the two components in the reaction mixture. In a bilayer solar cell, the optimal thickness of the semiconducting layers is a trade-off between a high enough thickness for sufficient light absorption, i.e. charge carrier generation, and the upper limitations of exciton diffusion length and low carrier mobility. Here, the film thickness was varied between (15 ± 2) and $(42 \pm 0.2$ nm. The resulting solar cell parameters for the respective devices are summarized in table 6.1. The values are obtained by averaging over four solar cells each.

Upon increasing the PT thickness the performance of the solar cells is changing constantly, with a change in j_{SC}, V_{OC}, fill factor, and PCE, respectively. So clearly, the thickness has an impact on several of the involved processes. Most importantly, however, the evolution of the j_{SC} should be stressed here, as this factor is most strongly dominated by the amount of absorbed light and the mobility of the charges in the device. [21] While it is increasing from $(0.1 \pm 0.1)\,\mathrm{mA{\cdot}cm^{-2}}$ at 15 nm to $(1.9 \pm 0.3)\,\mathrm{mA{\cdot}cm^{-2}}$ at 31 nm, it subsequently decreases again to $(1.7 \pm 0.2)\,\mathrm{mA{\cdot}cm^{-2}}$ at 42 nm. Although this current drop is not significantly changing between these two thicknesses, the mean value is highest for the solar cells with 31 nm of PT. Moreover, the single highest efficiency of one cell is found to be 0.8 % for the solar cell with that thickness. Hence, it is assumed that the optimal layer thickness is around that value. A similar result was found for bilayer solar cells with oCVD prepared PT. [33]

The power conversion efficiency (PCE) and the short circuit current density (j_{SC}) are

graphically presented in figure 6.7a, the I-V curve of the solar cell pixel with highest achieved efficiency is shown in figure 6.7b. The efficiency of the champion cell is the same Borrelli et al. found for bilayer PT cells with C_{60} as acceptor. [33] Also, they found the optimal layer thickness to be 25 nm and therefore in the same region as in the here presented approach. Other fabrication routes and device geometries implementing native PT in solar cells have resulted in similar performances. [26, 35]

6.4. Summary

A solution-based *in situ* polymerization offers the possibility of producing thin films of unsubstituted semiconducting polymers at low material and fabrication costs while at the same time being tunable through a large number of parameters. Moreover, the fabrication can easily be up-scaled to enable a production with industrial techniques such as printing. In this chapter, an oxidative polymerization routine is established that is suitable for synthesizing PT thin films which can be employed in the active layers of organic solar cells.

Initially, a routine for the synthesis of conductive PT films is adapted to convert the polymer into its semiconducting state. Moreover, the thermal annealing temperature is optimized to improve the packing and intermolecular interactions of the chains in a post-treatment step. However, the application of PMA as oxidizing agent does not result in films of sufficient homogeneity for use in solar cell devices. Hence, PMA is replaced with FeTos, an iron salt often employed for synthesizing the PT derivative PEDOT. After determination of the electronic band gap of the polymer, the thin films are successfully implemented in bilayer solar cells in combination with PCBM which serves as electron acceptor. The highest power conversion efficiency achieved is 0.8 %, showing that the developed solution-based fabrication can compete with the less variable fabrication techniques known from literature. Moreover, this novel *in situ* synthesis can be performed by application of different solution-deposition techniques, as established for slot-die printing.

7. Controlling polymer aggregation

While native PT offers the advantage of being more stable than most of the soluble semiconducting polymers [26,96], it is not often considered for device application because of its low degree of crystallinity and the aggregation in a herringbone (HB) motif, which results in weak intermolecular interaction and therefore poor charge transport properties. This HB motif of the neutral, uncharged chains originates from the electrostatic repulsion of the π orbitals of neighboring polymer backbones.

A novel solution-based *in situ* polymerization for semiconducting polythiophene (PT) thin films is established in the previous chapter. The polymerization technique is based on an oxidative reaction mechanism which can be distinguished into two subsequent steps as introduced in section 3.2. In a first step, the Fe^{3+} ions of FeTos oxidize the monomer molecules to activate them for polymerization. Afterwards, potential excess iron ions can further oxidize the already existing polymer chains. The resulting charged and therefore doped PT backbones are stabilized by the tosylate anions, which are ionically bound to the PT chains as counter ions. In an *in situ* synthesis this chemical doping process is potentially taking place during the film formation.

This chapter investigates how this changed charge distribution along the polymers influences their aggregation during film formation. Furthermore, it is examined whether this process-intrinsic chemical doping can be exploited for structural control. For this purpose, the molar ratio between monomer and oxidizing agent within the metastable reaction mixture is varied to potentially tune the level of doping during the synthesis. Subsequently to the synthesis, the films are rinsed in order to remove residual molecules or byproducts of the reaction. By choice of the solvent, it is possible to finally obtain doped, conducting (acetonitrile-rinsing) or undoped, semiconducting PT films (ethanol-rinsing), as shown in section 6.1. While acetonitrile solely rinses out the soluble compounds, ethanol additionally induces a reduction of the PT chains to their neutral state, a process accompanied by the removal of the tosylate ions. Hence, semiconducting and conducting PT are fabricated from the same reaction mixtures.

The article *Directing the aggregation of native polythiophene during in situ polymerization* is based on the work presented here. [97]

The electronic conductivities and molecular structures of the doped PT films are discussed in section 7.1. The influence of the prior doping process on the final semiconducting, undoped PT films on the other hand is presented in section 7.2. Finally, it is possible to draw a model of the film formation process during *in situ* polymerization and the involved polymer crystallization under the influence of doping in section 7.3.

7.1. Conducting polythiophene films

This section deals with the impact of the amount of FeTos in the reaction mixture on the electronic and structural properties of PT in its doped state. These are obtained by acetonitrile-rinsing after film fabrication, which leaves the polymer chains oxidized and the tosylate ions are electrostatically attached to them. The ratio between monomer and oxidizing agent in the employed reaction mixtures is varied between 3:1 and 1:3 to verify that it is indeed possible to tune the level of doping during the synthesis. This is discussed in section 7.1.1. Afterwards, the effect of the incorporated tosylate counter ions on the packing structure of the doped PT chains is analyzed by means of grazing incidence X-ray scattering in section 7.1.2.

7.1.1. Doping level

Four-point probe measurements are performed to obtain the electrical conductivities σ as an estimate of the respective levels of doping. σ is calculated from the measured sheet resistance according to equation 4.8. The origin of the electrical conductivities is investigated further by measurements of UV/Vis spectroscopy. Figure 7.1 shows the obtained conductivity (a) and normalized absorbance spectra (b) for three selected monomer to oxidant ratios.

The measured conductivities are in the range between 0.1 and $0.8\,\mathrm{S{\cdot}cm^{-1}}$, which is comparable to those of conducting PT films synthesized *in situ* with other oxidizing agents and several orders of magnitude above the conductivities of semiconducting PT ($10^{-8} - 10^{-4}\,\mathrm{S{\cdot}cm^{-1}}$). [32, 34, 98] Moreover, there is a strong conductivity gain upon increasing amount of FeTos in reaction mixture. A surplus of BT gives lower conductivities of $(0.08 \pm 0.02)\,\mathrm{S{\cdot}cm^{-1}}$ (ratio 3:1) and $(0.13 \pm 0.04)\,\mathrm{S{\cdot}cm^{-1}}$ (2:1), respectively, which jump to $(0.8 \pm 0.1)\,\mathrm{S{\cdot}cm^{-1}}$ (1:2) and $(0.74 \pm 0.08)\,\mathrm{S{\cdot}cm^{-1}}$ (1:3) for a surplus in FeTos.

The origin of the conductivity increase is visible in the absorbance spectra in figure 7.1b. All spectra have two broad absorption bands at $\lambda \approx 470\,\mathrm{nm}$ and $\lambda \approx 700\,\mathrm{nm}$. These correspond to the uncharged (lower wavelength) and cationic (higher wavelength) thiophene chromophores, respectively. [83] When normalized to the maximum of the absorption band

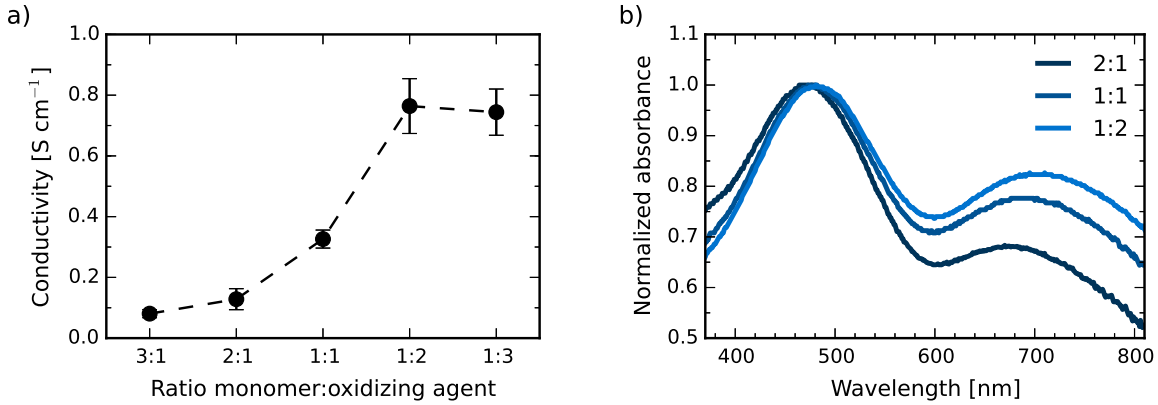

Figure 7.1.: Properties of doped PT films polymerized *in situ* with different monomer to oxidizing agent ratios in the reaction mixture. a) Electrical conductivities obtained from four-point probe measurements, error bars correspond to standard deviations of given means values. b) Absorbance of thin films with absorption bands of neutral ($\lambda \approx 470$ nm) and cationic chromophores ($\lambda \approx 700$ nm), respectively. Spectra normalized to maximum of neutral absorption band.

of the uncharged thiophene moieties, the intensity at lower wavelength steadily increases upon increased FeTos fraction. Hence, the fraction of doped to undoped molecules in the thin films increases when more FeTos is employed. Therefore the conductivity increase can without a doubt be assigned to an increased doping level and not for example a change in chain lengths or film quality. Thus, the degree of doping is easily tunable by variation of the FeTos amount in the mixture. With reference to the sudden jump of the conductivities, the BT to FeTos ratio is from here on referred to as FeTos *deficiency* (ratios 3:1 and 2:1) and *excess* (ratios 1:2 and 1:3). Since the level of doping is defined by the amount of cationic charges on the PT chain, the amount of attached tosylate ions within the polymer network has to be increasing as well. The impact of these anions on the packing structure of the polymer chains is therefore analyzed with GIWAXS in the next section.

7.1.2. Structural impact of doping

Grazing incidence wide-angle X-ray scattering (GIWAXS) measurements are performed to investigate the structural impact of the incorporated tosylate anions upon varying doping level. Figure 7.2 shows the two dimensional scattering pattern of the doped films obtained with molar ratios of 2:1 (oxidant deficiency, low level of doping), and 1:2 and 1:3 (oxidant excess, high level of doping), respectively. Due to a measurement artifact the pattern are superimposed by signals of the detector subunits and therefore only described and interpreted qualitatively.

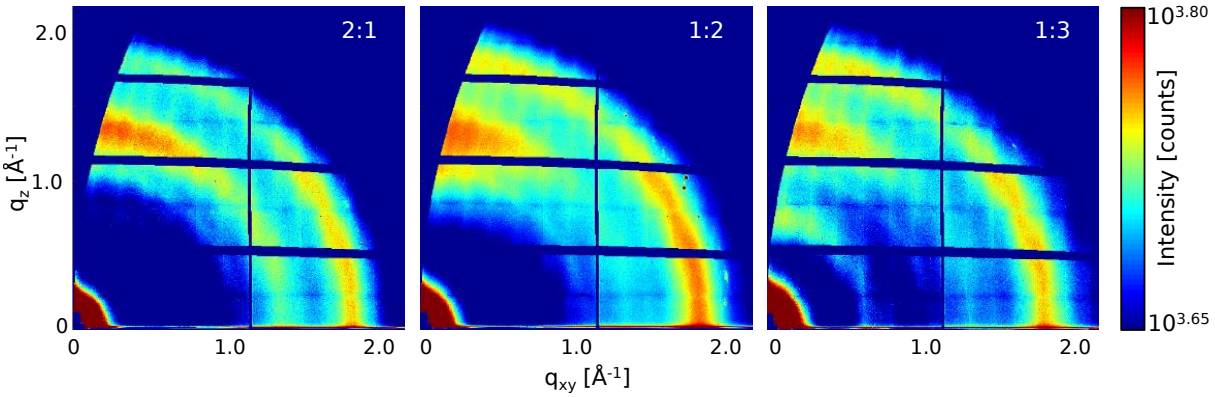

Figure 7.2.: Two dimensional GIWAXS pattern of *in situ* polymerized doped, conducting polythiophene thin films, fabricated from reaction mixtures with varied monomer to oxidant ratio. The amount of oxidizing agent and thereby the level of doping during the synthesis increases from 2:1 (left) to 1:3 (right).

The GIWAXS pattern of the only slightly doped PT synthesized under FeTos deficiency (ratio 2:1) shows two broad signals at approximately $q = 1.4\,\text{Å}^{-1}$ and $1.8\,\text{Å}^{-1}$ (real space distances $d = 4.5\,\text{Å}$ and $3.5\,\text{Å}$). These appear to feature a minor anisotropy with respect to the polar angle. The ring at lower q is more intense in vertical direction, while the second ring is enhanced in horizontal direction. However, the superimposed detector pattern might have an influence on that intensity distribution. The doped film synthesized with ratio 1:2 and therefore in tosylate excess exhibits a similar scattering pattern, but with a strongly increased anisotropy of the rings. Going to an even higher degree of doping (ratio 1:3), the GIWAXS pattern develops an additional signal at $q = 0.77\,\text{Å}^{-1}(d = 8.2\,\text{Å})$, with highest intensity in direction of q_z.

The two rings appearing in all the pattern have previously been observed for doped PT synthesized with different methods. [99–101] Nevertheless, the crystallographic data are not sufficient to resolve the underlying crystal structure. The opposite evolution of the anisotropy of the signals however suggests that the rings correspond to two perpendicular planes of the same crystal structure. The Bragg peak appearing for highest doping level is known to appear in diffraction pattern of bulk PT beyond a critical doping level. Yamamoto and coworkers have proposed a transition of the crystal structure upon incorporation of dopant into the polymer network. [101] According to them, the packing motif changes from herringbone (HB) to a lamellar stacking, in which π-stacked polymer layers are alternating with layers of electrostatically attached dopant molecules.

The reason behind this change in crystal structure is the tendency of charged oligo- and polythiophenes to form π-stacked dimers. [102,103] These dimers arise from the formation

of bonds between parallelly arranged backbones, leading to an enhanced stabilization of the charges. π-stacked crystal structures have been observed for large numbers of positively charged oligothiophenes. [102, 103] Chaalane et al. have performed density functional theory (DFT) calculations of tosylate doped oligothiophenes, in order to predict the relative orientation of the tosylate anion to the oligomer chain. [104] According to them the tosylate is attached in a sidewise arrangement, with an intermolecular distance of 3.5 Å between the sulfur atoms of thiophene and tosylate, respectively. These results support the presence of a lamellar structure in the highly doped PT films, where the lattice distance of 8.2 Å is in the range of the twofold calculated distance between thiophene chain and tosylate. [104] The proposed lamellar structure with tosylate ions packed between the backbones along with the lattice distance of 8.2 Å is illustrated schematically later-on in figure 7.7a.

In summary, the characterization of *in situ* polymerized PT films showed that the doping level of the films is easily tunable by variation of the ratio between BT and FeTos in the employed reaction mixture. Moreover, an increased doping level results in the evolution of π-stacked crystals in the film. The following section investigates the impact of this change in doping level and crystal structure on the semiconducting films that are obtained when the films are rinsed in a different solvent after synthesis.

7.2. Semiconducting polythiophene films

Undoped polythiophene thin films can be obtained from the same reaction mixtures as the doped ones by simply rinsing them in ethanol subsequent to the synthesis. Hence, it is understood that the here discussed semiconducting polymers show the same varied level of doping directly after the synthesis. Whether the structural changes induced by the doping are still maintained is discussed in section 7.2.1. Furthermore, a spectroscopic analysis and measurements of charge carrier mobilities in section 7.2.2 show the resulting changes in the intermolecular interaction.

7.2.1. Structural analysis

As seen in section 7.1, the amount of FeTos in the reaction mixture has a large impact on the doping level of the conductive PT thin films. Moreover, beyond a certain threshold of incorporated tosylate ions within the film, lamellar crystallites appear in the film. Here, the structure of PT thin films after dedoping and removal of the tosylate ions is investigated by GIWAXS. The two dimensional scattering pattern of the undoped films obtained with molar ratios of 2:1, 1:2, and 1:3 are presented in figure 7.3.

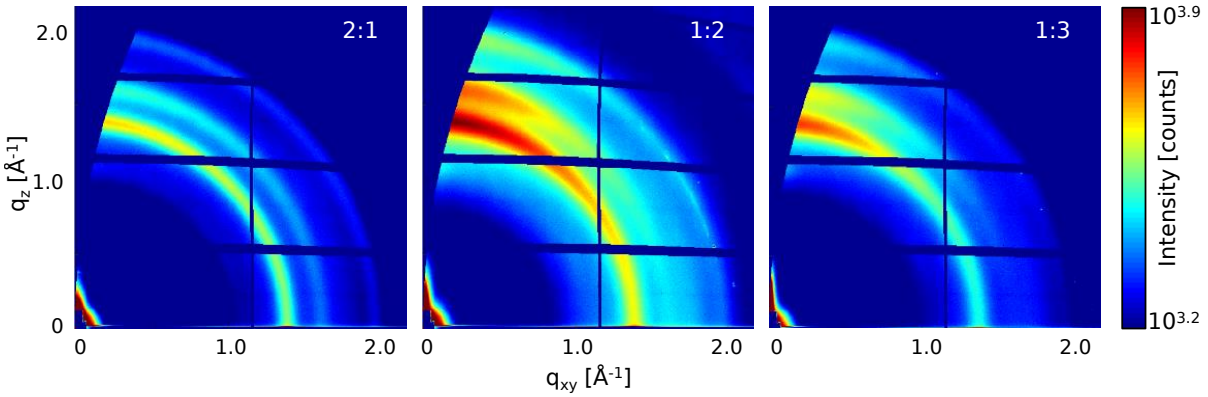

Figure 7.3.: Two dimensional GIWAXS pattern of *in situ* polymerized undoped, semiconducting polythiophene thin films, fabricated from reaction mixtures with varied monomer to oxidant ratio. The amount of oxidizing agent and thereby the level of doping during the synthesis increases from 2:1 (left) to 1:3 (right).

All GIWAXS pattern clearly exhibit three sharp rings at scattering vectors $q = 1.40\,\text{Å}^{-1}$, $1.63\,\text{Å}^{-1}$, and $1.98\,\text{Å}^{-1}$ corresponding to real space distances of $d = 4.5\,\text{Å}$, $3.8\,\text{Å}$, and $3.1\,\text{Å}$. For PT obtained under FeTos deficiency (figure 7.3 on the left, ratio 2:1) the signals are rather isotropic along the polar angle χ. The PT films synthesized under oxidant excess on the other hand show an increasing anisotropy, with the intensity of all three rings being higher in the direction of q_z. The peak positions match the main Bragg reflections of the HB structure that unsubstituted PT exhibits in its neutral state. The crystal structure of polythiophene has only been resolved in two dimensions, but the visible signals are known to be intermolecular distances between the thiophene rings. [105, 106] The HB packing motif along with the direction of the unit cell axes a and b is depicted in figure 7.7b.

Orientation analysis

The rings show a strong gain in anisotropy with increased fraction of FeTos employed during the synthesis. This anisotropy is most likely related to a preferred orientation of the HB crystallites inside the films. The three HB Bragg peaks correspond to lattice planes that lie in the ab-plane of the unit cell, while the axis of the polymer backbones is perpendicular to that plane. [105, 106] Therefore, the observed change in intensity distribution of the signals is interpreted as the unit cell's ab-plane lying preferably perpendicular to the substrate surface. This corresponds to the polymer backbone axis being parallel to the sample plane. A similar orientation has so far only been observed for polythiophene grafted from a sample surface. [107]

The fraction of HB crystallites with preferred orientation can be quantified by az-

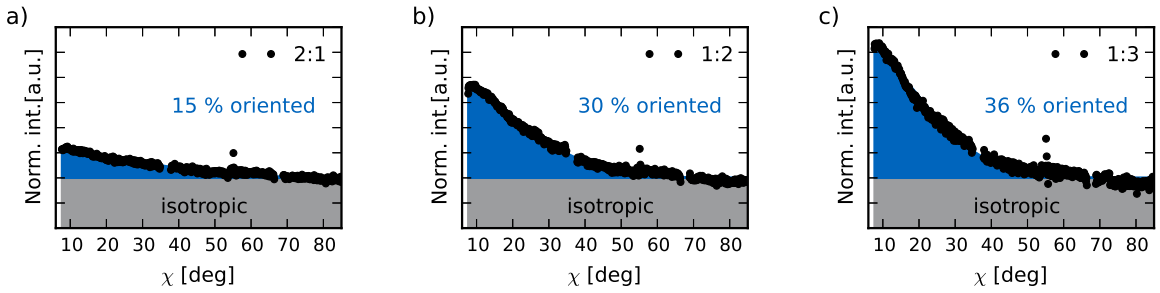

Figure 7.4.: Normalized azimuthal intensities of HB peak at 1.4 $Å^{-1}$ plotted against polar angle for orientation analysis of the HB crystallites in undoped PT thin films synthesized from reaction mixtures with BT to FeTos molar ratios of 2:1 (left), 2:1 (middle), and 1:3 (right). Fraction of crystallites with preferred (blue) as compared to isotropic orientation (gray). Each dataset is normalized to intensity of isotropic contribution.

imuthally integrating the intensity of the first and most prominent HB ring at 1.4 $Å^{-1}$ to investigate the intensity distribution along the polar angle. The background and amorphous contribution of the scattering intensity are accounted for by integrating the intensity at both edges of the ring and subtracting the average for each χ. The resulting intensities for the differently synthesized PT thin films are displayed in figure 7.4.

The displayed peak intensity contains on the one hand isotropic contributions, that are constant for all values of χ, and additionally an enhanced peak that is assumed to have its maximum at $\chi = 0°$. This peak intensity is increasing steadily from ratio 2:1 (figure 7.4a), to the ratios 1:2 (figure 7.4b), and finally 1:3 (figure 7.4c). The fraction of crystallites with preferred orientation can be estimated as the fraction of the area of this respective peak to the overall integrated intensity. For this purpose, the intensity distribution for each sample is fitted as the sum of a constant isotropic contribution (colored gray in the figure) and a Gaussian function with center at $\chi = 0°$ (blue). In this approach, the sample symmetry is not accounted for. This would require the combination of scattering data measured with different sample orientations or a mathematical symmetry correction. However, the latter is only possible for samples that act as in-plane powders [59, 108], which is not necessarily true for the here investigated PT films. Hence, the simple calculation of peak area to isotropic area does not yield factual amounts. However, they give an estimate on the tendency of the crystallite orientation upon changing BT to FeTos ratio. The fraction of the peak integral increases from 15 % (2:1), to 30 %, and finally 36 % for the highest amount of FeTos in the synthesis (1:3).

It is possible to explain the influence of the doping process on the polymer orientation by the induced changes in the chemical structure of the backbones. Upon oxidation, the electrons along the chain rearrange in a way that PT goes from benzoid to quinoid

configuration, as described in section 3.2. This rearrangement of the electrons results in double bonds between the thiophene rings, which prohibit ring rotation around the backbone axis. Hence, doped PT chains are much more rigid than the uncharged ones. [53] It is assumed, that during the film formation process the polymer chains undergo doping before precipitation to the substrate. When converted into their stiff, quinoid configuration, a planar precipitation with the backbone parallel to the substrate appears to be more likely than for the undoped and probably randomly coiled chains.

Summing this up, the induced backbone stiffening of the doping has a clear impact on the resulting orientation of the HB crystallites in the undoped PT films. Due to a more favorable planar precipitation of the stiffer molecules, the PT synthesized with the highest level of doping has the highest fraction of crystallites oriented with backbones parallel to the sample plane.

Crystal structure analysis

For a more detailed analysis on the crystal structures present in the PT films, the scattering intensities are radially integrated to determine the respective peak characteristics. Integrations are performed in the near out-of-plane (vertical cuts) direction between polar angles $0° < \chi < 15°$ and in horizontal direction (horizontal) between $75° < \chi < 85°$. The resulting intensity profiles are corrected for different contributions to obtain only the crystalline peaks. To begin with, the background scattering is fitted with an exponential decay and subsequently subtracted. [109] Since the PT films are synthesized on top of a polypropylene (PP) layer, the respective intensity profiles of a bare PP film are fitted with two Gaussian functions. The PP peaks appear at smaller scattering vectors than the PT signals and can therefore be scaled to the low-q flank of the cuts and likewise be subtracted. The resulting intensities only hold scattering of amorphous and crystalline PT. Finally, the amorphous contributions of native polythiophene can equally be described by two broad Gaussian functions. [106]

After subtracting the scattering of background, polypropylene, and amorphous polythiophene, the peaks of crystalline PT remain. The resulting vertical and horizontal cuts for the undoped PT films synthesized with monomer to oxidant molar ratios 2:1, 1:2, and 1:3 are depicted in figure 7.5. All vertical cuts (figure 7.5a) show the three clearly resolved HB Bragg peaks ($q = 1.40\,\text{Å}^{-1}$, $1.63\,\text{Å}^{-1}$, and $1.98\,\text{Å}^{-1}$), with highest peak intensities for PT obtained with ratio 1:2, indicating the largest volume fraction of HB crystallites in that thin film. Furthermore, an additional peak arises at $q = 1.08\,\text{Å}^{-1}$ ($d = 5.8\,\text{Å}$). The horizontal cuts (figure 7.5b), on the other hand, show a very drastic change when going from the tosylate deficiency to the excess regime. Here, a new signal appears at approxi-

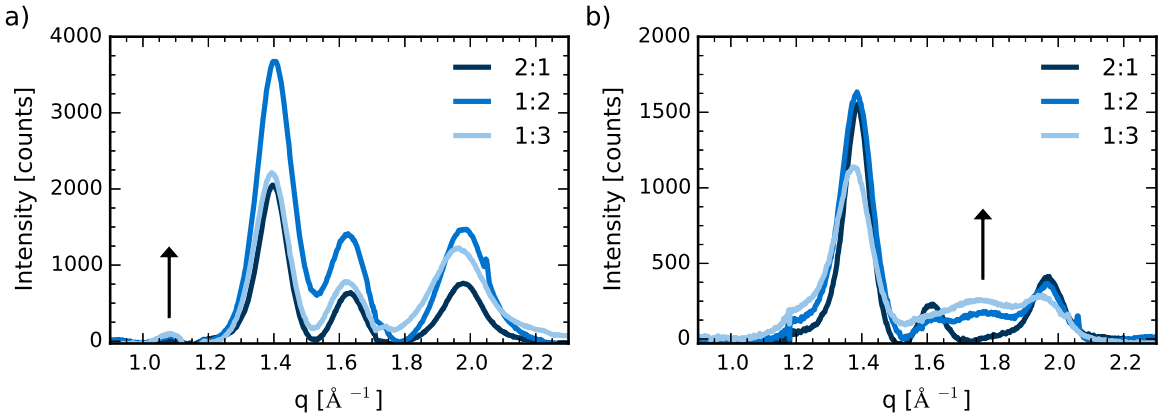

Figure 7.5.: Radially integrated intensities of GIWAXS pattern of undoped PT thin films synthesized with varied ratios of monomer to oxidizing agent. Intensity profiles obtained in (a) vertical and (b) horizontal direction. Arrows indicate signals assigned to proposed new π-stacking structure.

mately $q = 1.76\,\text{Å}^{-1}$ ($d = 3.6\,\text{Å}$), whose intensity is on the order of the second and third HB peak in those cuts.

The structural analysis of highly doped PT synthesized with the same reaction mixture leads to the proposal of a lamellar structure with π-stacked PT (section 7.2.1). Consequentially, the newly arising peaks in the semiconducting PT cuts are assigned to π-stacks that remain in the sample, even after dedoping and removal of the tosylate. The signal arising in horizontal direction ($d = 3.6\,\text{Å}$) matches the calculated intermolecular distance for tosylate doped oligothiophenes ($d = 3.7\,\text{Å}$) [104] and, moreover, is in the same range as π-stacking distances of the well-investigated PT derivatives P3HT ($d = 3.8\,\text{Å}$) [110] and PEDOT ($d = 3.4\,\text{Å}$) [111]. Therefore, the small feature appearing in the vertical cuts at $q = 1.08\,\text{Å}^{-1}$ very likely corresponds to a backbone spacing distance between the PT chains perpendicular to the π-stacking direction, that results from a shrinkage of the lamellar distance upon removal of the attached tosylate ions. The anisotropy of these signals indicates something like an edge-on orientation of these crystallites, with their π-stacking direction along the sample plane. For illustration, the proposed structure is depicted in figure 7.7 (c) along with the lamellar packing of highly doped PT (a), and the typical HB packing (b).

Molecular dynamics simulations

The GIWAXS data suggest that the polymers remain frozen in a non-equilibrium π-stacking after dedoping to their neutral state. This differs strongly from the reversible rearrangements that have been observed for doping of bulk PT. [101] In order to analyze

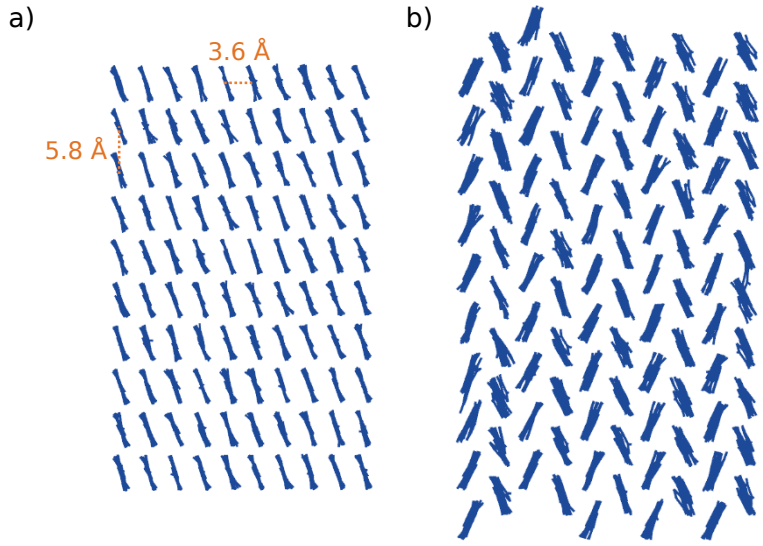

Figure 7.6.: Side view of a PT 10-mer crystal calculated by means of MD simulations. a) interchain distances are constrained to 5.8 Å in lamellar direction and 3.6 Å perpendicular to it, resulting in an arrangement of parallel aligned PT chains; b) a removal of all distance constraints yields the typical HB crystal structure.

whether such π-stacking is feasible for neutral PT under constrained conditions, molecular dynamics (MD) simulations are performed. Technical specifications on the simulation are given in the appendix.

The structure of a crystal of 100 PT 10-mers is simulated for two different cases. In the first case, the PT chains are constrained in their lateral movement in such way that the intermolecular crystal lattice distances observed in the GIWAXS data (5.8 Å and 3.6 Å) are kept constant. Rotations around the backbone axes, on the other hand, are not restricted. In the second case all constraints are removed, allowing the chains to change the distances between them. The calculated crystal structures are graphically depicted in figure 7.6. With lateral constraints (figure 7.6a), the PT oligomers all tilt in the same direction. As a result, the thiophene rings of neighboring chains are π-stacked. Without constraints (figure 7.6b), on the other hand, the chains shift in their position and tilt in an alternating fashion. Here, the calculation yields the typical polythiophene herringbone structure. The HB unit cell parameters that are derived from the MD simulations (a = 7.10 Å, b = 5.71 Å) agree well with experimental and theoretical values from literature (a = 7.10 Å, b = 5.71 Å). [105, 106]

The MD simulations show that the HB structure represents the global energetic minimum for neutral polythiophene. Nevertheless, a π-stacking structure is indeed possible when the distances between the chains are restrained. This is proposed to be the case

in the presented *in situ* polymerization, when the process-intrinsic doping results in a π-stacking of the charged polymers which are embedded in the bulk film during film formation. As a consequence, the chains are constrained from significant movements thereafter, leading to a maintained π-stacking structure even upon dedoping.

In summary, the structural investigation reveals two effects of the doping process during synthesis on the crystallization of polythiophene. Firstly, an orientation analysis of the HB peaks shows a strong increase in crystallites with horizontally aligned backbones. This effect is explained by the stiffening of the PT chains upon doping and the subsequent planar precipitation and aggregation. Secondly, there is an irreversible effect on the packing behavior of the chains. As a result of the dimerization that is typical for oligothiophene cations the system arranges into a lamellar structure with tosylate anions sandwiched between PT π-stacks at high doping level. But surprisingly, this change is not reversible upon dedoping to semiconducting PT. Once the polymers have aggregated in a π-stacked fashion and have been incorporated into the film structure, they are restrained from going pack to HB structure. MD simulations additionally support that they rather remain frozen in a non-equilibrium π-stacking.

A π-stacking is assumed to have a strong impact on the intermolecular interactions of PT, as the orbital overlap between neighboring chains is increased significantly. This is analyzed and discussed in the following section.

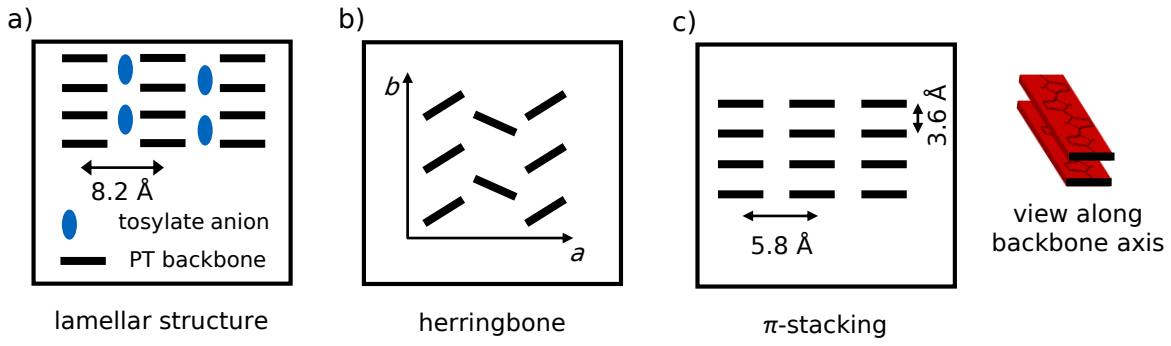

Figure 7.7.: Simplified illustration of proposed polythiophene crystal structures. a) Lamellar arrangement of highly doped PT: π-stacked PT with tosylate anions sandwiched in-between; b) typical herringbone structure of semiconducting PT with direction of unit cell axes a and b; c) proposed π-stacking structure of semiconducting PT obtained after high doping during synthesis. All depictions drawn in side view (along the polymer backbones), marked crystal lattice distances as obtained from GIWAXS measurements.

7.2.2. Polymer interaction

This section deals with the influence of the previously discussed structural changes on the intermolecular interaction in semiconducting PT films. For this purpose, there will first be a spectroscopic analysis researching the type of interaction between the backbones. Afterwards, the resulting impact on the polythiophene's electric properties, namely the hole mobilities, will be presented.

Spectroscopic analysis

Measurements of the thin film UV/Vis absorbance and emission are performed to obtain information on the aggregation and electronic interaction of the polythiophene backbones. The respective normalized spectra are shown in figure 7.8. In the lower wavelength regime one finds the absorbance spectra, which expand from the ultraviolet region to beyond 600 nm and look similar to those found for polythiophenes obtained with different kinds of syntheses. [34,82] Evidently, the absorbance intensity decreases in the lower-wavelength region when the amount of FeTos in the synthesis is increased. At the same time, the shoulders at higher wavelength become more pronounced. Like the spectra of its derivatives like P3HT, the spectra of PT can be divided into an amorphous contribution of the disordered chains at higher energy and the vibronic transitions of the aggregated thiophene chromophores of elongated, ordered polymer chains at lower energies. [112] Hence, the absorbance reveals an increasing fraction of ordered PT backbones when the films are synthesized under FeTos excess.

The chromophore interaction is further investigated by measuring the photoluminescence (PL) of the films. PL measurements are only successfully possible for samples synthesized with intermediate ratios of 2:1, 1:1, and 1:2. The ones obtained with highest deficiency (3:1) or excess of FeTos (1:3) appear to be too rough for reliable emission measurements, as they give rise to spectra of very undefined shape that differ strongly from the ones presented in figure 7.8. The emission spectra that are plotted on the high-wavelength side of the graph in figure 7.8 all exhibit a strong emission band at around 620 nm and a second strong emission at 670 nm. When the BT:FeTos ratio during synthesis is changed from 2:1 up to 1:2, the relative intensity of the first emission band is strongly decreasing. Moreover, the position of the emission becomes slightly red-shifted. Considering the emission spectra of P3HT, the two emission bands are assigned to the 0-0 and 0-1 emission of the polythiophene backbone. [112] A decreasing 0-0/0-1 ratio is a strong indicator for increasing order in H-type aggregated thiophenes. [44,88] The redshift additionally suggests an increasing interaction between the chromophores of neighboring PT chains. Hence, a strong doping during the synthesis on the one hand strongly inceases

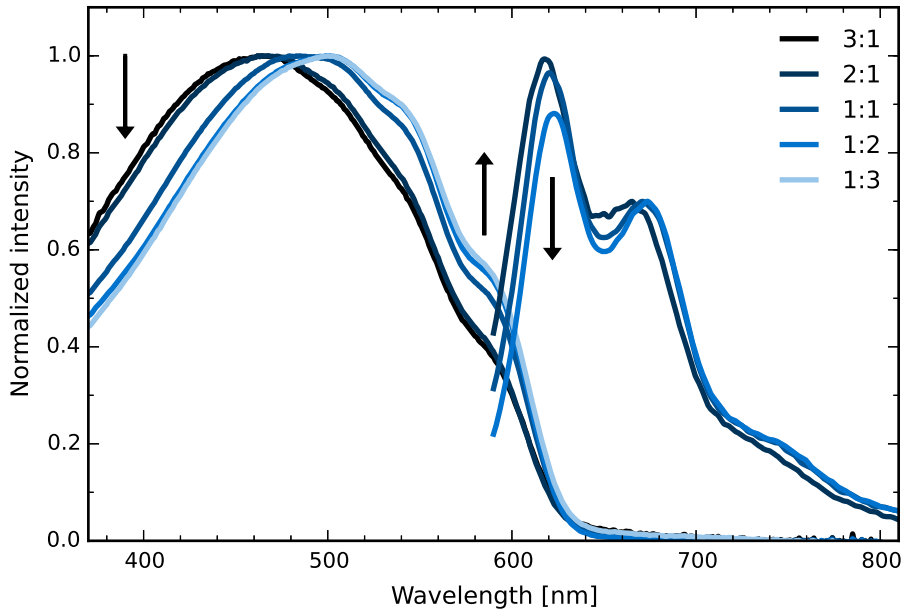

Figure 7.8.: Normalized absorbance (solid lines) and emission spectra (dashed lines) of undoped PT films synthesized *in situ* with varied molar ratios of monomer to oxidizing agent. Arrows indicate increasing 0-0 absorbance and 0-1 emission bands. Each absorbance spectrum is normalized to its respective maximum, photoluminescence spectra are normalized to height of 0-1 emission band.

the overall order in the films and, furthermore, results in an increased interaction between the chains, probably due to the induced π-stacking.

The electronic properties that result from the altered morphology in the films are discussed in the following.

Hole mobilities

The degree of crystallinity as well as the type of crystal structure have a strong impact on the final electronic properties of semiconducting polymer thin films. [16] Therefore, the vertical hole mobilities of the undoped films are measured by means of MIS-CELIV experiments. The results are given in figure 7.9.

The measured hole mobilities are on the order of 10^{-4}-$10^{-5}\,\mathrm{cm^2V^{-1}s^{-1}}$, matching the usually reported values of PT as well as P3HT. [113, 114] Overall, the mobility decreases with increasing amount of FeTos in the reaction mixture. There is an initial strong jump from $(7 \pm 2)\cdot 10^{-5}\,\mathrm{cm^2V^{-1}s^{-1}}$ (ratio 3:1) to $(16 \pm 5)\cdot 10^{-5}\,\mathrm{cm^2V^{-1}s^{-1}}$ (2:1) in the regime of FeTos deficiency. Thereafter, the mobility steadily decreases from $(4 \pm 1)\cdot 10^{-5}\,\mathrm{cm^2V^{-1}s^{-1}}$ (1:1), $(1.4 \pm 0.1)\cdot 10^{-5}\,\mathrm{cm^2V^{-1}s^{-1}}$ (1:2), and finally to $(0.9 \pm 0.3)\cdot 10^{-5}\,\mathrm{cm^2V^{-1}s^{-1}}$ (1:3).

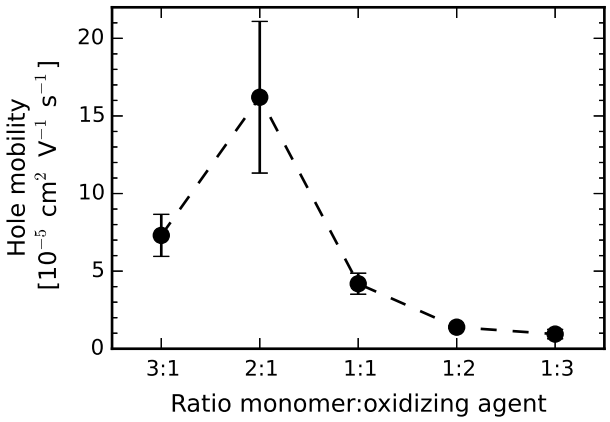

Figure 7.9: Vertical hole mobilities of undoped PT thin films polymerized *in situ* with varied molar ratios of monomer to oxidizing agent, as derived from MIS-CELIV measurements. The error bars correspond to standard deviations of given mean values.

The observed hole mobility decay can be explained by the difference in intra- versus interchain charge carrier transport in conjugated polymers. Usually, the mobility along an outstretched backbone is much faster than the hopping between different chains, even if the crystal structure enables a good intermolecular orbital overlap. [15] With regards to that, the decreasing vertical mobility upon increasing FeTos amount in the synthesis can be explained in terms of the strongly changed orientation of the HB crystallites. As discussed in the previous section, the chemical doping of the polythiophene chains during film fabrication probably increases their tendency to precipitate with backbones parallel to the substrate. As a result, the fraction of HB aggregates with horizontally oriented backbones increases strongly, when more FeTos is employed. Thus, the vertical pathways for hole transport are strongly reduced. Apparently, the effect of the π-stacked crystal structure is negligible compared to that of the orientation. The comparably low mobility obtained for ratio 3:1 is assumed to arise from a poorer film quality, since so little oxidizing agent is provided for polymerization.

7.3. Model

Combining the results of the performed analyses, it is possible to draw a model of the film forming process and the aggregation behavior of PT during the employed *in situ* polymerization method. Figure 7.10 schematically shows the impact of chemical doping during the synthesis on the resulting PT aggregation. Before application, the BT molecules and FeTos ions are both dissolved in the metastable reaction mixture without any reaction occurring. Upon spin coating, the monomers are oxidized by the Fe^{3+} ions and subsequently polymerize. Although the resulting oligomers become insoluble beyond a certain chain length, they apparently still possess enough mobility to undergo an additional oxidation by excess oxidant. This doping leads to a structural change in the backbone caused by a

transition from benzoid to quinoid configuration. In the quinoid structure, the C-C single bond between the thiophene units becomes a rigid double bond that prevents a rotation of the thiophene rings against each other. Therefore, the doped PT chains are much stiffer than the neutral ones. These rod-like chains probably precipitate on the substrate surface lying down.

Below a critical degree of doping the packing motif of the chains directly after fabrication and prior to the dedoping is not resolved. Upon dedoping, however, these PT chains pack in their typical HB structure. In this regime, the further oxidation by FeTos only induces the already mentioned horizontal orientation of the backbones. Hence, with increasing FeTos amount the fraction of horizontally oriented HB crystallites significantly increases. At very high Fe^{3+} concentration the doping level of the chains is high enough to induce a π-stacking of the charged chains. This process is typical for oligothiophene cations and induces an additional stabilization of the positive charges in the molecules. As a result, the strongly charged polymer is suggested to finally crystallize in a lamellar structure, in which the tosylate counter ions are sandwiched in-between the PT π-stacks. Here, dedoping and tosylate removal do not result in the formation of HB crystallites, but the PT chains rather remain in their π-stacking. This non-equilibrium packing is probably maintained due to the reduced mobility of the chains once they are incorporated inside the film, as shown by means of MD simulations. This novel PT crystal structure results in a strongly increased intermolecular interaction.

7.4. Summary

During the here investigated *in situ* polymerization of PT, the employed oxidizing agent FeTos serves two purposes: while it activates the monomers for polymerization, it additionally serves as chemical dopant already during the process. This chapter investigated the structural impact of that doping process on the resulting PT structure as well as the arising (opto)electronic properties.

In order to tune the doping level, the ratio between monomer BT and oxidant FeTos is varied in the employed reaction mixtures. The influence on the final doping level is analyzed by means of four-point probe measurements and UV/Vis spectroscopy, showing that the fraction of doped thiophene moieties in the films is growing if more FeTos is employed. This results in a strong increase in electrical conductivities. GIWAXS measurements on these doped PT films show the formation of a lamellar structure with π-stacked PT chains beyond a very high doping level.

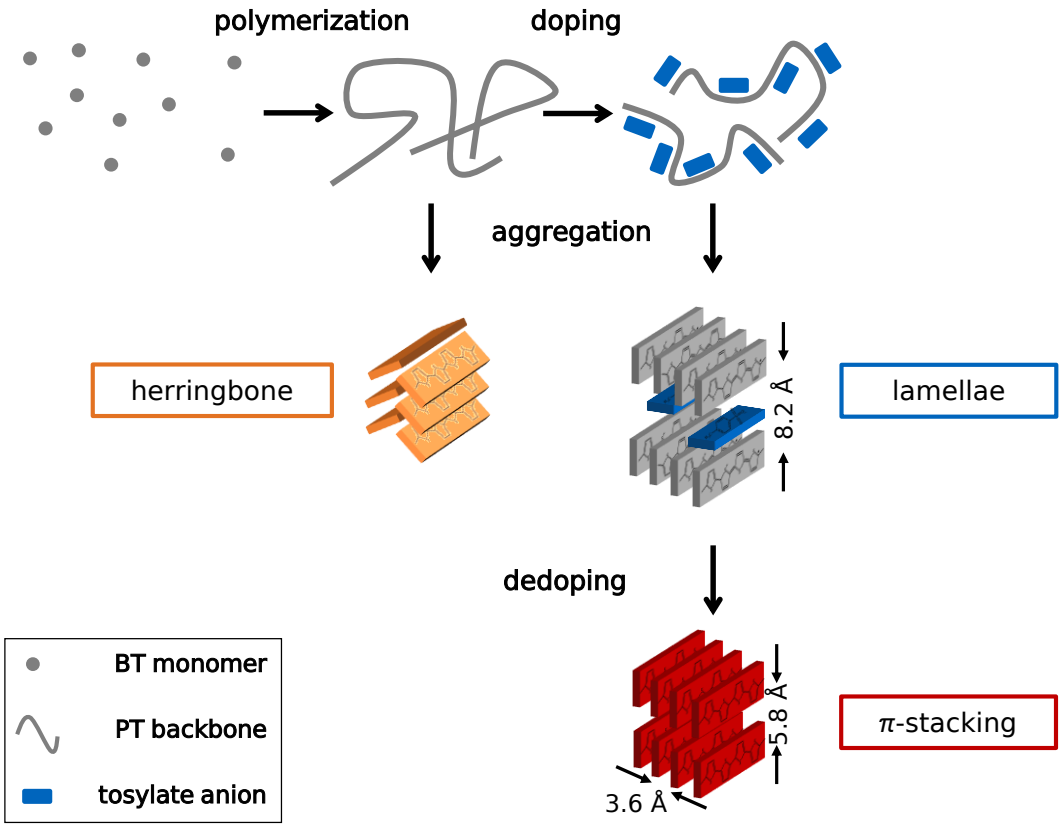

Figure 7.10.: Proposed process of *in situ* polymerization and resulting crystal structures: Two-step process with polymerization of BT to PT, that typical aggregates in herringbone structure if undoped. Excess of FeTos in the reaction mixture results in high degree of doping, which eventually induces lamellar π-stacked packing. If lamellae are dedoped in post-treatment, the π-stacking remains, resulting in a novel PT crystal structure.

If the doping is removed by ethanol-rinsing after the synthesis, the PT chains tend to pack in their expected herringbone structure. However, the films synthesized under very high doping show the presence of a second, additional crystal structure. As a spectroscopic analysis proofs a strongly increased intermolecular interaction, it is assumed that the π-stacking in the highly doped PT remains even after dedoping. This novel crystal structure is assumed to be stable due to the reduced mobility of the chains in the thin films.

8. Reaction kinetics and film formation dynamics

Solution-based *in situ* polymerization techniques are much complexer processes than the coating of pure polymer solutions because chemical reaction and film formation are happening simultaneously. Consequently, more parameters play a role when it comes to tuning the properties of the resulting thin films. Since process control and reproducibility are of high interest for the fabrication there is an urgent need to understand the key processes taking place at the molecular level during the *in situ* polymerization. So far, there have only been few experimental approaches of tracking the film evolution with time. The degree of polymerization in solution-based processes is typically monitored by measuring the film absorbance at a characteristic wavelength of the polymer. [32, 56, 115] In vapor phase polymerization the reaction can be tracked by micro gravimetry which detects the increasing film mass with time. [92] The recording of time-resolved current-voltage characteristics gives an insight on the polymer growth during an electrochemical polymerization. [30] All of these approaches, however, only take into account the kinetics of the polymerization reaction and do not include the mechanisms of the morphology formation like polymer aggregation and film solidification.

In the scope of this project a novel approach of analyzing the reaction kinetics and film formation dynamics is developed by combining simultaneous time-resolved grazing incidence wide angle X-ray scattering (GIWAXS) and UV/Vis transmission measurements. In contrast to the approaches already presented in literature, UV/Vis spectra of a large wavelength range (300-900 nm) are recorded rather than the absorbance at a single photon energy. This enables not only the detection of growing polymeric species but also the uptake of reaction educts. GIWAXS is supposed to complement the gained knowledge on reaction kinetics by providing information on the film morphology at all times. For this purpose, the *in situ* polymerization is performed by deposition of the metastable reaction mixture with a slot-die printer. The printer setup at hand is designed for the purpose of *in situ* X-ray scattering and UV/Vis transmission measurements, in order to perform time-resolved experiments on the structure formation in solution-processed, organic thin films. [81]

As discussed in chapter 7, the molar ratio between monomer bithiophene (BT) and oxidizing agent iron p-toluenesulfonate (FeTos) employed in the metastable reaction mixture has a direct influence on the doping level that the polymer films obtain. Moreover, the aggregation of the doped chains happens in a different geometry as compared to the uncharged, neutral chains, resulting in a crystal structure with improved intermolecular interaction. In order to gain further insight on the impact of the doping process on the film formation, the time-resolved characterization of the *in situ* polymerization is performed by employing two different molar ratios between BT and FeTos, respectively. The first ratio of 1:3 is expected to result in a polymerization under oxidant excess as introduced in chapter 7. The second, 2:3, presumably gives PT films of intermediate doping level. In comparison to the theoretical stoichiometric ratio of the polymerization reaction (1:2), however, the second ratio still contains a deficiency of FeTos. For a clear differentiation between the two cases they will be referred to as *deficiency* (2:3) and *excess* (1:3) conditions within this chapter, respectively.

The overall aim of this project is to establish an experimental routine to track the film evolution with time and obtain an understanding of the relevant film formation phases. The fit models for analyzing the transmission and GIWAXS measurements are established in sections 8.1 and 8.2, respectively. Afterwards, the *in situ* polymerization under *excess* of FeTos is discussed in section 8.3, followed by the formation under *deficiency* in section 8.4. Finally, section 8.5 combines the results obtained for the two processes in order to formulate an overall model of the *in situ* polymerization of polythiophene thin films.

8.1. Tracking reaction kinetics with UV/Vis transmission

Time-resolved transmission measurements are performed to track the progress of the *in situ* polymerization reaction. All involved compounds, the educts bithiophene and Fe(III)Tos, and the resulting neutral and doped polythiophene, have characteristic absorbances which allow a quantitative analysis of the composition in solution and film throughout the whole process. The absorbance A of a chemical depends on its amount n in a medium as described by the Lambert-Beer law (equation 3.4). The proportionality factor connecting the two quantities is the absorption coefficient $\alpha(\lambda)$. In order to gain the wavelength-dependent absorbance of each of the involved species, transmission spectra of the single components are measured. Figure 8.1 displays the normalized absorbance spectra of all involved chemical compounds.

The absorbance spectrum of the monomer bithiophene in solution is shown in figure 8.1a. The maximum absorbance is at 302 nm, which is in agreement with literature values. [116] The absorbance spectrum is fitted with a sum of three Gaussian functions

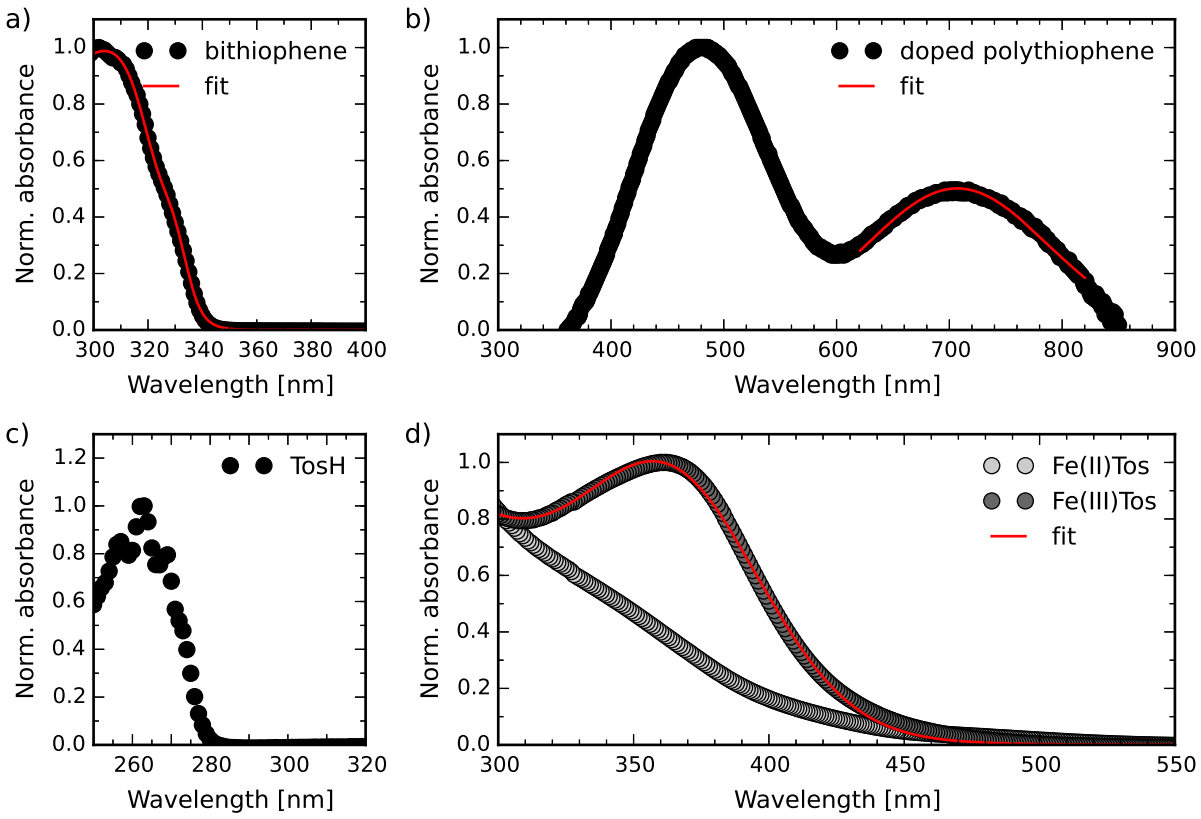

Figure 8.1.: Normalized absorbance spectra of single compounds of the polymerization reaction: a) solution of bithiophene in 1-propanol and corresponding fit function, b) thin film of doped polythiophene, c) solution of p-toluenesulfonic acid in 1-propanol, d) solutions of Fe(II)Tos (light grey) and Fe(III)Tos (dark grey) in 1-propapnol and corresponding fit functions.

to account for the different vibronic transitions of the respective band to obtain the absorption coefficient $\alpha_{\mathrm{BT}}(\lambda)$.

The oxidizing agent Fe(III)Tos consists of several absorbing species. In solution, the tosylate anions and the iron cations exist separated from each other, therefore giving rise to independent absorption bands. To investigate the decoupled tosylate absorbance p-toluenesulfonic acid is dissolved in 1-propanol. The main absorbing molecular component of the tosylate anion is its benzene ring, which absorbs in the UV region only up to a wavelength of about 280 nm (see figure 8.1c). Therefore, the tosylate absorbance is outside the energy range investigated here and will not be considered in the final model.

Fe^{3+} and Fe^{2+} ions on the other hand tend to form solvent complexes in solution which give rise to different types of electronic transitions. [77] The absorbance of the Fe^{3+} ions is determined by measuring the transmission of Fe(III)Tos dissolved in 1-propanol. Afterwards, the iron ions are reduced to Fe^{2+} by addition of zinc powder to obtain the respective spectrum of the iron complexes after their reaction with bithiophene. Both spectra are

displayed in figure 8.1d. The Fe(III)Tos spectrum shows two major absorbance bands, an intense one in the UV region and one at around 360 nm. The former is a *charge-transfer-band* associated to an electronic transition between the iron ion and a solvent ligand molecule, which is assumed to be constant for both oxidation states of the iron. [77] The latter corresponds to a d-d transition in the Fe^{3+} ion which vanishes upon reduction to $Fe^{2+}$and is therefore employed as a measure for the Fe^{3+} amount. [77] Overall, $\alpha_{\mathrm{Fe3+}}(\lambda)$ is fitted as a sum of two Gaussian functions corresponding to the two different electronic transitions, with the charge-transfer-band Gaussian kept constant for both oxidation states.

The absorbance of the organic reaction products is discussed in the following. Figure 8.1b shows the absorbance spectrum of a thin film of doped polythiophene. The two broad absorption bands correspond to two differently charged species of polythiophene. The lower wavelength absorbance around 480 nm is related to the excitation across the bandgap from HOMO to LUMO and is therefore attributed to the neutral, uncharged polythiophene chain. The doped, cationic polymer parts on the other hand show the absorption band of oxidized thiophene units at higher wavelength around 700 nm. [27] The intensity ratio between the two bands can be employed as a measure for the level of oxidation, i.e. doping level, of the polythiophene. [83] Therefore, $\alpha_{\mathrm{dopedPT}}(\lambda)$ is described by a single Gaussian function.

Nevertheless, it is not possible to segregate the neutral PT absorbance in the time-resolved absorbance spectra because the polymerization reaction is divided into several steps resulting in different (intermediate) products. At first, the bithiophene dimerizes to form a quaterthiophene molecule, which subsequently grows to oligothiophene chains of six, eight, and more thiophene units. Alongside the increase in conjugation length the bandgap of the molecule continuously decreases. Table 8.1 summarizes the absorbance maxima of oligothiophenes of two, four, and six units as well as of polythiophene in both solution and thin film. [116, 117]

Since the absorbance of all potentially present oligothiophenes expands from below 300 nm to beyond 500 nm, it is not possible to resolve the amount of actual polymer chains just by measuring absorbance spectra. Therefore, the sum of all of these species is considered as neutral oligothiophenes (in the following abbreviated as XT) with undefined conjugation length. Since the absorption strength of these is assumed to vary significantly, their absorption coefficient is simply accounted for as $\alpha_{\mathrm{XT}}(\lambda) = 1$.

The amounts that are determined in the following are not directly transferable to concentrations, since the single absorption coefficients do not contain information on the overall absorption strength of the molecules but simply describe the shape of their respective absorbances. This restriction arises mostly from the impossibility to resolve

Table 8.1.: Absorbance maxima of oligothiophenes of different chain length in solution (chloroform) and thin film. [116, 117]

	absorbance solution	absorbance film
bithiophene (2T)	302 nm	-
quaterthiophene (4T)	390 nm	448 nm
sexithiophene (6T)	432 nm	513 nm
polythiophene (PT)	-	486 nm

the different undoped oligothiophene species. Hence, all amounts derived are measured in arbitrary units. Nevertheless, the routine allows to track the evolution of the single chemicals throughout the polymerization.

The amounts are determined by the following procedure. For each measurement, the absorbance A is a sum of the all absorbances of the components in the film, i.e. the respective products of their amounts n_i and absorption coefficients $\alpha_\mathrm{i}(\lambda)$.

$$A(\lambda) = \sum n_\mathrm{i} \cdot \alpha_\mathrm{i}(\lambda) \tag{8.1}$$

Hence, it is possible quantify the single chemicals by fitting the respective parts of the spectrum.

undoped oligothiophenes
The sum of all undoped oligothiophene species n_XT is tracked by averaging the absorbance between 480 nm and 490 nm according to

$$\overline{A}(480\ nm - 490\ nm) = n_\mathrm{XT} \cdot \alpha_\mathrm{XT}. \tag{8.2}$$

doped polythiophene
The doped polythiophene chains are quantified by fitting the polaronic absorbance band between 600 nm and 900 nm with a Gaussian distribution function giving rise to $\alpha_\mathrm{dopedPT}(\lambda)$.

$$A(600\ nm - 900\ nm) = n_\mathrm{doped\ PT} \cdot \alpha_\mathrm{dopedPT}(\lambda) \tag{8.3}$$

BT and Fe^{3+}
The amounts of the reaction educts n_BT and $n_{\mathrm{Fe}^{3+}}$ are gained by fitting the absorbance between 285 nm and 384 nm. However, the absorption in that part of the spectrum is a superpositions of the Fe^{3+}, BT, and other uncharged oligothiophenes, whose absorbances are accounted for as well.

$$A(285\ nm - 384\ nm) = n_\mathrm{BT} \cdot \alpha_\mathrm{BT}(\lambda) + n_{\mathrm{Fe}^{3+}} \cdot \alpha_{\mathrm{Fe}^{3+}}(\lambda) + n_\mathrm{XT} \cdot \alpha_\mathrm{XT}(\lambda)\ . \tag{8.4}$$

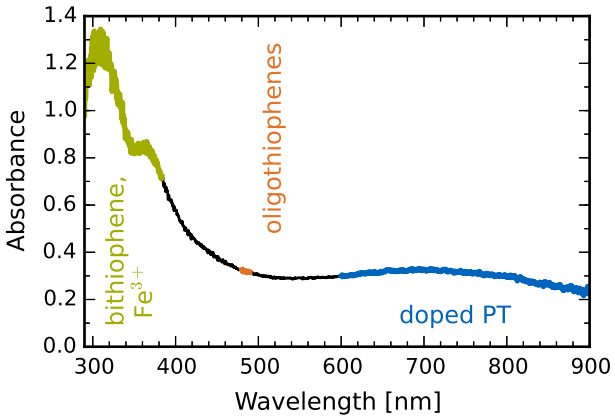

Figure 8.2: Exemplary absorbance spectrum of solution during polymerization reaction. The absorbance between 480 and 490 nm (orange) is averaged to calculate the amount of neutral oligothiophenes. The amounts of BT and Fe^{3+} are obtained by fitting the absorbance between 285 and 384 nm (green). Doped PT is quantified by fitting the polaronic absorbance between 600 and 900 nm (blue).

Figure 8.2 shows an exemplary absorbance spectrum taken from the *in situ* series to illustrate the parts of the spectra that are analyzed to quantify the amounts of the respective educts and products with time. Again, it should be noted, that due to the experimental procedure it is not possible to account for reflection, when the absorbance is calculated. Because of the measurement geometry the transmitted light can only be detected when the printing stage is in its final position. This is the case roughly two seconds after the solution deposition. The first dataset recorded in that position is set to be the starting point at $t = 0\,s$, the simultaneously recorded GIWAXS are correlated by identification of specific setup features appearing on the detector while the printer stage is still moving.

While the absorbance is used to determine the composition of the thin film at all times, time-resolved GIWAXS measurements are performed simultaneously to additionally obtain an insight on the morphology formation. The analysis of the resulting scattering data is outlined in the following section.

8.2. Following morphology formation with GIWAXS

Time-resolved GIWAXS measurements are performed simultaneously to the transmission measurements to gain an insight on the structure formation during the *in situ* polymerization of polythiophene thin films. In this section, the collected data are discussed with respect to the contained Bragg peaks as well as their origin. Figure 8.3 exemplary shows the results of static GIWAXS measurements recorded after the time-resolved measurements. Figure 8.3a shows a two-dimensional GIWAXS pattern of a thin film of polythiophene after the film formation is finished. First, this representation is utilized for a general overview of the present signals. Afterwards, the signals are analyzed in more detail by means of the radial intensity profiles presented in figure 8.3b.

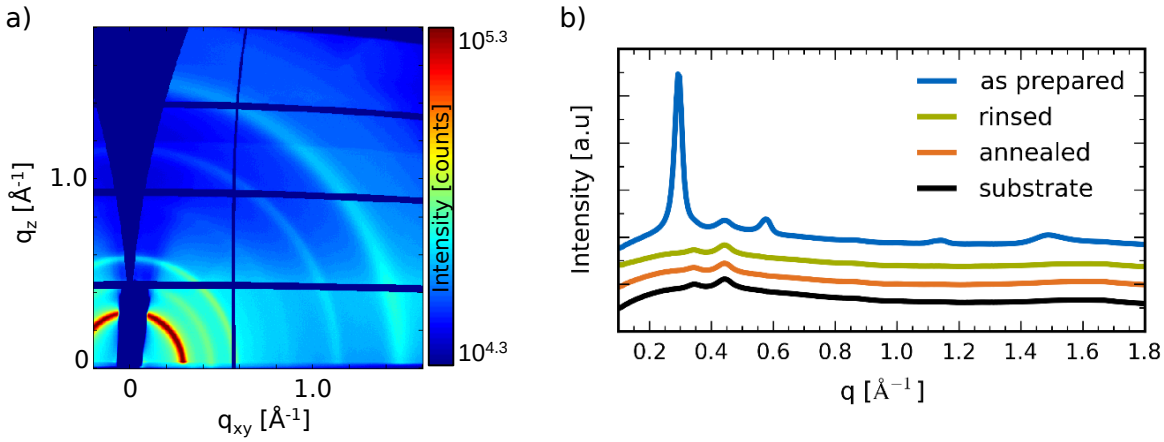

Figure 8.3.: Exemplary GIWAXS data of thin films obtained from *in situ* polymerization: a) two-dimensional GIWAXS pattern of as-prepared thin film b) radially integrated intensities of thin films as-prepared (blue), after ethanol-rinsing (green), after additional annealing step (orange), and PEDOT-coated substrate (black). Data shifted with respect to each other for a clearer presentation.

The measured raw data are converted into q-space for analysis, which gives rise to the missing wedge that is visible in figure 8.3a. After the conversion, the two dimensional data are displayed in a coordinate system of q_{xy} and q_z, respectively. The intensity of direct and specular beam are blocked by the rod-like beam stop, that is located at the origin of the coordinate system. The scattering pattern displayed here features several anisotropic Bragg rings of different intensity. The most intense one is found at $q = 0.3$ Å^{-1}. Moreover, two intensity artifacts have to be taken into account for the necessary data reduction. Firstly, the intensity in z-direction directly above the beam stop is decreased, presumably due to a shading invoked by the shape of the beam stop. Secondly, the intensity is increased on the right of the beamstop. This effect is assumed to be an artifact of the beamline, as it is observed without insertion of a beam stop as well. Therefore, the scattering intensities in the different directions (i.e. horizontal and vertical) are not examined separately, but the radial integrations are performed between polar angles of $\chi = 20°$-$85°$. For this reason, a detailed orientation analysis of the seemingly isotropic signals is not performed.

As aforementioned, the data are reduced by a radial integration for a more detailed analysis. The resulting intensity profiles are displayed in figure 8.3b. In order to assign the visible peaks to a material in the thin films, the cuts of films at different stages of preparation are compared. The graph shows the scattering intensities obtained from static GIWAXS measurements on a PT film directly after preparation (blue, obtained from the

2d pattern in figure 8.3a), after rinsing with ethanol (green), and after a final annealing step (orange). Moreover, the cut of the purely PEDOT-coated substrate is plotted as well (black). Comparing the cuts, there are two peaks that are present for all samples. The peaks located at q-positions of 0.35 and 0.44 $Å^{-1}$ are attributed to the Kapton® entrance and exit windows of the printer setup. Hence, they are not part of the scattering pattern of the thin films. Other than these, there are no additional peaks in the cuts of the substrate, the rinsed, and the annealed PT film. Strangely, the cuts do not feature the typical PT peaks which are observed in the static GIWAXS measurements discussed in chapter 7 at $q = 1.40\,Å^{-1}$, $1.63\,Å^{-1}$, and $1.98\,Å^{-1}$. While these might too weak and therefore be covered by other signals in the as-prepared sample, it is not clear why they are not present in the rinsed and annealed films. As a consequence, it is not possible to track the time-resolved aggregation of the polymer chains within the films.

In the as-prepared film several peaks can be observed that correspond to the isotropic rings found in the 2d data. The peaks are found at scattering vectors of $q = 0.29$, 0.58, 1.14, and $1.48\,Å^{-1}$. As they do not show up in any of the post-treated films, the respective crystalline material is rinsed out in the washing step. Since the insoluble polythiophene remains on the substrate, the only soluble parts in the as-prepared films are the residuals of the educts, BT and FeTos in its two different oxidation states. Since the measurement is performed right after the film preparation, the substrate is still kept at a temperature of 85 °C. Due to the melting temperature of bithiophene (33 °C) it is expected to remain liquid or at least without any long-range order within the films. Hence, the signals are assigned to the FeTos crystals forming during the film formation, when the solvent evaporates. Since an in-depth analysis of the respective crystal structure is not of interested in the scope of this project, only the most intense peak is employed for tracking the crystal growth of the oxidizing agent during the film formation in order to indirectly observe the transformation of the solution to solid film. The peak position of $q = 0.29\,Å^{-1}$, corresponds to a real space lattice distance of 2.17 Å and is therefore on the order of magnitude of metal-metal distances in metal ion tosylate complexes. [118]

For analyzing the FeTos crystal growth with time, the cuts are corrected by subtraction of a local background around the peak. For this purpose, a linear regression is performed between the intensities at $q = 0.20\,Å^{-1}$ and $q = 0.40\,Å^{-1}$, and the resulting function is subtracted from the original data. This local background is supposed to take into account all the scattering contributions that are present in that q-region, such as the exponentially decaying GISAXS signal, potential scattering of amorphous material in the film, and background scattering from the substrate or the setup. Afterwards, only the crystalline FeTos peak remains. This peak is subsequently fitted with a Gaussian distribution to obtain its center, intensity, and full width at half maximum (FWHM).

In summary, the time-resolved GIWAXS measurements allow to indirectly track the evolution of the thin film morphology during *in situ* polymerization by visualizing the crystal growth of FeTos. In combination with the transmission measurements, the analysis of the GIWAXS data is employed to gain an insight on the reaction and film formation kinetics.

8.3. Film formation under oxidant excess conditions

This section investigates reaction dynamics and film formation of an *in situ* polymerization under excess of oxidizing agent. As shown in chapter 7, a molar ratio of BT to FeTos of 1:3 yields to polythiophene films with high doping level. For an optimization of the processing parameters and the resulting film properties, it is of high importance to gain an insight on the different phases during the fabrication. While section 8.3.1 deals with the kinetics of the chemical reaction as tracked by transmission spectroscopy, the film formation is analyzed by GIWAXS in section 8.3.2. Finally, a model of the *in situ* polymerization process under FeTos excess is drawn in section 8.3.3.

8.3.1. Reaction rates of polymerization and doping

Time-resolved transmission measurements are performed to track the progress of the polymerization reaction. Figure 8.4 shows the resulting transmission (a) and absorbance (b) spectra recorded during a time of 200 seconds. As discussed in the previous chapter, the educts of the polymerization reaction (BT and Fe^{3+}) absorb only in the low wavelength regime of the visible spectrum as well as in the ultraviolet, while both the doped as the undoped oligo- and thiophenes can be tracked by analyzing the absorbance at wavelengths above 450 nm.

The absorbance spectrum at t = 0 s already features the contributions of all compounds, both educts and products. Hence, the reaction has started prior to the data collection. In the first few seconds the contributions of BT and Fe^{3+} still decrease rapidly, until they seem to stay at an almost constant amount after about half of the investigated reaction time (bright green curves). The intensity around 480-490 nm is already close to its final value at the beginning, and only increases further in the first few seconds, indicating the formation of neutral oligothiophenes. Moreover, the polaronic band of the doped PT is already clearly visible in the beginning. Furthermore, it does not only show the expected increase in the first few seconds (dark blue curves) but seems to drop again in the end (from bright blue to yellow curves). In the following, the evolution of the amounts of the different compounds will be discussed in detail.

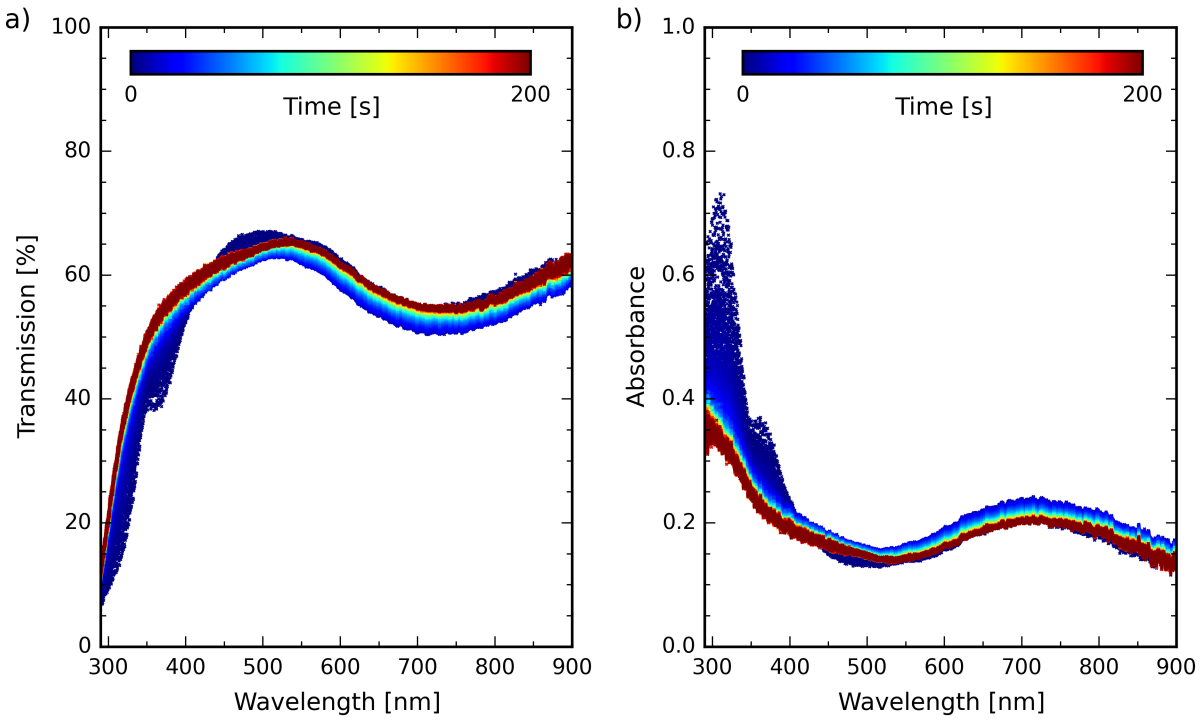

Figure 8.4.: Time-resolved UV/Vis spectroscopy data measured during *in situ* polymerization under FeTos excess; a) transmission spectra, b) absorbance spectra obtained from transmission after background correction.

Figure 8.5 contains the fit results obtained for the absorbance spectra of the first 200 s after the beginning of the data collection. Figure 8.5a shows absorbance spectra measured every ten seconds shifted with respect to each other for a clearer presentation. Additionally, the black curves represent the obtained fit functions derived in the respective considered parts of the spectra as introduced in the previous section. Clearly, the black curves sufficiently match the original datasets. Therefore, we can assume that the established fit model can adequately describe the composition of solution and forming film throughout the whole investigated time frame. Additionally, the amounts of the compounds that are obtained from the fits are given for the educts (subfigures a and b) and the products (subfigures d and e). As discussed in section 8.1, these values are not factual amounts but prefactors to the absorbances, that are approximately proportional to the real amounts. Therefore, the absolute values of the different components cannot be compared directly.

The development of the educt amounts (figures 8.5b and c) will be discussed first. Both compounds show a similar evolution throughout the polymerization and film formation. As expected, both amounts constantly decay throughout the course of the reaction, with fast uptake rates in the first few seconds, followed by intermediate decays until the end

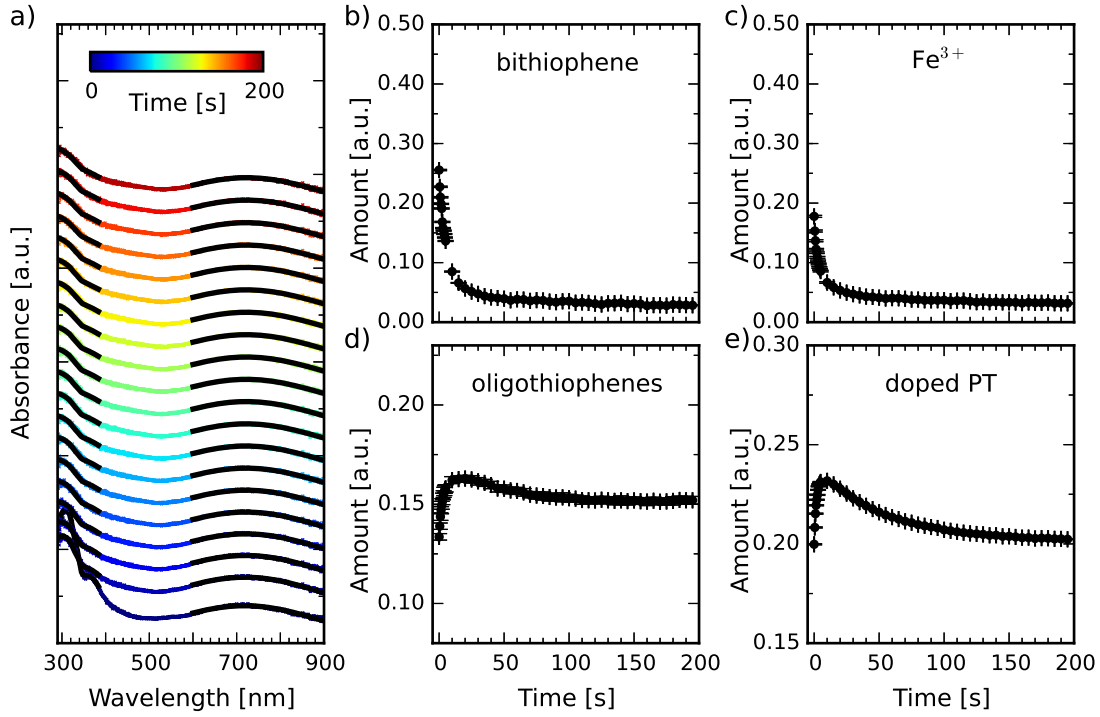

Figure 8.5.: Fit results of time-resolved absorbance spectra recorded during *in situ* polymerization under FeTos excess; a) selection of absorbance spectra of every 10 s and resulting fit curves (black) shifted along the y-axis, b-e) evolution of amounts of bithiophene (b), Fe^{3+}(c), oligothiophenes (c), and doped polythiophene (d) as determined by fit function. Error bars correspond to time resolution in horizontal and fitting inaccuracies in vertical direction, respectively.

of the first half minute, and a very slow rate converging to the final values in the end. At t = 0 s, the amounts of BT and Fe^{3+} are (0.255 ± 0.002) a.u. and (0.178 ± 0.002) a.u., respectively. The errors result from fitting inaccuracies. As discussed before, these are not the inital values of the metastable reaction mixture, since the polymerization reaction has already started prior to the data collection. Hence, it is not possible to determine the educt uptake before the first measurement. Within the first ten seconds of data collection, however, the educt amounts are reduced to (0.085 ± 0.001) a.u. (BT) and (0.067 ± 0.002) a.u. (Fe^{3+}). Therefore, both BT and Fe^{3+} decrease to about one third of their initial amounts in only ten seconds. In the phase of intermediate uptake rate (until t = 40 s) the amounts further decay to (0.042 ± 0.001) a.u. and (0.043 ± 0.002) a.u.. Finally, at around t = 100 s, the educts reach their final amounts without any further significant decay. Both BT and $Fe^{3+}$are not taken up completely, but remain in small amounts within the film. The monomer bithiophene is reduced to an amount of (0.029 ± 0.001) a.u., i.e. about 11 % of the initially measured amount. The Fe^{3+} ions finally remain at (0.031 ± 0.002) a.u. and are therefore reduced to 17 %.

Figures 8.5d and e illustrate the evolution of the reaction products with time. While subfigure d displays the amount of the undoped oligothiophenes, the amount of doped PT is shown in subfigure e. Both products are already present at t = 0 s, but still show a strong increase in the first few seconds. After this expected growth of the polymeric species, both already reach a maximum. Afterwards, they decay until they reach their final value after about 100 seconds. At the beginning of the data collection, the amount of the undoped oligothiophenes is (0.134 ± 0.002) a.u. They increase to (0.162 ± 0.002) a.u. within the first ten seconds, reaching their absolute maximum throughout the whole process. Afterwards, they first decay with a slow and steadily decreasing rate to their final value of (0.153 ± 0.002) a.u. Hence, the maximum amount is reduced again by about 5.6 %.

The doped polythiophene chains (figure 8.5e) behave in a very similar way, with a starting amount of (0.200 ± 0.001) a.u.. They show a rapid increase to (0.232 ± 0.001) a.u. at t = 10 s, which is the maximum amount present during the film formation process. Afterwards, they are decreased again with an intermediate rate until t = 50 s and a very slow decay thereafter, reaching their final amount of (0.203 ± 0.001) a.u. after approximately 150 s. The amount of doped PT is therefore decreased by 12.5 % after its maximum.

Putting these observations together, it is possible to follow the progress of the different steps of the polymerization and doping reactions under FeTos excess. As the starting values of the products suggest, the reaction already starts before the data collection begins at t = 0 s. At the selected starting time, both doped and undoped oligo- or polythiophenes are already at more than 80 % of their detected maximum during the observed time. Obviously, the educts are already decreased by a large amount. Nevertheless, the fit results give an important insight on the reaction dynamics under FeTos excess. In the first ten seconds, the rate of the polymerization and doping reaction are very high, as indicated by the drastic decrease of the educts as well as the corresponding fast increase of the polymeric products. Afterwards, however, all the considered chemical compounds of the reaction show a slow decay. The reduction of the educts, BT and Fe^{3+}, indicate a further proceeding of the polymerization reaction at a strongly reduced speed. Nevertheless, this cannot be confirmed by the results obtained for the polymers, since neither contribution shows an increase. The reduction of the doped PT contribution can be explained by an initial overoxidation to a high doping level within the first seconds. This overoxidation could be the result of a faster oxidation or doping step as compared to the formation of a new covalent bond between the resulting radical oligo- or polythiophene radicals. Therefore, the polymerization reaction is supposed to continue even after there is no further significant decay in the educts, since there are enough "activated" polymer chains already present in the film. This ongoing formation of polymer bonds, however,

cannot be confirmed by the results obtained for the undoped oligothiophenes. In principle, these are expected to show an increase upon the conversion from two charged thiophene units to the uncharged, bonded molecule. However, the absorbance between 480 and 490 nm decreases further as well. It is assumed, that this decrease in absorbance and therefore seemingly amount of undoped oligothiophenes originates in the structure of the molecules. It is known, that the order and type of aggregation as well as the chain and conjugation lengths have a significant impact on both absorbance shape and absorption coefficient of semiconducting polymers. [88, 119, 120] Due to the superposition of the different absorbances in the spectra, however, it is not possible to resolve the character of the undoped oligothiophene absorbance.

The final amounts of the uncharged oligothiophenes and the doped PT can be employed, to make an assumption on the doping level of the eventual films. For this purpose, the ratio of doped to undoped is calculated to be 1.33. While this value does not represent a real physical quantity, it can be used as an estimate of the doping level, when the *in situ* polymerization under FeTos excess and deficiency are discussed in section 8.5.

In summary, the time-resolved transmission measurements give an insight on the different reaction rates of doping and polymerization during the *in situ* polymerization of polythiophene thin films under excess of the employed oxidizing agent FeTos. For a more detailed insight on the different phases of the film formation, the morphology evolution is tracked and analyzed by means of GIWAXS. The results of the corresponding measurements are discussed in the following section.

8.3.2. Evolution of morphology: crystallization of FeTos

In this section, the dynamics of the film formation during *in situ* polymerization under excess of FeTos are investigated by means of time-resolved GIWAXS measurements. For this purpose, the measured two-dimensional data are reduced by radial integration and corrected with a local background as described in section 8.2. Figure 8.6 displays the resulting cuts over a large q-range (a) and the background-corrected peak of the crystalline FeTos (b). Other than in the transmission measurements, only the first 25 s of the reaction are tracked by GIWAXS.

In the cuts it is clearly visible that all appearing signals are already present at the beginning of the data collection. Hence, FeTos starts to crystallize immediately in the first moments after the deposition of the metastable reaction mixture. Since FeTos is completely soluble at the employed concentration, no crystals are expected to be present in the metastable reaction mixture. Therefore it is concluded that parts of the solvent

have already evaporated before the data collection. This leads to an increased FeTos concentration beyond the solubility limit already at $t = 0\,s$.

A closer look at the peak after background correction (figure 8.6b) already reveals that its center is shifting to smaller q-values in the first few seconds (blue to bright green curves) while it still gains intensity. The fitting results presented in figure 8.7 give a more detailed insight on the evolution of the FeTos crystals with time. The gaussian fits give rise to information on the amount of crystals or crystalline material in the thin film (figure 8.7a), the center of the peak in q-space (figure 8.7b) is inversely proportional to the real space crystal lattice distance that corresponds to the peak, and the FWHM of the gaussian can be employed to extract a lower limit of the present average crystal size by application of the Scherrer equation (equation 3.16). The fit results of the final static measurement (black curve in figure 8.6) are not displayed in the plots, as they cannot be attributed to a distinct point in time. Nevertheless, it will be taken into account in the discussion in this section as well as for the formulation of the final model in section 8.3.3.

The evolution of each parameter will be discussed individually, before a complete interpretation is proposed. The intensity of the FeTos peak under investigation is already at (157 ± 5) counts at $t = 0\,s$. In the first three seconds the intensity increases rapidly to (187 ± 6) counts. Thereafter, the increase in intensity is reduced to an intermediate level, until it reaches (211 ± 6) counts at $t = 10\,s$. In the last phase of the time-resolved measure-

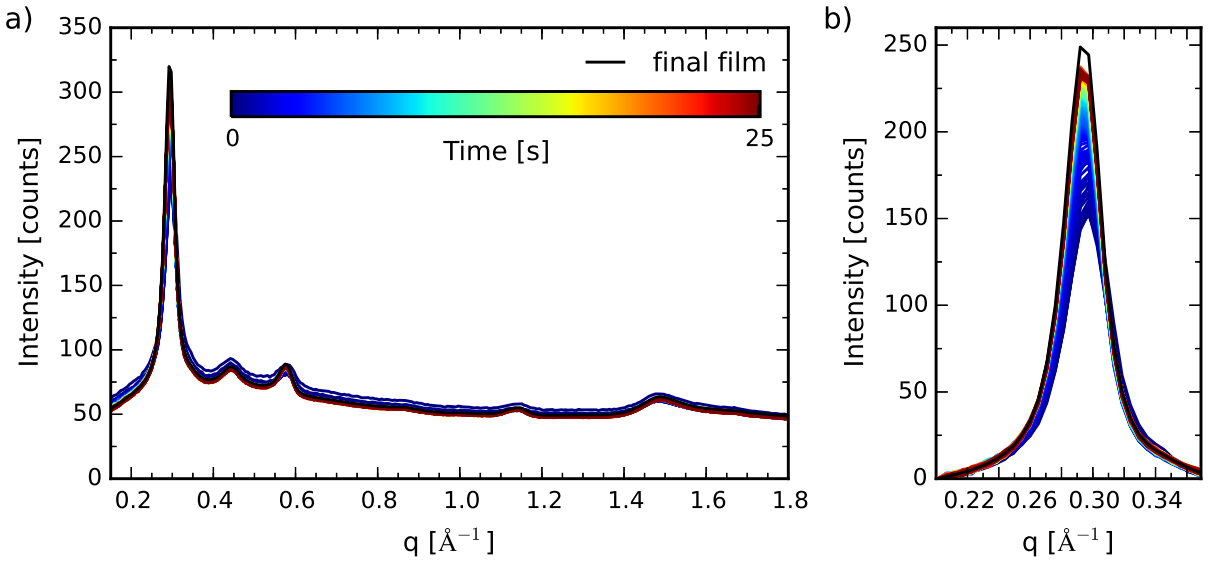

Figure 8.6.: Time-resolved GIWAXS measurements of *in situ* polymerization under FeTos excess. a) Radially integrated intensities of 2d data, b) FeTos peak after subtraction of local background. In both plots the time-resolved measurements are displayed in colors, while the static measurement after the film deposition is plotted in black.

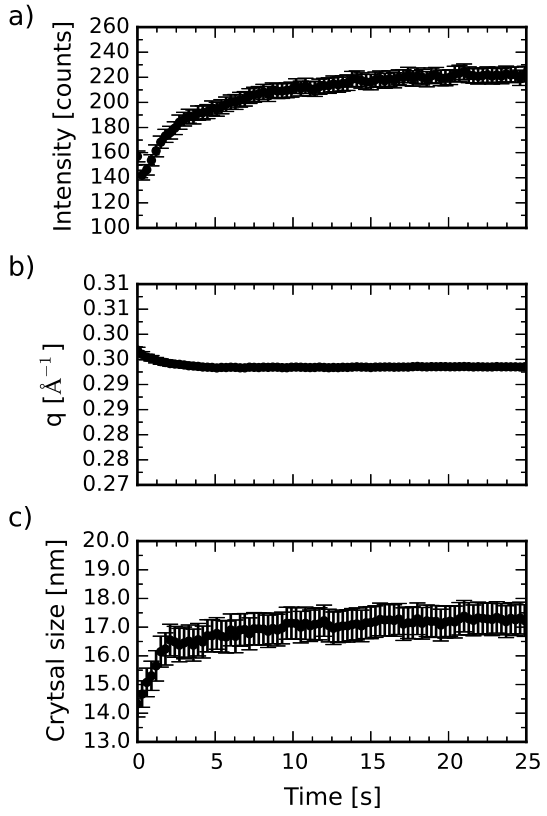

Figure 8.7: Evolution of the parameters extracted from the Gaussian fits of the FeTos peak: a) peak intensity as a measure of the amount of crystalline material in the film; b) peak position, which is inversely proportional to the real space distance between the iron ions in the FeTos crystals; c) crystal size calculated from the FWHM by the Scherrer equation. Error bars correspond to time resolution in horizontal and fitting inaccuracies in vertical direction, respectively.

ments the intensity only increases very slowly to (223 ± 7) counts. Finally, the peak only gains a final intensity of (237 ± 7) counts as determined in the subsequent static measurement. Hence, most of the crystalline material is formed between the solution deposition and the first few seconds of the data collection.

The position of the peak and therefore the corresponding distance between the iron ions only changes slightly within the investigated time frame. At t = 0 s, the peak is centered at a scattering vector of $q = (0.297 \pm 0.001)\,\text{Å}^{-1}$. Within the first few seconds, the peak shifts to $(0.294 \pm 0.001)\,\text{Å}^{-1}$ and stays at that value until the final static measurement. The change happening at the beginning of the reaction, however, only corresponds to an increase in real space distances from 2.12 Å to 2.14 Å and is therefore not considered to be significant.

The average crystal size of the FeTos crystals in the film shows a rapid increase in the first three seconds. The crystals quickly grow from (14.3 ± 0.5) nm (t = 0 s) to (16.5 ± 0.6) nm (3.0 s). After that period, however, the crystal growth is abruptly decreased to a slower speed, resulting in a crystal size of (17.1 ± 0.6) nm after ten seconds of measurement. Finally, the crystal size only very slowly increases further to (17.2 ± 0.6) nm at 25 s and (17.6 ± 0.6) nm in the final state.

Overall, the growth rates of the FeTos crystals enable to draw a picture of the structure

formation from reaction mixture to polymer thin film. In the first phase after the deposition a certain fraction of the solvent quickly evaporates, resulting in the crystallization of FeTos due to an increased concentration. Therefore, there are already crystals present at t = 0 s. In the first three seconds, the size as well the the amount of crystals still increases rapidly. Thereafter, the speed of the crystal growth decreases very abruptly. Hence, it is assumed that most of the solvent has evaporated after that time, limiting the further crystal growth to a minimum. However, the results of the time-resolved GIWAXS measurements need to be put in context with the corresponding transmission data to derive an overall model of the film formation under FeTos excess. This will be done in the following section.

8.3.3. Reaction and film formation dynamics

In the two previous sections, the results of the time-resolved transmission and GIWAXS measurements have been discussed separately. Now, these results will be combined to formulate a model of the film formation process during the *in situ* polymerization of polythiophene under excess of oxidizing agent FeTos. For this purpose, some of the parameters obtained from the analyses are normalized to their respective initial (educt amounts) or final values (product amounts, FeTos crystal parameters) and put together in figure 8.8. Each parameter is plotted in two separate graphs with different time scales to account for the fast changes in the beginning of the film formation (figures 8.8 a, c, e, and g) as well as the slower changes happening in the first minutes (figures 8.8 b, d, f, and h). Since the changes in the amounts as discussed in section 8.3.1 do not show any significant changes after about 170 s, the results are not plotted beyond that, assuming that the film formation process is at its end. Therefore, the results of the static GIWAXS measurements are appended to the plots at 170 s to account for the final structure of the film.

The chemical conversion of bithiophene to polythiophene is tracked by analyzing the evolution of the amounts of the educts BT and Fe^{3+}(figures 8.8a and b), each normalized to its respective initial value, and the amount of doped PT (figures 8.8c and d), normalized to its final value. The transition from solution to solid film is taken into account by means of the crystallization of FeTos. Here, the scattering peak intensity (figures 8.8e and f) and the crystal size (figures 8.8g and e), each normalized to its respective final value, are of special interest. The process is divided into four different stages I_e - IV_e (e: FeTos *excess* conditions). These will be explained in further detail in the following by discussing the behavior of the single parameters with time.

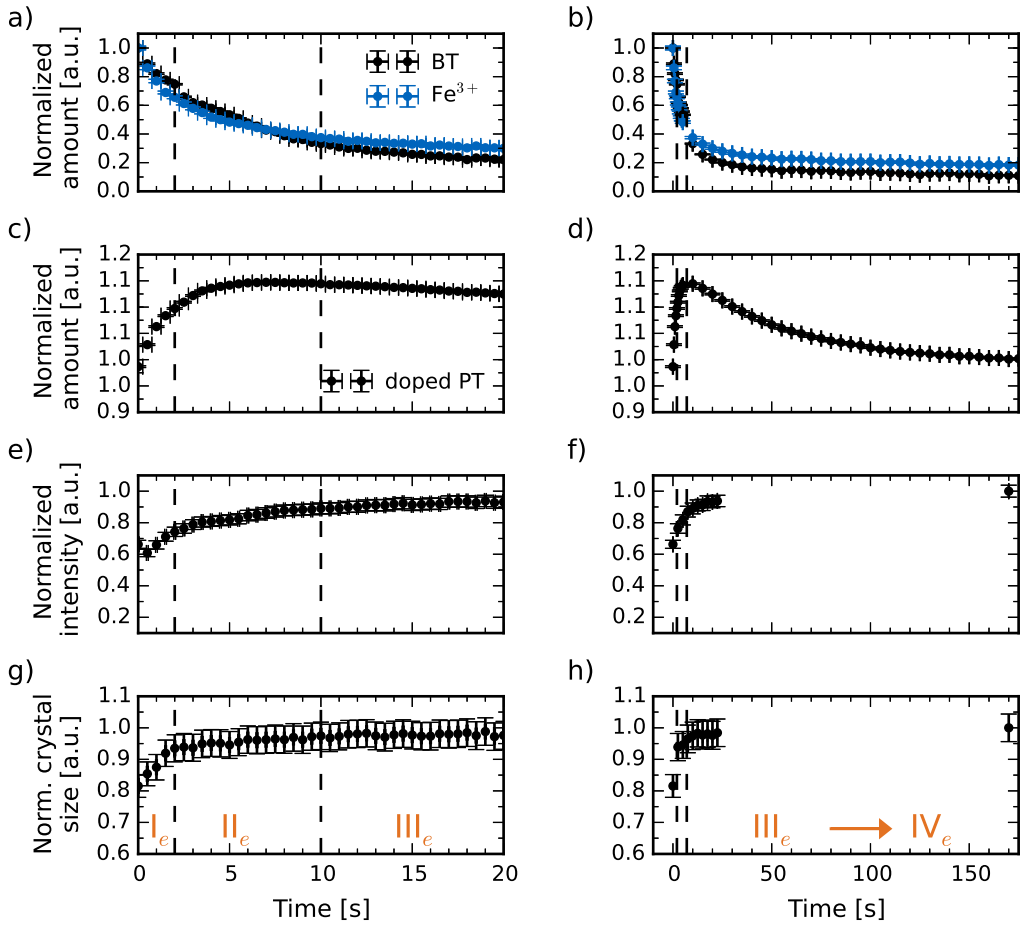

Figure 8.8.: Evolution of the normalized parameters of the *in situ* polymerization under FeTos excess, extracted from the respective fits of the time-resolved absorbance and GIWAXS data. Each parameter is plotted with high time resolution for the first 20 seconds (left) and lower time resolution for 175 seconds (right). a,b) Amounts of educts bithiophene (black) and Fe^{3+}(blue) from absorbance, c,d) amount of doped polythiophene from absorbance, e,f) scattering intensity of FeTos peak from GIWAXS, g,h) crystal size of FeTos crystals from GIWAXS. The process is divided into four different stages, that are separated by dashed vertical lines and labeled accordingly. Error bars correspond to time resolution in horizontal and fitting inaccuracies in vertical direction, respectively.

$\mathbf{I}_e$: *Fast polymerization and solvent evaporation*

In the first phase, from the beginning of the data collection to t = 3 s, all the parameters show the fastest change. Both educts have a steep decrease, while the amount of doped PT strongly increases. At the same time, the crystallization of FeTos is still very fast, with a gain of peak intensity and crystal size. These observations suggest the presence of sufficient solvent to enable high molecular mobilities for either chemical reactions or

crystal growth. Nevertheless, this phase must have started before the data collection, since FeTos crystals and doped PT are already present at t = 0 s.

II_e: *Decreased reaction rates and solidification*

In the subsequent second phase all the changes are reduced to an intermediate speed. The change is most clearly visible in the FeTos crystal size and in the amount of doped PT. The amount of both educts further decreases, accompanied by a further gain of the doped polymer. Hence, both chemical processes of polymerization and doping are still taking place, but at a decreased rate. The abrupt change in the crystallization behavior of FeTos at the beginning of the phase indicates a significant change in the dynamics of the system. While an inhibited crystallization could be the result of a depletion of the respective ions in the solution, the ongoing uptake of Fe^{3+} established by its absorbance contradicts this. Hence it is assumed that the decreased crystallization rate is caused by the evaporation of most solvent molecules. The transition from phase I_e to phase II_e is therefore also the transition from solution to a mostly solid film, in which only the leftovers of the liquid monomer BT provide the remaining molecular mobility for ongoing polymerization and crystallization processes at reduced rates. The second phase ends at about t = 10 s, when the amount of doped PT reaches its maximum.

III_e: *Polymerization of overoxidized chains*

In the third phase of the film formation the amount of crystalline FeTos still steadily increases, although the average crystal size does not show any further significant growth. The time-resolved data expire during this phase, but it is assumed that the peak intensity keeps increasing at a continuously decaying rate until it reaches its final value. Interestingly, however, the amount of doped PT decreases in the third phase. Therefore it is concluded that while the oxidation process itself is still comparably fast in the previous phase II_e, the dimerization of "activated" cationic chains is already reduced by their low mobility, resulting in an overoxidation of the polymers. Nevertheless, the steady decrease in the amount of doped PT suggests a slow ongoing bond formation between spatially close charged chains in the system. This phase lasts from t = 10 s to approximately t = 100 s.

IV_e: *Final film formation and reaching of equilibrium doping level*

The transition between the stages III_e and IV_e is evident in the decreasing rate of the reduction of doped PT. The educts are already at their final amounts at the beginning of the phase. Therefore, no formation of new polymer chains from BT is happening after 100 seconds. There is a minor gain in FeTos scattering intensity from the end of the time-resolved data to the final static measurement which is assumed to happen in the

phases III_e and IV_e. Apparently, this phase is a final relaxation to the equilibrium doping level that is obtained under the employed monomer to oxidant ratio of 1:3.

In summary, the combination of the time-resolved GIWAXS and transmission measurements allows to reveal the dynamics of an *in situ* polymerization of polythiophene under excess of oxidizing agent FeTos. A four-stage film formation model is proposed, in which the rapid reactions in the solution and a decrease in the rates upon drying of the film is evident. Also, the excess of Fe^{3+} ions in the reaction mixture results in an overoxidation of the polymer chains, which later relaxes to the finally stable doping level. The results of the film formation under excess will be revisited in section 8.5, when the two film formation processes are brought together to formulate one model.

8.4. Film formation under oxidant deficiency conditions

This section investigates the reaction dynamics and film formation of an *in situ* polymerization under deficiency of oxidizing agent. The results of chapter 7 suggest that the molar ratio 2:3 of BT to FeTos should result in an intermediate doping level, as compared to the ratio employed in section 8.3. Again, the reaction rates are investigated by means of time-resolved transmission measurements in section 8.4.1, while the film formation dynamics are analyzed by GIWAXS in section 8.4.2. The overall model of the polymerization and film formation is proposed in section 8.4.3, bringing the observations of the two measurement techniques together.

8.4.1. Reaction rates of polymerization and doping

Time-resolved transmission measurements are performed during the *in situ* polymerization to track the progress of both the reaction as well as the doping. Figure 8.9 shows the transmission (a) and resulting absorbance spectra (b) during the first 200 s of the process. Employing the fit model set up in section 8.1, the amounts of the educts are determined by tracking the absorbance in the low wavelength regime of the visible spectrum and in the ultraviolet, while the amounts of doped and undoped PT are obtained at wavelengths beyond 450 nm.

A qualitative analysis of the absorbance spectra already provides some information on the progress of the reaction at different times. The first spectrum features only the absorption bands of the two educts, showing no sign of any polymer absorbance at higher wavelengths. Hence, in this experiment the chemical reactions have not yet started at the beginning of the data collection. Within the first few seconds (dark blue spectra), however, the absorption band of the doped PT rapidly increases. At the same time, the monomer

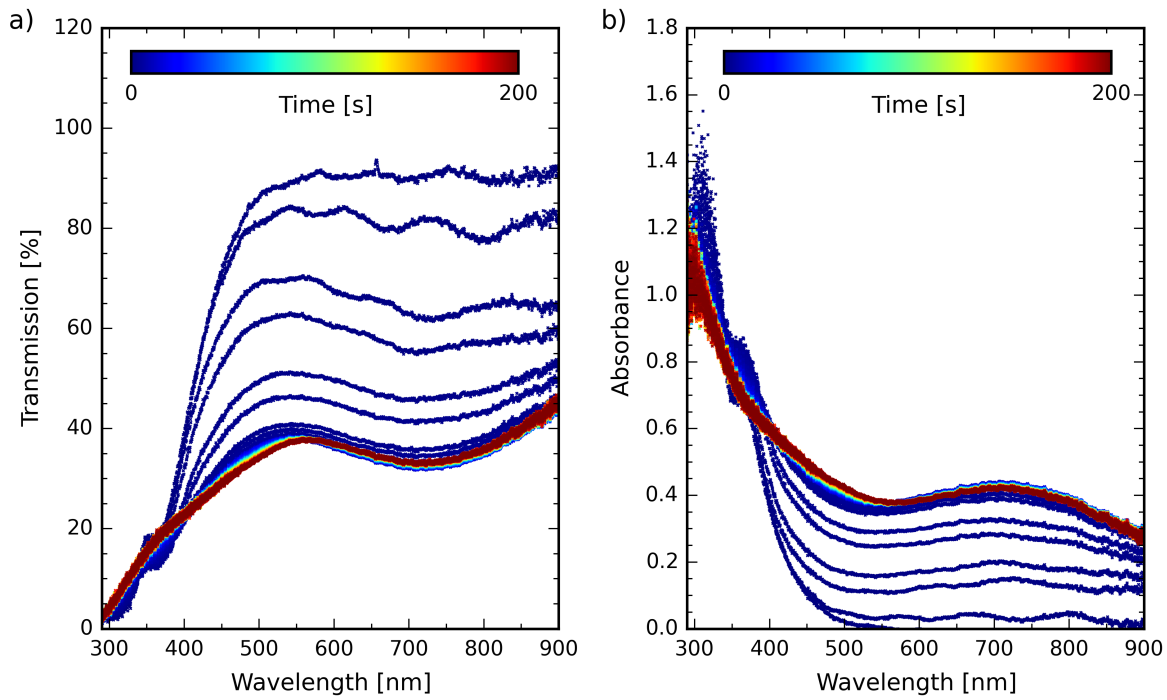

Figure 8.9.: Time-resolved UV/Vis spectroscopy data measured during *in situ* polymerization under FeTos deficiency; a) transmission spectra, b) absorbance spectra obtained from transmission after background correction.

absorbance around 300 nm decreases. At first sight, the absorption of the Fe^{3+} ions seems to increase at first, before it finally drops again. However, the contribution of the undoped oligothiophenes has to be considered in this wavelength regime as well. Therefore, the proposed fit model is applied for a quantitative analysis of the compounds. The results are presented in figure 8.10 and discussed in the following.

Figure 8.10a shows the absorbance spectra for every ten seconds, shifted with respect to each other for a clearer presentation. Additionally, the black curves represent the resulting fits for the respective parts of each spectrum. Again, the applied fit model sufficiently describes the original data throughout the whole analyzed time frame, verifying its validity for the investigated process. The resulting amounts for the educts BT and Fe^{3+} are given in figures 8.10b and c, while the evolution of the product compounds is given in 8.10d and e.

The course of the educt amounts will be discussed first. As the qualitative interpretation of the spectra already showed, the reaction mixture is mainly composed of the educts in the beginning. In the course of the process BT and Fe^{3+} follow a similar evolution. They are consumed in the chemical reactions at an initially fast rate in the first few seconds. Thereafter, their decay drops to an intermediate rate for about half a minute and

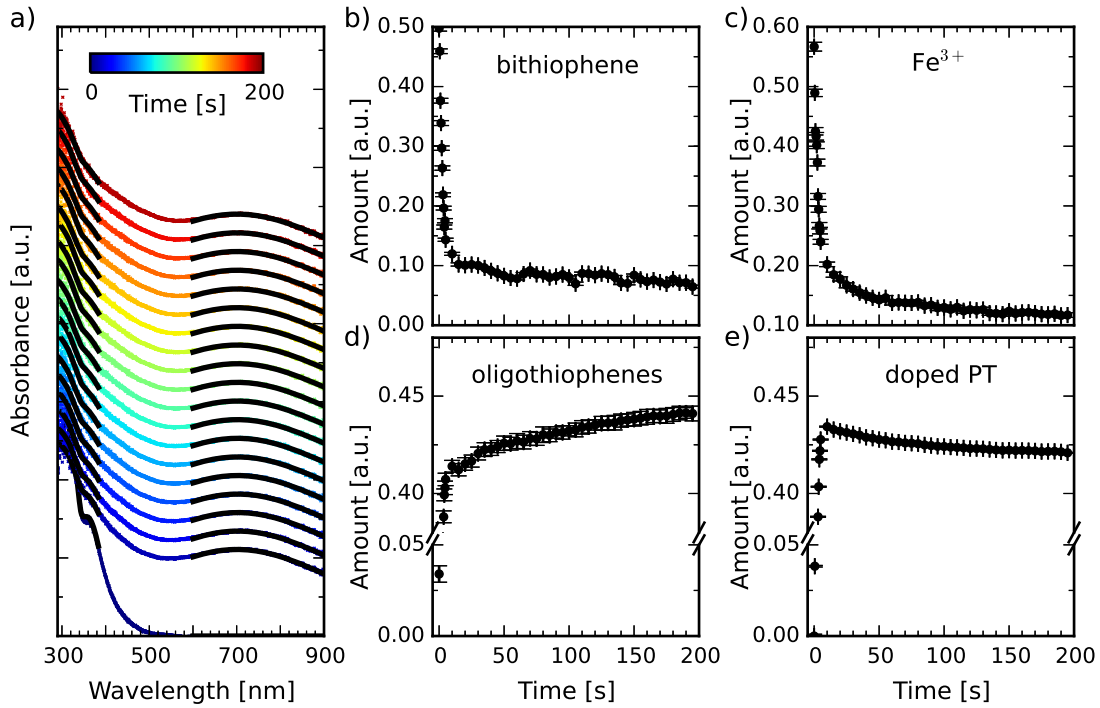

Figure 8.10.: Fit results of time-resolved absorbance spectra recorded during *in situ* polymerization under FeTos deficiency; a) selection of absorbance spectra of every 10 s and resulting fit curves (black) shifted along the y-axis, b-e) evolution of amounts of bithiophene (b), Fe^{3+}(c), oligothiophenes (c), and doped polythiophene (d) as determined by fit function. Error bars correspond to time resolution in horizontal and fitting inaccuracies in vertical direction, respectively.

finally to a very slow ongoing reduction until the end of the investigated time. At $t = 0\,s$, (0.498 ± 0.005) a.u. of BT are present in the solution. For the monomer, the very fast uptake lasts for approximately seven seconds, resulting in an amount of (0.136 ± 0.003) a.u. ($t = 7.0\,s$). The oxidant ions Fe^{3+} decay from (0.567 ± 0.008) a.u. to (0.223 ± 0.005) a.u. in the same time frame. In the phase of intermediate uptake which lasts to about $t = 30\,s$, they both further decay to (0.100 ± 0.003) a.u. (BT) and (0.161 ± 0.004) a.u. (Fe^{3+}), corresponding to fractions of 20 % and 28 % of their initial values, respectively. Finally, the speed of the educt decays is continuously reducing to a minimum, with the respective amounts reaching their final values after about two minutes of measurement time. Eventually, the residual amounts of BT and Fe^{3+} which stay in the formed films are (0.069 ± 0.003) a.u. and (0.116 ± 0.004) a.u.

The development of the product amounts with time is illustrated in the plots in figures 8.10d and e. For both, the data is displayed in graphs with broken y-axes to make the smaller changes visible which take place after the strong increases in the first few seconds. Overall, the product amounts evolve as expected, with general increase from beginning to end. Nevertheless, there are some differences in the behaviour of the undoped (figure

8.10d) and doped species (figure 8.10e). While they both show a large gain in the first few seconds, the continuous increase of the undoped oligothiophenes is only reduced in its speed. The doped PT, however, reaches a maximum amount after seven seconds, which is followed by a subsequent slow and steady decay.

At the beginning of the data collection, the undoped oligothiophenes have already been formed to an amount of (0.034 ± 0.001) a.u.. Thereafter, they increase with a very fast rate to (0.412 ± 0.004) a.u. ($t = 7.0\,s$), followed up by an intermediate growth to (0.421 ± 0.004) a.u. ($t = 30.0\,s$), and in the end reach a final amount of (0.442 ± 0.004) a.u. after 200 s. At $t = 0\,s$ there is no evidence of any doped oligothiophene species in the solution. Thereafter, however, doped PT is formed at a very high rate in the first phase to (0.434 ± 0.003) a.u. at $t = 7.0\,s$. Moreover, this is also the maximum amount that is reached throughout the whole investigated time. Thereafter, the doped PT is slowly decreasing, to finally reach an amount of (0.421 ± 0.003) a.u. at the end of the process.

In the following, these observations are brought together to follow the chemical reactions taking place in the process of the investigated *in situ* polymerization under deficiency of FeTos. At the beginning of the data collection, the solution is composed in the largest fraction of the two reaction educts. There are no traces of doped polythiophene and only a small amount of uncharged oligothiophenes present. Hence, the polymerization reaction has started just immediately before $t = 0\,s$ or in the moment of the first measurement. The doping process, on the other hand, has not yet started at that point, supporting the stepwise reaction mechanism proposed in section 3.2. In the first phase of the process, both polymerization and doping take place at a very high rate. Therefore, both educts decay rapidly, while the absorbance of all polymeric species is drastically increased. This phase, however, ends after only seven seconds, when the uptake of the BT and Fe^{3+} is slowed down to an intermediate speed. This is accompanied by an abrupt interruption of the product generation as well, with the oligothiophene formation slowing down and the amount of doped PT actually decreasing. Apparently, the previously oxidized polymer chains now further polymerize to neutral molecules. Finally, the last phase of the process begins at approximately $t = 30\,s$. Here, all the rates continuously decay until the compounds reach their final amounts after about two minutes of measurement time. While the data suggests an ongoing formation of undoped oligothiophenes even at the end of the investigated 200 s, the increase from $t = 120\,s$ ((0.434 ± 0.004) a.u.) to the final value is below 2 % and therefore considered to be negligible in comparison to the increase in the prior phases.

The ratio between doped and undoped polymeric species is 0.95 at the and of the process. Again, this is not a physically significant quantity. However, it can be applied

as a measure of the relative doping level, when the influence of the FeTos concentration is discussed in section 8.5.

In summary, the time-resolved transmission measurements allow to draw an image of the reaction rates in the different phases of an *in situ* polymerization under deficiency of employed oxidizing agent FeTos. It is possible to track the evolution of the chemical compounds from deposition of reaction mixture to final film formation. In the following section, the time-resolved GIWAXS measurements are analyzed and interpreted to extend the already derived preliminary model with information on the morphology evolution during the process.

8.4.2. Evolution of morphology: crystallization of FeTos

In this section, the dynamics of the film formation dynamics during the *in situ* polymerization under deficiency of FeTos are investigated by means of time-resolved GIWAXS measurements. The two-dimensional data detected on the area detector in the course of the experiment are transformed into q-space, subsequently reduced by radial integration, and finally corrected with a local background around the most prominent FeTos peak such as described in section 8.2. Figure 8.11 displays the resulting intensity profiles over a large q-range (a) and the background-corrected peak of the crystalline FeTos (b). Other than in the transmission measurements, only the first 25 seconds of the reaction are tracked by GIWAXS.

First, the changes in the intensity profiles are going to be discussed qualitatively. The background corrected data clearly show that the FeTos peak is already present at the beginning of the data collection. Thereafter, there is a rapid increase in the intensity, that is accompanied by a shift of the peak center to lower q. At the same time, the scattering background around that peak escalates within a few measurements (i.e. a few 100 ms). This, obviously, is only visible in the cuts presented in figure 8.11a, as the background is already subtracted in 8.11b. The gain in peak intensity is happening mostly in the approximately first five seconds (blue lines). Afterwards, the increase is slowed down significantly. The final static measurement indicates an ongoing increase in crystallinity after the end of the time-resolved data collection. These observations already verify a starting of the crystallization of FeTos, probably induced by an immediate evaporation of the solvent right after deposition, prior to the data collection. Nevertheless, the largest fraction of the scattering intensity is gained within the measurement time. A more detailed analysis of the FeTos crystallization can be performed by fitting the most intense peak with a gaussian function. The fitting results are presented in figure 8.12. The peak intensity (figure 8.12a) gives rise to information on the amount of crystalline material

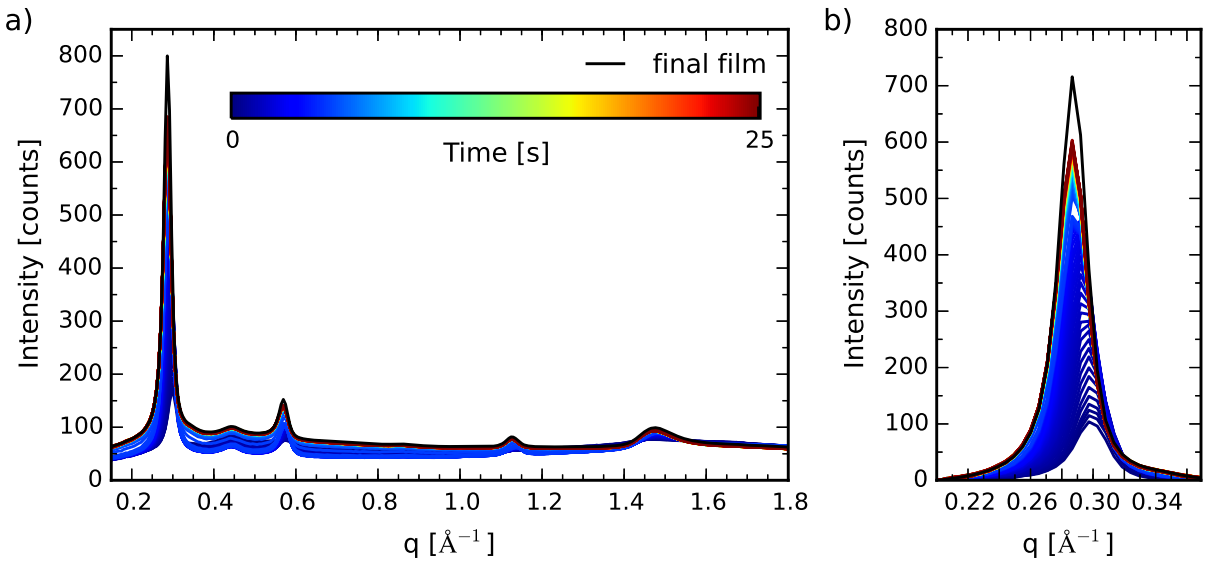

Figure 8.11.: Time-resolved GIWAXS measurements of *in situ* polymerization under FeTos deficiency. a) Radially integrated intensities of 2d data, b) FeTos peak after subtraction of local background. In both plots the time-resolved measurements are displayed in colors, while the static measurement after the film deposition is plotted in black.

in the thin film, the center in q-space is inversely proportional to the real space crystal lattice distance that corresponds to the peak, and the FWHM of the gaussian can be employed to extract the lower limit of the present average crystal size (c) by application of the Scherrer equation (equation 3.16). The fit results of the final static measurements are going to be included in the discussion of the final model in section 8.4.3.

The evolution of the parameters extracted from the fits will be discussed individually first. Afterwards, the observations will be brought together to formulate an overall interpretation of the FeTos crystallization process upon deficiency conditions. At $t = 0\,s$, the intensity of the investigated FeTos peak is (99 ± 3) counts. In the first short phase, the intensity increases strongly until it reaches an almost constant value of (430 ± 10) counts at $t = 2.5\,s$. For a period of two seconds, the intensity does not increase nor decrease, until it rises again at a decreased speed to reach an intensity of (560 ± 20) counts at the end of the investigated 25 s. Eventually, it reaches a final film peak intensity of (670 ± 20) counts.

As already observable from the background corrected cuts, the position of the peak shifts to lower q-values in the course of the reaction. In the beginning, the peak appears at $(0.298 \pm 0.001)\,Å^{-1}$, which corresponds to a lattice distance of $(21.06 \pm 0.03)\,Å$. With time, the q-value of the peak center decreases, until it stays at its final position of $(0.286 \pm 0.001)\,Å^{-1}(21.95 \pm 0.003\,Å)$. Within the error bars, there is no further shift

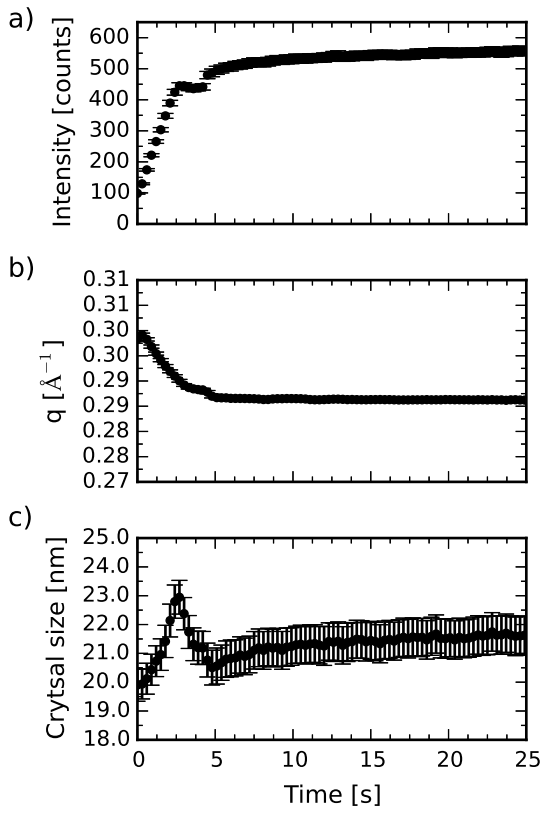

Figure 8.12: Evolution of the parameters extracted from the Gaussian fits of the FeTos peak: a) peak intensity as a measure of the amount of crystalline material in the film; b) peak position, which is inversely proportional to the real space distance between the iron ions in the FeTos crystals; c) crystal size calculated from the FWHM by the Scherrer equation. Error bars correspond to time resolution in horizontal and fitting inaccuracies in vertical direction, respectively.

occurring after the end of the time-resolved measurement, as determined by the static measurement. Hence, the crystal lattice distance under investigation here increases by 0.9 Å in the course of the measurement.

The average crystal size of the FeTos crystals shows a very interesting behavior. In the beginning of the data collection it is calculated to be (19.9 ± 0.6) nm from the peak FWHM. Similar to the peak intensity, the crystal size features a very rapid increase in the first 2.5 s to reach a maximum value of (22.9 ± 0.6) nm. However, this increase is followed by an equally steep decrease until t = 4.5 s, when the size is reduced to (20.8 ± 0.6) nm. Thereafter, the size does not significantly increase again within the investigated time frame. In the final film, the average FeTos crystal size is (23.6 ± 0.8) nm.

The crystallization dynamics of the FeTos crystals enable to track the transformation from solution to solid film by comparing the crystal growth rates in the different phases of the process. It is assumed that FeTos is fully dissolved in the reaction mixture before deposition. Hence, the crystallization only starts upon evaporation of the solvent, when the concentration is increased beyond the solubility limit. The evolution of the peak intensity suggests that the crystallization process starts just before the beginning of the data collection, as it is still small compared to the final value and increasing at a rapid speed. In addition to that, the crystal size is still growing quickly. Therefore, the reaction

mixture is supposed to still be liquid with the solvent evaporation inducing the rapid crystallization. After a short time, however, the crystallinity reaches a constant value and the average crystal size actually decreases again. This reduction of the average size is interpreted to rather be a partial dissolution of the already existing crystals as compared to the formation of new, smaller crystallites, because the overall degree of crystallinity is not increased. In the third phase of the process, the amount of crystallinity is again increasing, but at a significantly reduced rate, until it reaches its final value.

In summary, the GIWAXS measurements give an insight on the transformation from solution to solid film, as observed by the crystallization of FeTos. Nevertheless, these observations have to be put in context with the process of the chemical reactions to gain an understanding of the process of the *in situ* polymyerization under deficiency of oxidizing agent. This will be done in the following section.

8.4.3. Reaction and film formation dynamics

The two previous sections presented the results of the time-resolved transmission and GIWAXS measurements, respectively. Now, these observations are combined to formulate a model of the film formation process during the *in situ* polymerization of polythiophene under deficiency of oxidizing agent FeTos. Analogously to the proceedings in section 8.3.3 for the reaction under excess conditions, several of the obtained parameters are normalized and put together, to follow the evolution of the chemical reactions as well as the solidification of the film. The normalized data are displayed in figure 8.13. Again, each parameter is plotted in two separate graphs to account for the rapid processes taking place in the first few seconds as well as the slower final film formation. The results of the static GIWAXS measurement performed on the final film are appended to the plots at t = 170 s when the film formation is assumed to be completed.

The polymerization and doping reaction are tracked by analyzing the evolution of the amounts of the educts BT and Fe^{3+}(figures 8.13a and b), each normalized to its respective initial value, and the amount of doped PT (figures 8.13c and d), normalized to its final value. The crystallization of FeTos is taken into account by means of interpreting the scattering peak intensity (figures 8.13e and f) and the average crystal size (figures 8.13g and h), both normalized to their respective final value. The process is divided into four different stages I_d - IV_d (d: FeTos *deficiency* conditions). These will be explained in further detail in the following by discussing the evolution of the parameters with time.

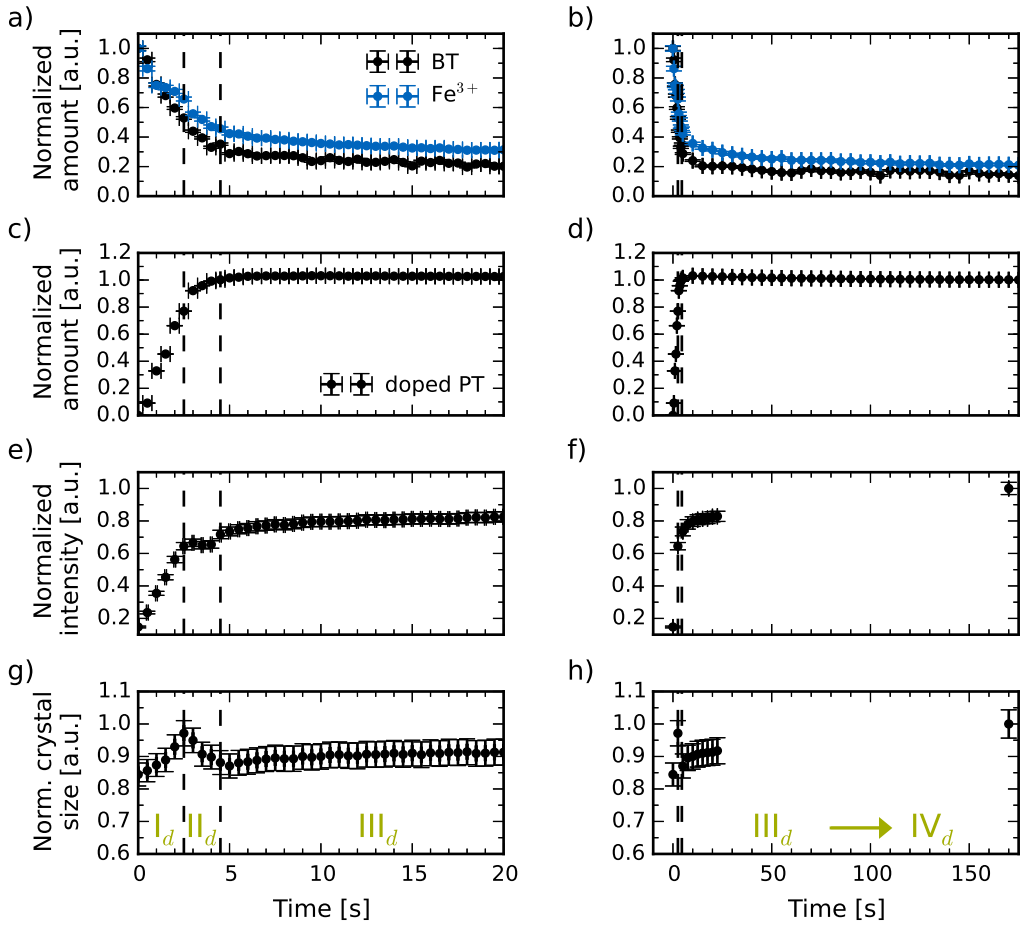

Figure 8.13.: Evolution of the normalized paramaters of the *in situ* polymerization under FeTos deficiency, extracted from the respective fits of the time-resolved absorbance and GIWAXS data. Each paramameter is plotted with high time resolution for the first 20 seconds (left) and lower time resolution for 175 seconds (right). a,b) Amounts of educts bithiophene (black) and Fe^{3+}(blue) from absorbance, c,d) amount of doped polythiophene from absorbance, e,f) scattering intensity of FeTos peak from GIWAXS, g,h) crystal size of FeTos crystals from GIWAXS. The process is divided into four different stages, that are separated by dashed vertical lines and labelled accordingly. Error bars correspond to time resolution in horizontal and fitting inaccuracies in vertical direction, respectively.

$\mathbf{I}_d$: *Fast polymerization leading to depletion of Fe^{3+} ions in solution*

In the beginning of the data collection, the educts decay at a very high rate. Moreover, there is no evidence of doped PT at t = 0 s. Hence, it is assumed that the polymerization and doping reaction start around the time of the first measurement. The initial value of the intensity of the FeTos crystal peak also suggests a beginning of the crystallization directly prior to the data collection. Therefore, while solvent evaporation is assumed

to take place already before the start of the time-resolved measurements, the chemical reactions and salt crystallization are proposed to start around t = 0 s. During the first 2.5 s, the rates of the involved processes are very high.

However, the deficiency of employed FeTos results in a competition between the chemical uptake of the Fe^{3+} ions in the polymerization/doping processes and the crystallization. At some point, the solution depletes, which results in two things: (i) a drop in the polymerization rate, and (ii) a stop in the FeTos crystal growth. Therefore, the first phase of rapid polymerization ends at t = 2.5 s.

II_d: *Partial dissolution of FeTos crystals and decreased reaction rates*

In the second phase, the effects of the Fe^{3+} depletion in the remaining solution become visible in the different parameters. While the rate of the educt uptake and PT formation are slowed down, the average FeTos crystal size decreases again. The ongoing evaporation of the solvent is assumed to have an additional impact on the reaction rates. However, the reduced reaction rates cannot be explained solely by a reduced mobility due to the solidification of the thin films, since this would not result in a decreasing FeTos crystal size. Apparently, this phase ends when the decrease in crystal size is stopped and the reaction rates decay even further.

III_d: *Slow polymerization and doping*

In the following, the crystallization of FeTos happens at continuously decaying speed. Within the error bars, there is no further in- or decrease in crystal size in this phase. Similarly, the intensity gain of the FeTos peak is decreased strongly. This is accompanied by a sudden drop of the polymerization rate, as seen by the decrease in the educt amounts and the almost unchanged amount of doped PT chains. These observations suggest the solidification of the film resulting in the end of the chemical conversions, although there are still educt molecules available in the system. The residual solvent molecules as well as the liquid monomer might provide the minor molecular mobility that is required for the very slow ongoing processes.

IV_d: *Final film formation*

In this experiment, there is no clear separation between the third phase of drastically reduced polymerization rates and the final film. The reaction rates constantly decay, until the final film properties are achieved. As the GIWAXS data indicate, the FeTos crystallization is not fully complete after the 25 s of time-resolved measurements. Most likely, the crystallization continues at a constantly decaying rate, until the final crystallinity and crystal size are reached

In summary, the combination of the time-resolved GIWAXS and transmission measurements reveal the dynamics of an *in situ* polymerization of polythiophene under deficiency of oxidizing agent FeTos. A four-stage model is proposed, that divides the process into phases of rapid polymerization in solution, followed by a depletion of the Fe^{3+} ions within the solution. Nevertheless, the polymerization continues upon partial dissolution of the already formed FeTos crystallites, until most of the solvent is evaporated and the film is formed.

8.5. Process of *in situ* polymerization

Finally, the results discussed in the previous sections are combined to gain an overall understanding of the processes involved in the *in situ* polymerization of PT thin films. For this purpose, the four respective phases proposed for the film formation under FeTos excess as well as deficiency are combined in one scheme in figure 8.14. The chosen representation illustrates the evolution of several of the obtained parameters with progression of the process. Since the phases of the two experiments differ in length, the progress axis is not equivalent to time but simply depicts the succession of the processes. The progress of the polymerization reaction is tracked as sum of doped and undoped PT, respectively, with the ratio between the two species visualized as the background color in different shades of blue. The uptake of the monomer BT can be followed by the decreasing number of green dots. The displayed FeTos crystals (orange) represent the evolution of crystal size as well as crystalline material.

In the following, the two investigated processes are compared phase by phase to determine general processes in the *in situ* polymerization as well as steps that are specific for the different monomer to oxidant ratios.

In the beginning of the experiment, the metastable reaction mixture is deposited to the preheated substrate. In both cases, the solution is assumed to be free of FeTos crystals and stable against early polymerization reactions. Hence, it only contains dissolved monomer molecules and the FeTos ions. At $t = 0\,s$ (figure 8.14, top row), however, the solutions have already undergone some changes from their initial states. In both cases, a fraction of the solvent has probably already evaporated because the presence of FeTos crystals indicate a concentration beyond its solubility. Naturally, the amount of crystalline FeTos is higher in the excess case, as the initial concentration is already higher here as well. A higher concentration of Fe^{3+} ions also results in an earlier onset of the oxidative polymerization. As the redox reaction on hand is controlled by the oxidation potentials of the two reactants, an increased Fe^{3+} concentration also increases the reaction probability according to Nernst equation (equation 3.5). Hence, there is already a high amount of doped and undoped

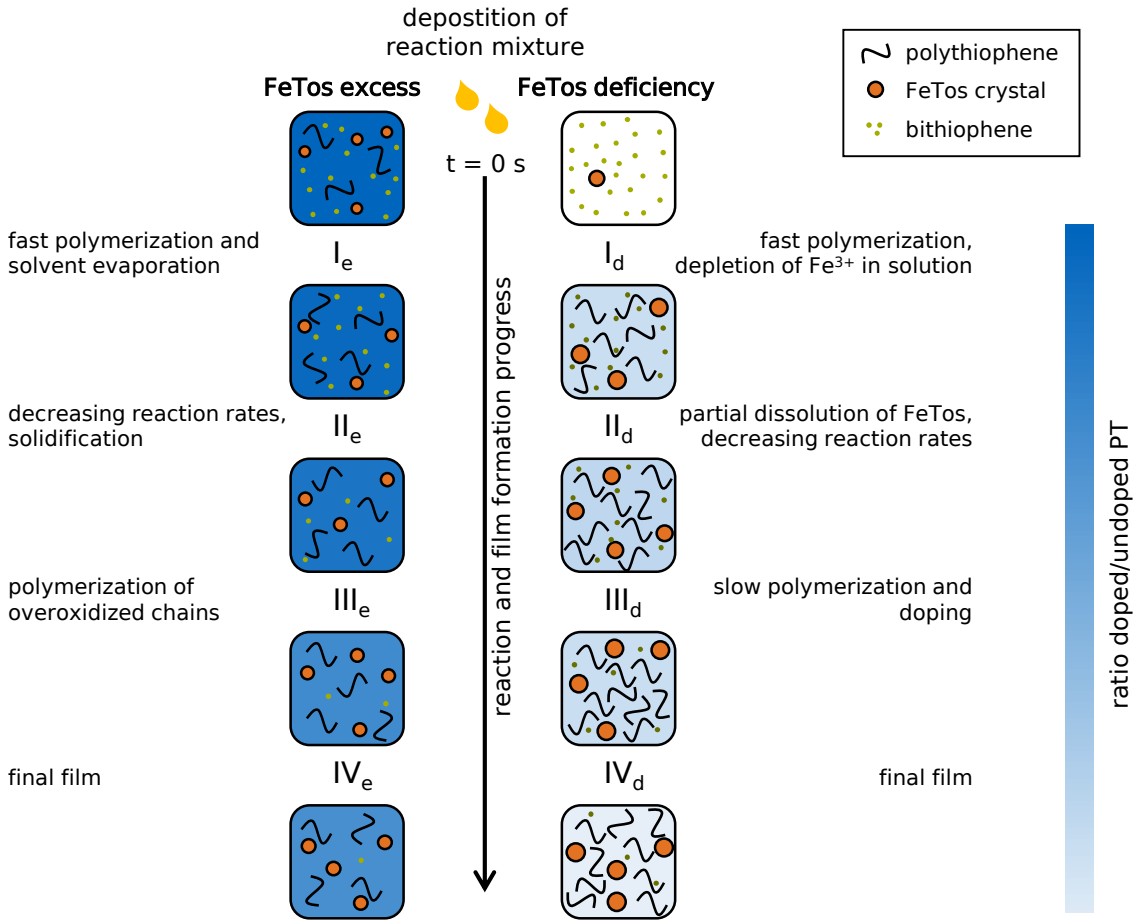

Figure 8.14.: Schematic illustration of the *in situ* polymerization and film formation processes under FeTos excess (left) and deficiency (right). The transformation from solution to polymer film is represented by means of the states at the end of the respective phases. The ratios between the different components, however, is not representative. The amount of polythiophene is obtained by summing up the amounts of neutral oligothiophenes and doped PT. The ratio between doped and undoped species is depicted in the color of the background. The vertical process coordinate is not proportional to time, but depicts the progression of the different phases for the two investigated systems.

PT present if an excess of FeTos is employed, while the chemical reactions have not significantly started under FeTos deficiency.

In the first phase the rates of the chemical reactions are high and FeTos crystallizes rapidly. Therefore it is assumed that the films are still liquid but that the solvent is quickly evaporating. The degree of oxidation of the formed polymeric species strongly depends on the employed monomer to oxidant ratio. With more Fe^{3+} in the solution, more thiophene units are in their oxidized state. Under deficiency conditions the amount

of iron ions available in the solution is not enough to provide an additional oxidation of the polymer chains already present in the films.

The reaction kinetics of the first phases have a strong impact on the following behavior of the systems. The high doping level of the excess sample results in a high fraction of "activated" cationic polymers in the film. If two of these are spatially close to each other they can form a polymeric carbon-carbon bond even after the mobility in the system is already reduced upon evaporation of the solvent. Hence, the doping level reaches a maximum after the second phase and subsequently decreases again. In the deficiency case, on the other hand, the fast polymerization results in a depletion of dissolved Fe^{3+} ions in the mixture. As a result, parts of the already formed FeTos crystals dissolve again to ensure a continuation of the polymerization reaction.

After a solidification of both films in the respective third phases, the reaction rates are decreased to a minimum for both cases. In the end, the differing final doping levels are consistent with the expectations for the different ratios between monomer and oxidizing agent. As already indicated by the conductivity measurements in chapter 7 the doping level is tunable with the employed ratio of BT to FeTos in the reaction mixture.

Overall, the kinetics of the polymerization and doping reaction are dominated by two main factors. In the beginning, the start of the reaction is controlled by the redox potentials of the components that are strongly concentration dependent. Thus, the processes start earlier upon excess of Fe^{3+} ions. Thereafter, the availability of the components in the drying mixture dictates the kinetics as well as the film formation process. The FeTos excess results in a strong overoxidation of the polymer chains leading to an ongoing significant polymerization even after evaporation of the solvent. Under deficiency, the iron ions rapidly deplete in the solution, resulting in a partial dissolution of the FeTos crystals to keep the polymerization going. The doping rate, on the other hand, is reduced strongly here. Other than introduced in section 3.2 the oxidative *in situ* polymerization is not a two-step reaction with clearly distinguishable subsequent processes of polymerization and doping. The nature of the chemical oxidation resulting in finally doped PT chains is the same as that of the oxidation which activates the chains for polymerization. Hence, chain growth and doping happen simultaneously throughout the whole process. This is clearly visible in the ratio between doped and undoped PT which in both experiments is already set in the early stages of the film formation. Hence, the doping level is probably not significantly adjustable by prolonging or shortening of a certain phase in the process, as the fraction of oxidized chains is simply determined by the amount of available oxidant ions in the system.

8.6. Summary

This chapter presents a novel approach of simultaneously tracking reaction kinetics and film formation dynamics of a solution-based oxidative *in situ* polymerization of polythiophene thin films. Time-resolved GIWAXS and UV/Vis transmission measurements are combined to investigate the evolution of the polymer film that is fabricated by deposition of the metastable reaction mixture by slot-die coating.

The reaction rates can successfully be tracked by fitting the absorbance spectra with a combination of the specific educt and product absorbances, respectively. The GIWAXS data complement these findings by means of detecting the FeTos crystallization. While this allows to indirectly follow the solidification of the films it is not possible to gain an insight on the polymer aggregation, as there are not PT signals observable in the scattering pattern. Presumably, this is only an artifact of the here shown measurements and not a drawback of the experimental approach itself, as PT is generally known to crystallize and give rise to distinct scattering peaks as shown in the previous chapter.

The impact of the employed monomer to oxidizing agent ratio on the reaction process is investigated by performing two polymerization reactions, one under FeTos excess and one under FeTos deficiency, respectively. A four-step model of the reaction and film formation is proposed for both processes, whereby the dynamics of each are strongly dominated by the amount of Fe^{3+} ions in the reaction mixture. In the early stages, the iron to BT ratio mainly dominates the onset and kinetics of the polymerization, as the initiating redox reaction is controlled by the concentrations of the species. Moreover, the probability of a subsequent doping of the formed chains increases with more Fe^{3+} in the solution, resulting in a higher doping level under the excess conditions. Later on in the process, the different amounts of iron ions result in (i) an ongoing polymerization of previously oxidized chains even after solidification of the film, or (ii) an early depletion of the solution leading to a drop in the reaction rates and a partial dissolution of the already present FeTos crystals in the film. The level of doping of the chains is only dictated by the BT:FeTos ratio from the very beginning of the chemical reactions and differs strongly between excess and deficiency conditions also in the final films.

9. Impact of water on film morphology

In most organic electronic devices the interplay between different functional materials is of utmost importance. For an optimization of device performance, properties such as wettability and adhesion between stacked layers, their electronic structure and interaction, and the interface morphology need to be understood and controlled in the material choice and fabrication. [121] A famous example for the impact of interface area and energy level matching is the active layer of organic solar cells, especially in the bulk heterojunction (BHJ) morphology (introduced in section 3.1). A randomly interdigitated network of electron donor and electron acceptor material is employed to maximize both, the charge carrier generation upon light absorption and their separation at the donor-acceptor interface. This morphology is achieved by processing the active layer from a solution containing both materials. [47, 50]

When polythiophene (PT) thin films are synthesized *in situ* as presented here, the possibilities to blend the polymer with a second material are very limited. This is mostly due to the fact that the polymerization reaction is very sensitive to the addition of other chemicals to the reaction mixture. Hence, *in situ* polymerization techniques typically give insoluble films of polythiophene only. The solar cells presented in chapter 6 are therefore prepared in a bilayer geometry with the electron acceptor material PCBM deposited on top of the PT layer. As a consequence, the interfacial area between the two materials is strongly reduced in comparison to BHJ solar cells. So far, BHJ solar cells of native polythiophene have only been prepared by processing a blend of a soluble substituted PT derivate and PCBM, followed by a high-temperature post-treatment resulting in the thermal cleavage of the solubilizing side chains. [26]

In general, several other routes are established that enable the tuning of nanomorphology and interface in functional layer stacks. A common approach in organic solar cell research is the fabrication of a nanostructured layer followed by a backfilling with the second material. This way it is possible to obtain an interdigitated morphology despite the subsequent deposition of the two respective layers. Nanoimprint lithography (NIL) is often employed for the structuring of polymer layers for application in organic solar cells. [122–124] NIL uses fine-structured molds whose pattern are transfered to the polymer films by imprinting under pressure and typically produces vertical and ordered struc-

tures in the films. While physical structuring methods such as NIL are usually employed in post-treatment routines after the film fabrication, it is possible to directly fabricate porous polymers by means of synthetic chemistry. Porosity in polymers can be created by exploiting self-assembling processes taking place for example in block copolymers, or via dissolution of embedded templates (e.g. nanoparticles) from inside the polymer matrix. [125] Porous polymers are a material class that is strongly investigated in research fields such as catalysis and gas storage. [126,127] Gu et al. have developed an electropolymerization method for porous films of certain fused thiophene derivatives that form helical structures upon polymerization. [128] They were able to backfill the pores of these polymer helices with C_{60} as electron donor giving rise to solar cell devices with power conversion efficiencies of up to 5 %.

Previously, it has been observed that the presence of humidity influences the film formation during oxidative polymerization reactions with iron(III) p-toluenesulfonate (FeTos) as oxidizing agent. As a result, thin films of varied, for example porous, morphology are synthesized. [129–131] Therefore, this chapter explores the possibilities of adapting the established *in situ* polymerization technique for fabrication of semiconducting PT films with tunable porosity. For this purpose, water is employed as solvent additive in the reaction mixture in varied volume fractions between 0 % and 25 %. The morphology of the final PT films is investigated by means of scanning electron microscopy (SEM) and grazing-incidence small-angle X-ray scattering (GISAXS) in section 9.1. The origin of the water impact is investigated by a combined structural analysis of the as-prepared films prior to any post-treatment with GISAXS and grazing-incidence wide-angle X-ray scattering (GIWAXS) in section 9.2. Finally, the obtained results are discussed (section 9.3) and summarized (section 9.4).

9.1. Morphology of pure polymer films

Initially, the morphology of the semiconducting polythiophene thin films is investigated to verify whether the added water has an impact on the resulting film porosity. This is done by combining SEM to examine the surface structure and GISAXS for studying the inner film morphology.

Surface morphology

First, the surface morphology is discussed in terms of the recorded SEM images given in figure 9.1. The images are displayed with water content increasing from 0 % in figure 9.1a to 25 % in figure 9.1f. At first sight the polymer surfaces of the six films appear to be of very different nature. However, there are a few characteristics that are visible in

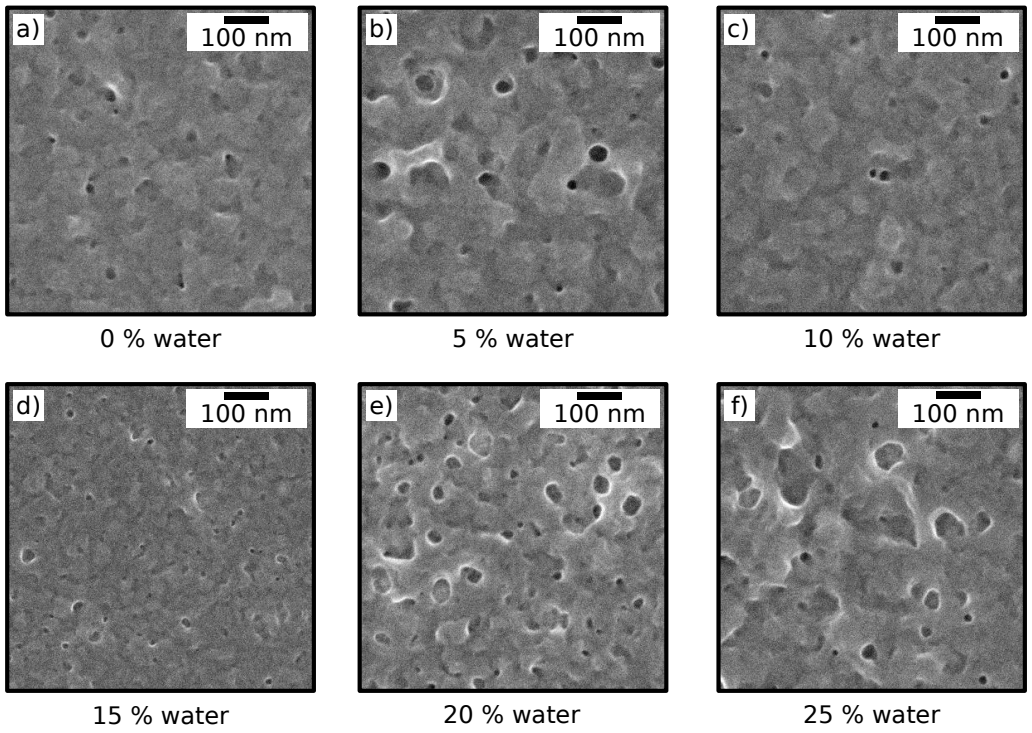

Figure 9.1.: Surface morphology SEM images of polythiophene thin films synthesized *in situ* with different volume fractions of water in the reaction mixture.

all the images and should be stressed here. First of all, the replacement of a significant fraction of propanol by water does not seem to inhibit a successful *in situ* synthesis of PT. Moreover, no signs of quality losses due to dewetting or demixing of the different solvents are observed. However, the films are of varying roughness, with structures of different dimensions visible in the images. Since the contrast in SEM images derives from differences in conductivity, and the films are composed of polythiophene only after the rinsing, the dark structures in the images are assumed to be pores or dents. Overall, three classes of these pore-like inhomogeneities are present whose amounts are different for every film. They can roughly be categorized into small (5-10 nm), intermediate (10-20 nm) and large pores (30-40 nm). Nevertheless, from the SEM images alone it is not possible to resolve their elongation in vertical direction. The surface morphology of each of the investigated films is described in more detail in the following.

The PT film synthesized without addition of water (figure 9.1a) makes a smooth impression, with pores mostly of the intermediate size regime. Upon addition of 5 % of water (figure 9.1b), the surface structure is dominated by large pores, with the number of intermediate pores decreasing compared to the previous film. The overall amount of pores, however, appears to stay of the same order. The PT film obtained with 10 % wa-

ter in the reaction mixture (figure 9.1c) again has a very similar appearance as the one obtained without water, with only intermediate sized pores and a decreased roughness as compared to the 5 % film. Increasing the water content further to 15 % leads to the formation of a PT film with pores almost exclusively in the small size regime, which are not observed for lower water fractions (figure 9.1d). The film corresponding to the 20 % sample (figure 9.1e) has by far the most inhomogeneous appearance with a large number of pores of all size regimes from 5 to beyond 40 nm. Here, the SEM image indicates an almost foam-like surface morphology. Finally, the highest employed water fraction leads to an again decreased number of surface pores (figure 9.1f).

Overall, the evolution of the surface morphology as investigated by SEM does not show a clear dependence on employed water content. So far, it is not possible to resolve whether it has an impact on the final film morphology, since the surface structure appears to be changing randomly. However, SEM can only provide an insight to a very limited small surface area, without giving information on the state of the film volume. Hence, it is necessary to employ a complementary method to gain a more complete picture of the film morphology.

Inner film morphology

GISAXS measurements are performed for researching the morphology inside PT thin films. The collected 2D scattering data for all samples are presented in figure 9.2.

The diffuse scattering pattern of the differently prepared polythiophene thin films have an overall similar appearance, with no pronounced features from highly ordered structures. Moreover, all samples feature a strongly increased horizontal scattering at the Yoneda peak. Although a vertical beam stop shields the scattering at very low q_y, an intensity change can still be observed close to the resolution limit there. Upon increasing water content in the synthesis the intensity of the diffuse scattering at low q_y shows a general

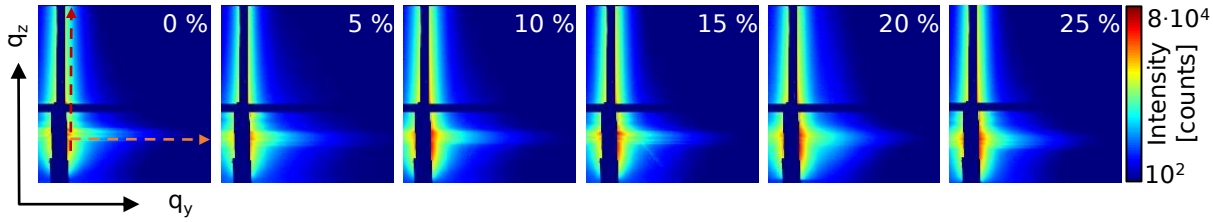

Figure 9.2.: Two dimensional GISAXS pattern of semiconducting polythiophene thin films synthesized *in situ* with different volume fractions of water in the reaction mixture; red and orange arrow in 0 % image represent prosition of vertical and horizontal line cut, respectively. The low-q_y region including direct and specular beam is shielded with a vertical beam stop.

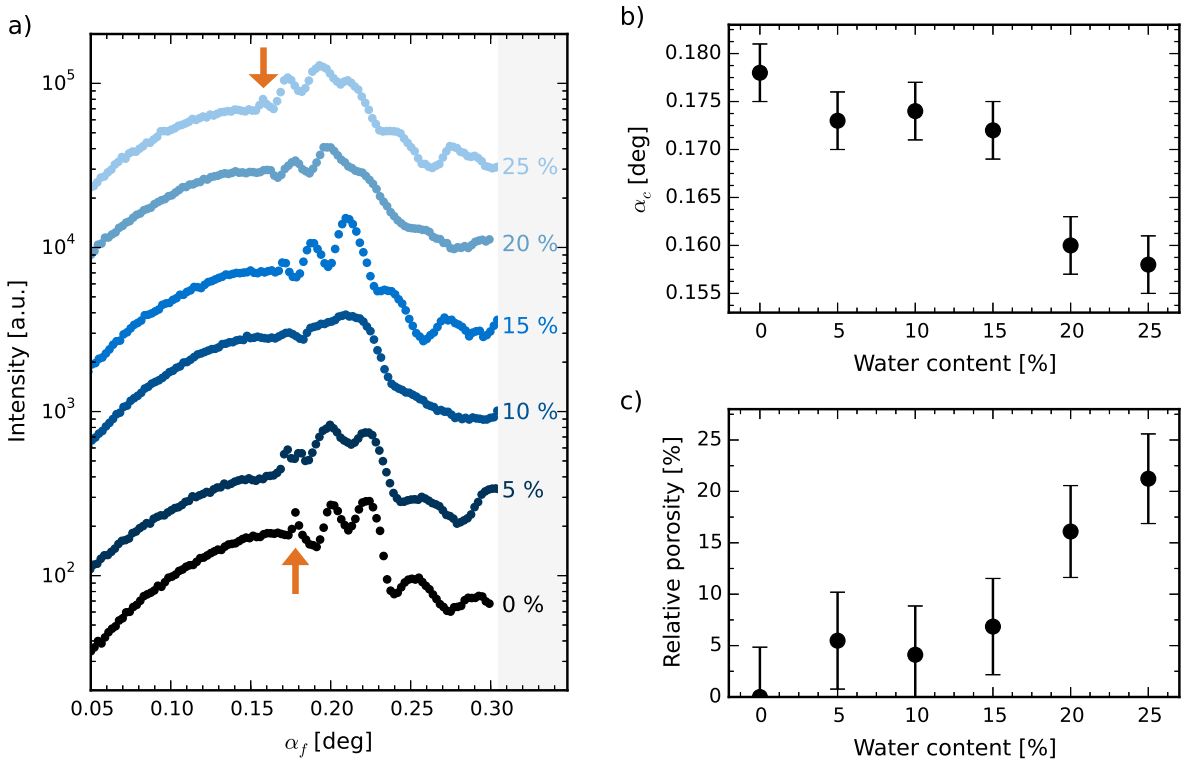

Figure 9.3.: Analysis of vertical line cuts of GISAXS measurements on semiconducting PT thin films synthesized with different volume fractions of water in the reaction mixture. a) Vertical line cuts, shifted with respect to each other for clearer presentation, orange arrow indicates Yoneda peak; b) critical angle obtained from position of Yoneda peak plotted against employed water fraction; c) Porosity of thin films realitve to density of film obtained without addition of water. Error bars correspond to resolution of GISAXS data.

increase. For a more detailed analysis of the film morphologies, vertical and horizontal line cuts are taken by integrating the intensity in the respective directions in slices with widths of three pixels each at the positions indicated by the arrows in figure 9.2.

The information gained from the vertical line cuts is discussed first. The vertical cuts of all samples as well as the respective parameters gained from the Yoneda peak position (critical angle and porosity) are displayed in figure 9.3.

In figure 9.3a the vertical intensity at constant q_y is plotted against the exit angle α_f for each of the PT films. The data are shifted along the y-axis for a clearer representation. The most important feature to be highlighted here is the Yoneda peak, a material specific peak of high intensity where the exit angle α_f matches exactly the critical angle α_c of the material. [61] The Yoneda peak positions in the displayed cuts are marked with two orange arrows for the films prepared without and with highest fraction of water. A qualitative analysis already shows that the peak is shifting towards smaller exit angles with

increasing amounts of water in the synthesis. The resulting critical angles obtained from the maxima of each peak are plotted in figure 9.3b. According to the presented GISAXS measurements, the α_c of the polythiophene films steadily decrease from $0.178° \pm 0.003°$ (0 % water) to $0.158° \pm 0.003°$ (25 % water). As the critical angle depends on the scattering length density (SLD) of the material, it is possible to extract the mass density of the different polythiophene films from the critical angles. In general, a decreasing α_c is an indication of a decrease in density. As the films are composed purely of polythiophene, the decrease in density must derive from embedded air within the film. Hence, the films show an increasing porosity with increasing amount of water added to the reaction mixture. As introduced before, equation 3.18 can be used to calculate the porosity as the ratio between the density of the respective film to the mass density of the densely packed, non-porous material. However, the density of dense PT is not known, as it depends strongly on the employed synthetic method. Therefore, the relative porosity in relation to the film fabricated without addition of water is calculated for each sample. The mass density at zero water is calculated to be $1.46\,\mathrm{g{\cdot}cm^{-3}}$, which is in the range of experimental and theoretical values for PT found in literature ($1.35\,\mathrm{g{\cdot}cm^{-3}}$ [107], $1.4\,\mathrm{g{\cdot}cm^{-3}}$ [98], $1.55\,\mathrm{g{\cdot}cm^{-3}}$ [106]). The resulting relative porosities are shown in figure 9.3c. According to the performed analysis, the porosity can be increased by (21 ± 5) % upon addition of the maximum amount of 25 % of water to the reaction mixture.

In summary, the vertical cuts give rise to an impact of the added water on the porosity of the *in situ* polymerized polythiophene thin films. However, for an information on the sizes of the pores and their lateral distribution within the films it is necessary to additionally analyze the horizontal line cuts. These are obtained by integrating the intensity at the Yoneda position of each of the respective samples and therefore at increasing q_z position for higher fractions of water.

The horizontal line cuts presented in figure 9.4a are modeled with three form and respective structure factors. The smallest object class is kept constant as background. The structure factor of the largest objects is set to 300 nm for all datasets and therefore lies outside the resolution limit due to shielding by the beam stop at low $q_y$and is therefore not discussed. The structure radii (form factor) and distances (structure factor) plotted in figures 9.4b and 9.4c are extracted directly from the model. With increasing water content, the large structures steadily grow with radii increasing from (44 ± 1) nm for PT synthesized with 0 % up to (65 ± 2) nm at 25 %, and therefore by almost 50 %. The size of the intermediate structures, on the other hand, does not show an equally clear dependence on the employed water content. When going from 0 % to 10 % the radius is increased from (14 ± 1) nm to (19 ± 1) nm. Beyond that water content, however, the structure size decreases to (15 ± 1) nm at 20%, and finally grows again to (19 ± 1) nm at

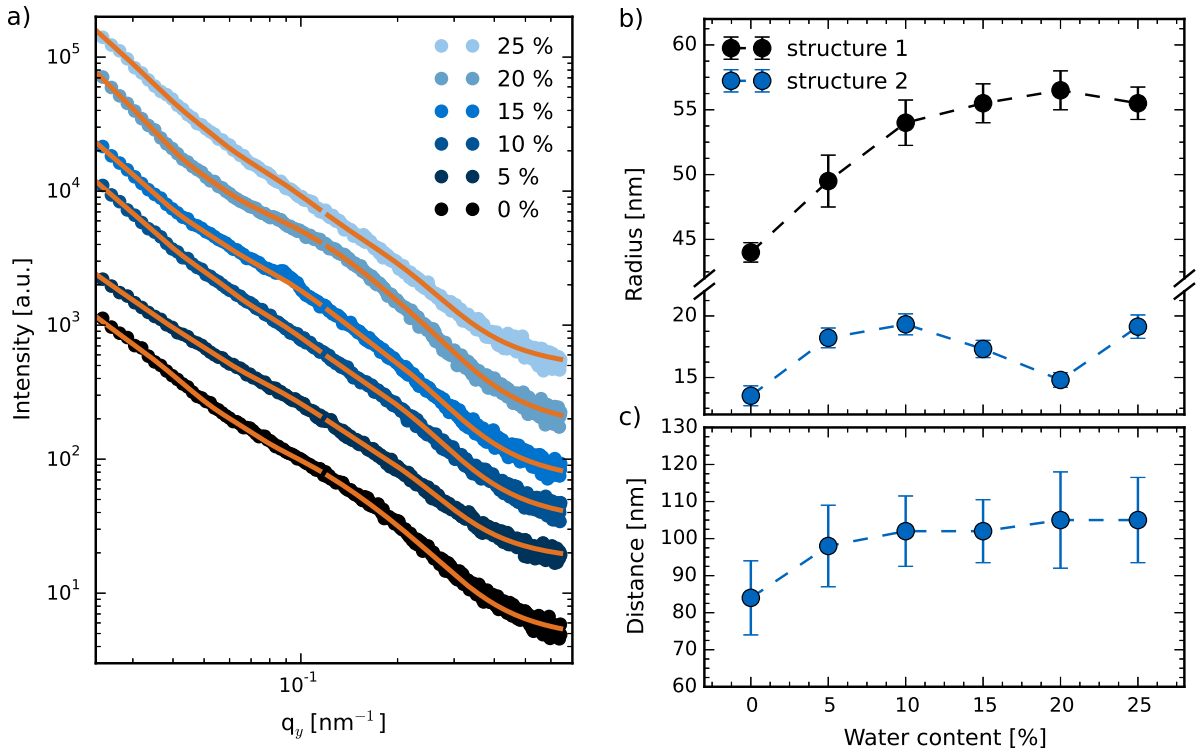

Figure 9.4.: Analysis of horizontal line cuts of GISAXS measurements on semiconducting PT thin films synthesized with different volume fractions of water in the reaction mixture. a) Horizontal line cuts, shifted with respect to each other for clearer presentation, orange lines represent the modeled data for each of the scattering curves; b,c) parameters applied for modeling the cuts: structure radii (b) and distances (c). Error bars correspond to uncertainties of the modeling, dashed lines are guides to the eye.

25%. The domain distance extracted from the structure factor is almost constantly on the order of (100 ± 10) nm for all samples that have been prepared with addition of water. Without water, the distance is only (84 ± 10) nm. Within the error bars, however, the difference to the other values is not significant.

Overall, the GISAXS data of *in situ* polymerized polythiophene thin films can be summarized in the following:

- a shift of the Yoneda peak and the corresponding decrease in the critical angle of the polymer thin films strongly suggests an **increasing porosity** upon addition of water to the reaction mixture
- the analysis of the horizontal cuts shows the presence of two differently sized structures that are changing with employed water content, with the **large domains growing** by 50 % when comparing the films obtained from dry synthesis to the one with highest water content

These two observations strongly indicate that the large domains are actually the pores within the film. However, this cannot be resolved definitely, since their interdomain distance and hence their density in the thin films cannot be determined. Due to the fact that the films contain only PT, the intermediate structures are interpreted as PT domains of higher density arising during the polymerization.

In order to determine the mechanism that induces the observed change in morphology, the PT films are additionally analyzed directly after the preparation and before all the soluble products and educt residuals are rinsed out. The properties of these unrinsed films are the center of the next section.

9.2. Crystallization of reaction components

As discussed in the previous section, the porosity of *in situ* polymerized PT thin films increases upon addition of water to the reaction mixture. Moreover, it is assumed that the porosity derives from an increase in the present pore sizes. In this section, the underlying mechanism of this change in morphology is analyzed by structural investigations on PT films directly after the fabrication and therefore before rinsing out the byproducts of the polymerization reaction.

Film morphology

Initially, the morphology of the respective films is investigated by means of GISAXS measurements. The collected 2D scattering pattern are depicted in figure 9.5. The GISAXS pattern obtained for all six samples exhibit a very broad diffuse scattering, which is especially enhanced in comparison to that for the rinsed PT films (figure 9.2). In some of the pattern, two rod-like vertical features appear at rather low q_y. These seem to be most pronounced in the sample synthesized without addition of water. Furthermore, there is more than one Yoneda region visible. A more detailed analysis of the data is performed by taking vertical and horizontal line cuts. Again, these are obtained by integrating the intensities in the respective directions in slices with widths of three pixels each. The positions of the cuts are indicated by the arrows in figure 9.5.

The vertical cuts are discussed first. Figure 9.6 gives the intensity profiles obtained at constant q_y plotted against exit angle α_f. As already mentioned for the two-dimensional scattering pattern, all cuts show two regions of enhanced intensity. These are interpreted to be the Yoneda peaks belonging to two materials of different electron density. The peaks appear at exit angles of approximately 0.16° (marked as Y1 in the figure) and 0.22° (Y2), respectively. Other than in the vertical cuts of the rinsed PT films (figure 9.3),

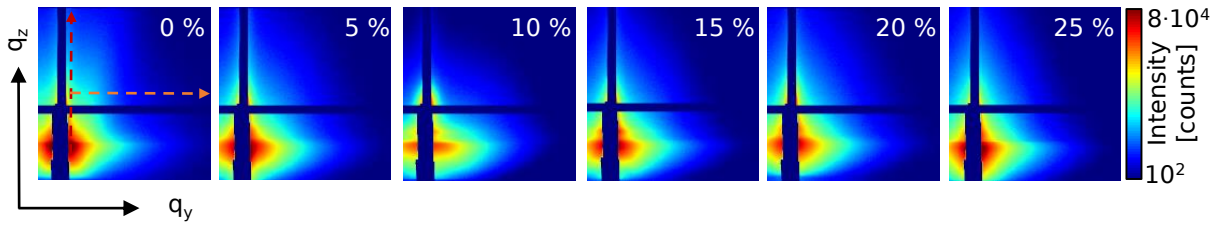

Figure 9.5.: Two dimensional GISAXS pattern of unrinsed polythiophene thin films after *in situ* polymerization with different volume fractions of water in the reaction mixture; red and orange arrow in 0 % image represent prosition of vertical and horizontal line cut, respectively. The low-q_y region including direct and specular beam is shielded with a vertical beam stop.

the scattered intensity in the Yoneda region is very broad and featureless, which makes a more precise determination of the critical angles difficult.

In order to assign the peaks to a type of material, it is useful to consider all the materials that are potentially present in the unrinsed films. These are polythiophene, Fe^{3+} and Fe^{3+} cations, tosylate anions, and even-numbered oligothiophenes of short degree of polymerization. It is possible to estimate the critical angles of all organic compounds in the system. Table 9.1 shows the chemical formulas, mass densities, and corresponding

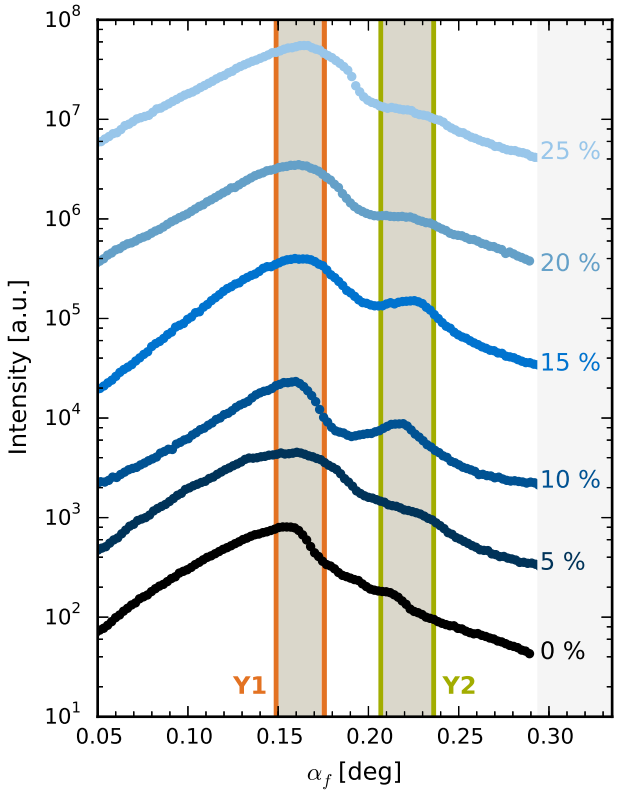

Figure 9.6: Vertical line cuts of GISAXS measurements on unrinsed PT thin films. Cuts of films synthesized with different volume fractions of water in the reaction mixture, shifted with respect to each other for clearer presentation; Y1 (orange marked region) and Y2 (green marked region) indicate presence of two different Yoneda peaks.

critical angles at the respective energy of the 2-, 4-, 6-, and 8-mers of thiophene as well as polythiophene. The critical angles are determined by means of equations 3.9 and 3.11, which link the critical angle to a material's dispersion and hence electron density. The values for polythiophene are derived from the GISAXS measurements on pure PT films presented and discussed in section 9.1.

The critical angles of the organic materials that are possibly present in the unrinsed films range from 0.171° to 0.179°. Hence, they are by far closer to Yoneda Y1 in the vertical cuts than to Y2. The densities of Fe(II)Tos and Fe(III)Tos, however, are not reported in literature. Therefore it is not possible to calculate the respective critical angles. But since iron has a much higher electron density than all organic materials, it is reasonable to assume that the iron tosylates or at least the iron ions are incorporated inside the material that exhibits the critical angle matching Y2.

The lateral distribution of the different materials is investigated by taking horizontal line cuts. As indicated in the 2D pattern (figure 9.5), these are taken at a q_z position beyond the two Yoneda peaks. This is done because the shoulder arising from the vertical intensity rods mentioned before is most pronounced here. Figure 9.7 depicts the horizontal line cuts (a) and the form and structure factors derived from the modeling (b).

From their general shape, the horizontal cuts can roughly be divided into two subgroups. They all feature a shoulder that is very well pronounced in the samples from 0 % to 10 % and becomes more broad and unresolved in the cuts with higher water content (15 %-25 %). Moreover, the shoulder shifts towards larger q_y in the beginning, while it remains at a lower, yet almost constant, q-position in the second group. In order to quantify the structural changes, the data are modeled with three cylindrical form and structure factors. The structure radii (form factor) and distances (structure factor) that are extracted from

Table 9.1.: Mass density, chemical formula, and corresponding critical angle α_c (at $E = 8\,\text{keV}$) of even-numbered oligothiophenes and polythiophene. Densities of oligothiophenes are literature values of respective crystalline materials. [38] PT density and critical angle are derived from GISAXS measurements.

	density [g·cm^{-3}]	chemical formula	α_c [deg]
bithiophene (2T)	1.44	$C_8H_6S_2$	0.171
quaterthiophene (4T)	1.50	$C_{16}H_{10}S_4$	0.174
sexithiophene (6T)	1.55	$C_{24}H_{14}S_6$	0.177
octithiophene (8T)	1.58	$C_{32}H_{18}S_8$	0.179
polythiophene (PT)	1.46	n C_4H_2S	0.178

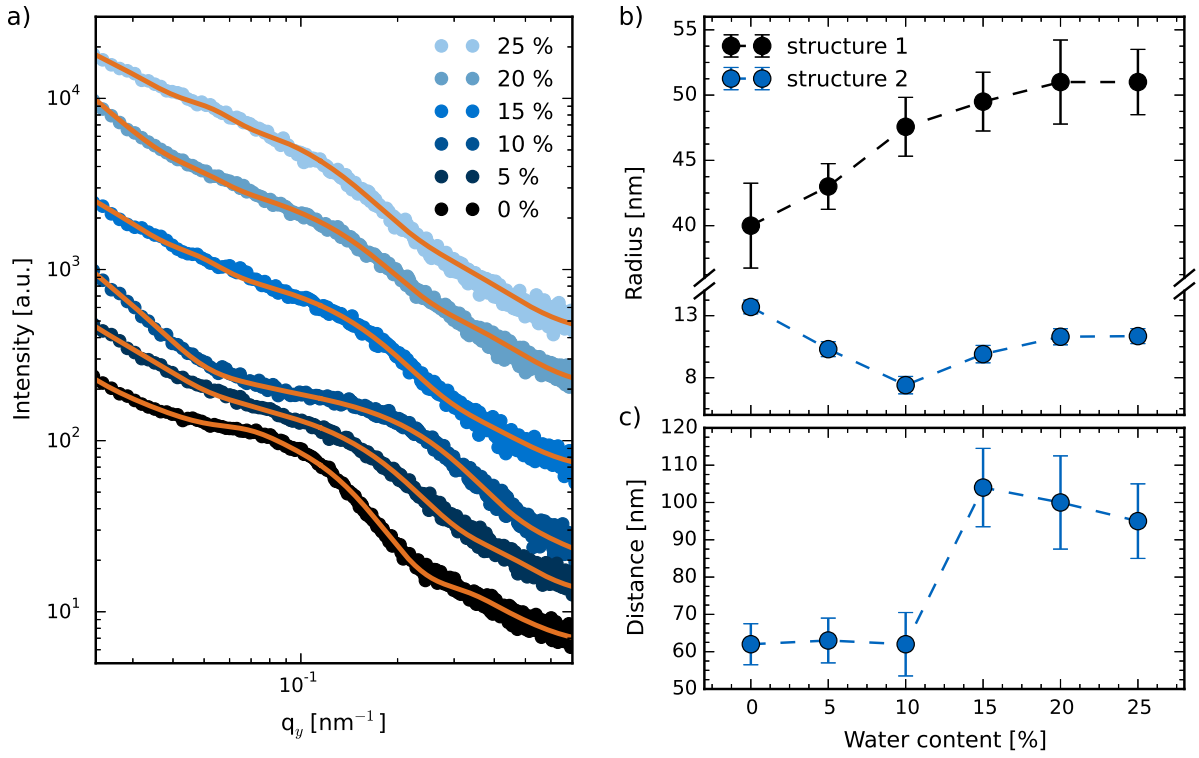

Figure 9.7.: Analysis of horizontal line cuts of GISAXS measurements on unrinsed PT thin films synthesized with different volume fractions of water in the reaction mixture. a) Horizontal line cuts, shifted with respect to each other for clearer presentation, orange lines represent the modeled data for each of the scattering curves; b,c) parameters applied for modeling the cuts: structure radii (b) and distances (c). Error bars correspond to uncertainties of the modeling, dashed lines are guides to the eye.

the applied model are plotted in figure 9.7b. The smallest object class is kept constant as background. The structure factor of the largest objects is set to 300 nm for all datasets and therefore lies outside the resolution limit due to shielding by the beam stop at low q_y and is therefore not discussed.

While the larger objects exhibit radii of 40-50 nm, the intermediate form factor is on the order of about 10 nm. The large object radius steadily grows upon increasing water fraction from (40 ± 4) nm (0 %) to (51 ± 3) nm (25 %). The intermediate structure on the other hand corresponds to the already mentioned shoulder in the horizontal cuts. This shoulder does not show a continuous shift in the same direction with increasing water content. In the three samples with lower water content, the related object radius decreases from (14 ± 1) nm (0 %), to (10 ± 1) nm (5 %), and finally (7 ± 1) nm (10 %). The inter-domain distance (structure factor) that corresponds to these objects is almost constant on the order of 60 nm (62 ± 6) nm (0 %); (63 ± 7) nm (5 %); (62 ± 9) nm (10 %). When

the water content is increased further, the appearance of the horizontal cuts drastically changes. The shoulder appears less pronounced, which is interpreted as a sudden increase in the structure factor. Moreover, the form factor is again shifted towards larger radii. The object radius stays almost constant with (10 ± 1) nm (15 %), and (11 ± 1) nm (20 %, 25 %). The respective structure factor for these three samples is modeled to be on average (100 ± 20) nm.

The evolution of the larger objects as well as the range of their radii is similar to the large structures in the rinsed films presented in figure 9.4. Therefore it is assumed that these structures are correlated to the formation of the growing pores. The intermediate structures, on the other hand, give rise to a very well pronounced scattering feature.

Identification of crystalline compounds

In order to identify which compounds in the thin film give rise to the different structures, GIWAXS measurements are performed. Figure 9.8 shows the GIWAXS pattern of the six film prior to rinsing that are discussed in this section (two top rows), as well as three exemplary datasets of the films after rinsing for comparison (bottom row).

The GIWAXS pattern of the unrinsed films show several signals of strong intensity appearing in the whole investigated q-range. While these Bragg peaks seem to appear at similar scattering vectors (and hence crystal lattice distances) for all samples, they do indeed vary in intensity as well as orientation. Some of the most distinct scattering features arise between $q = 0.8$ - $1.7\,\text{Å}^{-1}$and are highlighted in top left pattern in figure 9.8. These appear to have the strongest orientation anisotropy in the films prepared with 0 % and 15 % of water, while they are smeared out to broad rings most intensely in the 20 % sample.

In the rinsed PT films, on the other hand, all of the previously observed signals vanish. The only signal is a ring of very low intensity corresponding to the herringbone crystal structure of undoped PT which is highlighted in the scattering pattern of the 10 % sample ($q \approx 1.37\,\text{Å}^{-1}$; more information on PT crystal structure is given in chapter 7). Therefore, all the features appearing in the GIWAXS data of unrinsed PT films must derive from soluble compounds which are removed in the subsequent rinsing step. These are FeTos in both oxidation states, and short-chain oligothiophenes, because PT is the only material remaining in the films after the rinsing step. In chapter 8 the most prominent Bragg peaks of FeTos are identified at $q = 0.28\,\text{Å}^{-1}$ and $0.56\,\text{Å}^{-1}$, respectively. While the q-range of the first one is partly blocked by the beam stop in the here discussed pattern, the latter one should be visible in case FeTos strongly crystallized in the films. However, no peak or ring is found in any of the GIWAXS measurements at that position.

Hence, the crystalline material giving rise to the intense features are attributed to

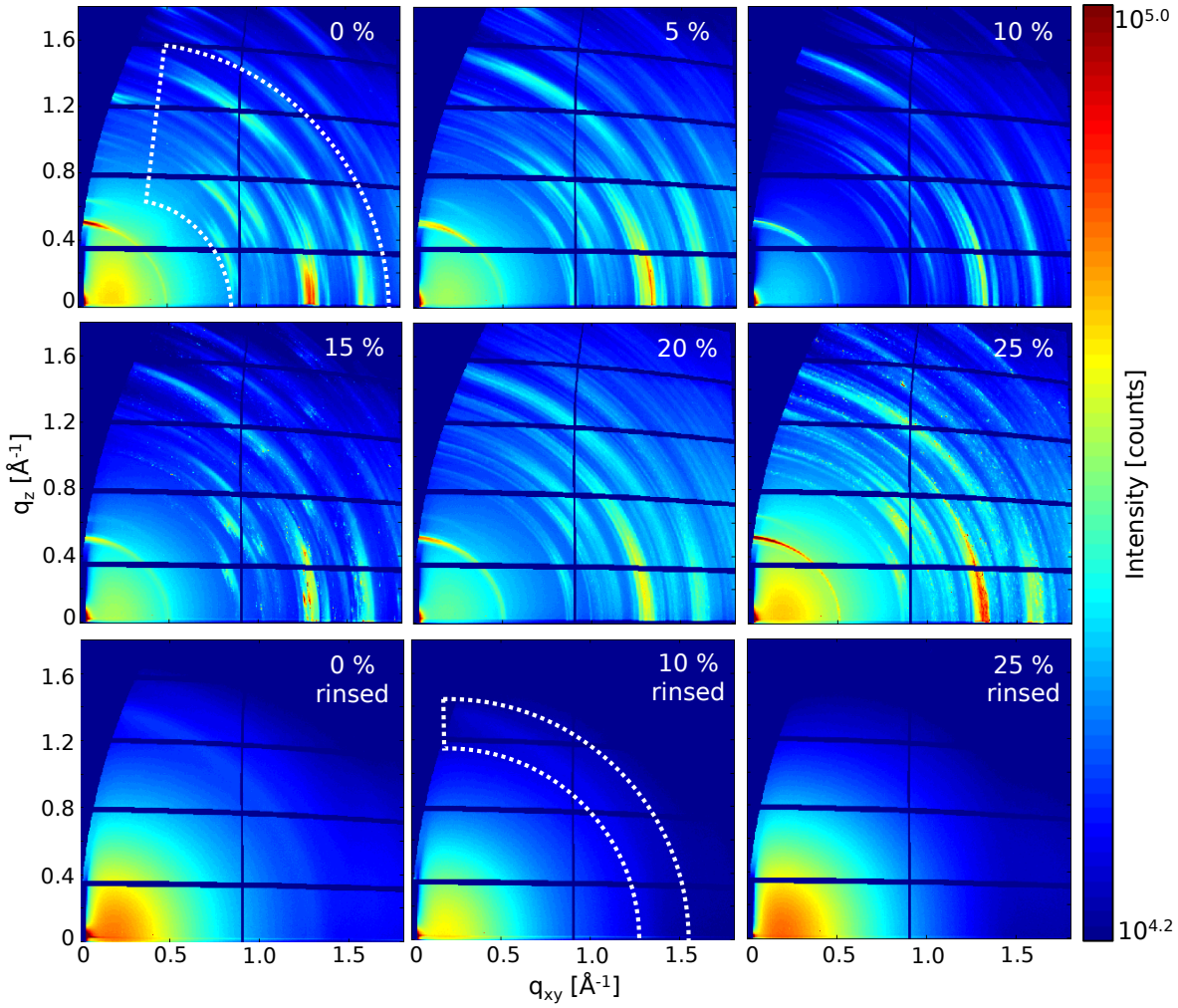

Figure 9.8.: Two dimensional GIWAXS pattern of polythiophene thin film synthesized *in situ* with varied fraction of water in the reaction mixture. First and second row: films directly after fabrication and prior to rinsing, still containing soluble byproducts of reaction. Oligothiophene signals are highlighted in 0 % image. Bottom row: selection of three samples after rinsing, which contain semiconducting PT only. Position of herringbone ring is indicated in 10 % image.

clusters of oligothiophenes. Thin films of for example sexithiophene give rise to very similar GIWAXS pattern. [132] Especially the signal appearing in horizontal direction at $q \approx 1.3$ Å^{-1} strongly indicates the presence of sexithiophene crystals in the films. Moreover, it is known that several oligothiophenes aggregate in different layered crystal phases, depending among others on deposition method, substrate surface, and temperature. [133–135] These show varying Bragg peaks in a similar range as they are observed here.

Therefore, it is concluded that the *in situ* polymerization does not only yield long, entangled polythiophene chains, but additionally short oligothiophenes that have a strong tendency to crystallize. These do not seem to participate in any further chemical reactions,

but rather form stable crystallites of probably varying crystal phase and orientation that can be rinsed out after the synthesis. The absence of FeTos crystal signals suggests that iron as well as tosylate ions are incorporated and distributed in the polymer matrix. Overall, the GIWAXS data differ strongly from the time-resolved measurements presented in chapter 8. There, only FeTos crystal signals are detected and there is no indication of oligothiophene crystal formation. The oligothiophene crystallization might be prohibited by the elevated substrate temperature during the time-resolved measurement. The origin of the varying behavior of FeTos, however, is not resolved so far.

With this, the two Yoneda peaks in the vertical GISAXS cuts (figure 9.3) are interpreted as follows. The α_f of Y1 as well as its width strongly suggest that is corresponds to a mixture of the purely organic compounds in the film, i.e. oligothiophenes and PT. Y2, on the other hand, arises at an angle too large to be explained by organics only. Since FeTos does not crystallize, it is proposed to be distributed in the film, the second critical angle is attributed to the matrix of polymer plus iron salt. This way, it is possible to attribute the intermediate structures to the oligothiophene crystals. As they appear to have a strong tendency to crystallize, they probably push out the iron ions along the crystallization front.

The proposed crystallization of the single compounds in the unrinsed films is put into context with the water content and resulting PT film morphology in the following section.

9.3. Discussion

The two previous sections discussed the morphology of *in situ* polymerized PT thin films (9.1) as well the crystallization of the reaction compounds (section 9.2) depending on the amount of water present in the reaction mixture. Finally, all of the observations from the single experiments are brought together here. Several studies have already shown that water has an impact on different aspects of the oxidative polymerization of polythiophene derivative thin films. These are shortly introduced and explained in the following.

The influence of water during *in situ* polymerization has been investigated by several research groups who focused on various aspects during the reaction and film formation. First of all, water has been shown to serve as so-called proton scavenger in the reaction mechanism. [130, 136, 137] An important step in the polymerization reaction is the deprotonation of the molecules after bond formation (see section 3.2). This way, the polymer backbone regains its aromaticity and is potentially available again for oxidation and addition of another monomer. As a result, the polymerization yield is increased by the presence of some water in the system. Aside from that, water molecules also influence the aggregation of the resulting polymer chains, as it serves as solubilizing agent for some of

the reaction byproducts. This has been shown to strongly influence the resulting electrical conductivities of the conducting thin films. [129] In vapor-phase polymerization, the oxidizing agent is typically applied to the substrate as a thin layer prior to the monomer evaporation. If FeTos is employed as oxidant, water vapor leads to the formation of salt crystallites in the otherwise amorphous material. These crystalline regions do not take part in the reaction and result in pinholes in the polymer film after rinsing out the oxidant in the end. [130,131] Finally, water has been added to metastable reaction mixtures in order to influence the solution viscosity and thereby alter its reactivity and resulting lifetime. [115]

The investigated PT films definitely exhibit a change in morphology upon the addition of water ot the reaction mixture. On the one hand, the SEM surface images reveal the presence of pores. However, the evolution of the different surface pore sizes does not show a clear trend with the water fraction. Nevertheless, the GISAXS measurements strongly indicate an increase in film porosity by more than 20 %. This is quantified by the strong shift of the effective critical angle and hence mass density of the films, as observed in the Yoneda peak. The origin of this porosity is further looked into in terms of the lateral distribution of different structure sizes. The modeling of the horizontal cuts shows the presence of two different structure sizes present in the films. The intermediate structures (about 15 nm) do not show a clear dependence on the water content. The large structures, on the other hand, steadily grow if more water is employed and are interpreted to be pores explaining the increasing porosity already mentioned. This proposed pore size evolution in the film bulk does not reflect the random changes in the surface morphology. Hence, the pore formation might be more favorable in the bulk film or maybe even at the substrate surface.

The origin of the porosity might lie in the aggregation of reaction byproducts. As these are rinsed out subsequently to the film fabrication, they are potentially able to leave air-filled pores in the insoluble PT matrix. A combined morphological analysis by means of GISAXS and GIWAXS suggests a strong crystallization of oligothiophenes in a film matrix, that is composed of PT as well as iron and tosylate ions. In GISAXS, an intermediate form factor is identified that does not steadily grow with water content. A second, larger object class, on the other hand, actually does show a similar size evolution as the pores in the rinsed films. Due to the signals present in the GIWAXS data, both structures are interpreted as oligothiophene crystals inside an iron-filled polymer matrix. The difference in the cluster sizes might derive from crystals of molecules with different chain length. The superposition of the Bragg peaks of potentially differently sized oligothiophene crystal phases makes the estimation of average crystal sizes from the GIWAXS data difficult.

Nevertheless, other complementary measurements are required for a definite assignment of the form factors to one specific material class.

Finally, it is not possible to fully explain the effect of water in the *in situ* polymerization on the final film morphology. While the films are assumed to become more porous due to constantly growing pore sizes, the reason for their formation is not resolvable with the experimental data at hand. Presumably, the addition of water enhances the crystallization of oligothiophenes of short chain length. This might happen either due to i) a changed solubility of the oligothiophenes in the solvent mixture (alcohol and water), or ii) due to a change in polymerization rates by the addition of water as a proton scavenger, that maybe leads to an increased number of reaction sites in the sample with equally more byproducts synthesized. Moreover, it is possible that iii) the effect of water is not of chemical nature, but maybe results in a changed substrate-solution interaction, leading for example to partial dewetting during the fabrication. This could also explain the different morphological properties of the surface when compared to the bulk film.

9.4. Summary

The influence of water on the film morphology of *in situ* polymerized PT thin films is investigated. For this purpose, varying fractions of water are added directly to the reaction mixtures. The morphology of the semiconducting films obtained after rinsing is investigated by means of SEM and GISAXS. It is concluded, that with increasing amounts of water the films become more porous, probably due to a growing pore size inside the film. The surface structure, on the other hand, does not exhibit a clear dependence.

Furthermore, the origin of this porosity is analyzed by GISAXS and GIWAXS measurements on the films prior to rinsing. As the GIWAXS data indicate, short oligothiophenes are formed as byproducts in the reaction and tend to strongly crystallize inside the polymer matrix. The crystal sizes and whether they match the growing pore sizes, however, cannot definitely be determined from wide-angle scattering. Nevertheless, as there are two distinct structure sizes found in the small-angle scattering pattern, these are attributed to the respective clusters. Hence, this effect is proposed to be the origin of the increased pore size in the films after rinsing out these soluble byproducts.

10. Conclusion and outlook

The objective of the presented work is to provide an insight into the structure formation during *in situ* polymerization of polythiophene (PT) thin films. Moreover, it addresses the possibilities of manipulating the morphology by exploiting intrinsic processes of the polymer synthesis. For this purpose, a solution-based *in situ* polymerization technique is developed that enables the fabrication of PT in its conducting and semiconducting state, respectively. The main focus of the thesis is set on morphological investigations by means of grazing-incidence X-ray scattering experiments as well as thin film characterization by spectroscopic and electronic analyses.

Initially, a novel solution-based polymerization routine is developed applying the concept of metastable reaction mixtures. The synthesis is established by combining key aspects of different literature-known *in situ* syntheses. So far, polythiophene films manufactured from metastable reaction mixtures have only been investigated in their doped, conductive state. Upon application of the same synthetic recipe and adaption of the post-treatment routine with respect to rinsing solvent and thermal annealing semiconducting PT films are obtained. Nevertheless, the resulting film quality is not sufficient for application in bilayer solar cells. Therefore, the oxidizing agent is exchanged for iron p-toluenesulfonate (FeTos), which is known to have an impact on film homogeneity in thin film polymerization techniques. With FeTos as oxidizing agent and modification of the processing parameters it is possible to fabricate very homogeneous PT thin films. Finally, these are employed as electron donor layers in bilayer organic solar cells with PCBM as acceptor material. The highest achieved power conversion efficiency is 0.8 % and therefore as high as those of differently prepared PT bilayer cells reported in literature.

In oxidative polymerization mechanisms an additional polymer doping is taking place during the synthesis. This is due to the fact that the employed oxidant molecules are able to further oxidize the polymer backbones. Within this work, the resulting morphological impact of this process-intrinsic doping is studied and whether it can be exploited for structural control. For this purpose, the ratio between monomer and oxidizing agent in the reaction mixture is varied. After fabrication, it is possible to keep the films in the

doped, conducting state or the undoped, semiconducting state, depending on the kind of solvent employed in the post-fabrication rinsing step. Hence, for both electronic states, the PT film states are proposed to undergo the same film formation process with the intrinsic doping taking place during the fabrication. Conductivity measurements and a spectroscopic analysis on the conducting films show that the doping level obtained during the synthesis is tunable by the employed monomer to oxidant ratio. A structural investigation by means of grazing-incidence wide-angle X-ray scattering (GIWAXS) indicates the rearrangement of the polythiophene chains at high doping level. A lamellar structure is obtained, in which π-stacks of charged polymers alternate with layers of electrostatically attached oxidant anions. Upon dedoping and removal of these counter ions a fraction of the π-stacked polymers remains in that geometry. This is a novel crystal structure for semiconducting PT which usually packs in a herringbone structure due to the repulsion of the π-orbitals of neighboring chains. However, if the aggregates are incorporated in the insoluble films the new packing stays intact even upon dedoping. The experimental observations are additionally supported by molecular dynamics simulations which verify the feasibility of the proposed π-stacked crystal structure. As a result of the altered aggregation geometry the intermolecular interaction is strongly increased, as revealed by measurements of UV/Vis absorbance and emission.

The doping happening during the synthesis is found to play a crucial role in the aggregation behavior of the resulting films. Hence, it is of high relevance to investigate the kinetics of polymerization and doping reaction as well as the film formation dynamics. In order to adress this, an experimental approach is presented that employs simultaneous time-resolved UV/Vis transmission spectroscopy and GIWAXS measurements. For this purpose, the metastable reaction mixture is deposited by slot-die coating with a customized printer setup allowing the implementation into synchrotron beamlines. Again, two different ratios between the reaction components are employed. Two four-step models are proposed, that vary significantly for the two different cases. Two major findings shall be stressed here. Firstly, the polymerization onset is dictated by the thermodynamics of the reaction. If a monomer surplus is present in the reaction mixture, the equilibrium of the activating redox reaction is reached after conversion of relatively few monomer molecules. With higher amounts of oxidant, however, the amount of activated monomers in the solution is much higher, resulting in an earlier reaction onset. Secondly, an excess of oxidizing agent leads to a high fraction of charged to neutral thiophene moieties throughout the whole process. As a consequence, the doping step of the reaction is taking place throughout the whole process rather than subsequently to the polymerization. The resulting level of doping of the chains is only dictated by the BT:FeTos ratio from the

very beginning of the chemical reactions and differs strongly between excess and deficiency conditions also in the final films.

Finally, the nanoscale morphology of the films and its manipulation by application of water as additive is studied. Other than the crystal structure, the morphology on that length scale is not assumed to affect the properties of the PT itself. However, film surface area and constitution are of high relevance for the interaction with other functional materials in device applications. In order to analyze the impact of water, it is added to the reaction mixture in varying fractions. Grazing-incidence small-angle X-ray scattering (GISAXS) strongly suggest an increasing film porosity upon higher water contents, as the critical angle and hence the density is significantly shifted. Upon addition of 25 % water to the reaction mixture the porosity is increased by 21 % as compared to the dry synthesis. The GISAXS data further indicate the presence of structures in the range of 45-55 nm which steadily grow in size and are therefore assigned to pores in the films. The origin of these pores is proposed to be the formation of reaction byproducts which form clusters during the film formation and are rinsed out later in the post-treatment. This hypothesis is tested by performing GISAXS and GIWAXS measurements on films prior to the rinsing step. The GIWAXS data show strong scattering features that indicate the presence of crystalline oligothiophenes such as sexithiophene and quarterthiophene. Other reaction components, such as the oxidizing agent FeTos, do not show crystallinity in the investigated films. The GISAXS pattern again show an increasing structure of a similar size regime than the pores in the rinsed films. Additionally, a very pronounced intermediate structure size of about 10 nm radius is visible. In summary, both structure sizes in the unrinsed films are assigned to strongly crystallized oligothiophene crystals. However, complementary measurements are required to finally confirm that interpretation. As a result of their water-dependent crystallization the oligothiophenes are proposed to leave pores of increasing size in the PT thin films.

The different aspects addressed in the framework of this thesis clearly demonstrate that the morphology of PT thin films can be tuned by exploiting the impact of process parameters involved in the film formation during *in situ* polymerization. By presenting investigations on polymer aggregation and crystal structure, a time-resolved analysis during film formation characterization, and finally a morphological study on tunable film porosity, this work proves that there is indeed a major optimization potential in the processing of insoluble (semi)conducting polymer thin films once the processes are fully understood. Nevertheless, this thesis revealed that despite of the various possibilities for influencing the film formation the fabrication process parameters need to be very precisely controlled.

A comparison of the scattering data presented in chapters 7 to 7 reveals significant differences with respect to the crystallization of the polymer as well as reaction byproducts. Whether these differences are measurement artifacts caused by changed experimental setups or are actually an indication of different underlying film evolution mechanisms is not fully resolved at this point. Therefore, future experiments should include additional complementary analytic methods which can further support the findings obtained by X-ray scattering. Moreover, the gained knowledge should be exploited for application-specific tuning of the PT thin films in order to investigate its ability to compete with other organic semiconducting materials.

A. Appendix

Details on molecular dynamics simulations

The molecular dynamics (MD) simulations presented in chapter 7 were performed in the framework of a cooperation with the research group of Prof. Dr. Stephan Geckle from University of Bayreuth. The results are published alongside the experimental data in the article *Directing the aggregation of native polythiophene during in situ polymerization.* [97]

The simulations are done with Gromacs using the Gromos 53a6 force field. [138, 139] United-atom force field topologies are used, the visual analysis of the molecular structures and trajectories is carried out with VMD. [140] The crystals containing 10 rows and 10 columns are generated with the desired lattice spacings extracted from X-ray scattering experiments. The box size is chosen, so that the crystal continues through its own mirror imaged via the periodic boundary conditions. Spring potentials with spring constants of 10000 $kJ \cdot mol^{-1} nm^{-2}$ are employed to restrict the positions of the atoms in yz direction, while their movement is not constrained along the backbone (x direction). A short NVT simulation of 400 ps is performed locally without a thermostat until the molecules are aligned in a stable configuration. The resulting π-stacked crystal structure is depicted in figure 7.6a. Upon removal of the position restraints the PT oligomers arrange in a herringbone structure (figure 7.6b).

Building the model

The structure file of the PT 10-mer is generated with JME. [141] From that, a force field file is created using the *Automated Force Field Topology Builder and Repository.* [142] The model is enhanced by calculating the partial charge distribution and potential energy surface (PES) of the dihedrals between individual thiophene rings with Gaussian09, Rev. E.01. [143] B3LYP/6-31g(d,p) level is employed in all quantum chemical calculations. Tight convergence criteria are requested in geometry optimization.The symmetry of the molecule is exploited so that the PES for the first dihedral is also used for the last and so on. The model is adjusted for MD simulations to replicate the PES calculated by the quantum chemical calculations by rotating the molecule around the angle in question with enforced rotation. The potential energy of this process was determined with the Gromacs

tool *gmx energy*. The new dihedrals are implemented with Ryckaert-Bellemans potentials. [144] Simulations are performed locally and on the Jureca Supercomputer. [145]

Bibliography

[1] C. K. Chiang, C. R. Fincher, Y. W. Park, A. J. Heeger, H. Shirakawa, E. J. Louis, S. C. Gau, and A. G. MacDiarmid, "Electrical conductivity in doped polyacetylene," *Physical Review Letters*, vol. 39, no. 17, pp. 1098–1101, 1977.

[2] Statista, "Primary energy - global consumption 1998-2016." https://www.statista.com/statistics/265598/consumption-of-primary-energy-worldwide/ (accessed: 2017-04-17), 2018.

[3] OE-A, "OE-A Roadmap for Organic and Printed Electronics: White paper." 7. ed, 2017.

[4] J. H. Noh, S. H. Im, J. H. Heo, T. N. Mandal, and S. I. Seok, "Chemical management for colorful, efficient, and stable inorganic-organic hybrid nanostructured solar cells," *Nano Letters*, vol. 13, no. 4, pp. 1764–1769, 2013.

[5] M. Kaltenbrunner, M. S. White, E. D. Głowacki, T. Sekitani, T. Someya, N. S. Sariciftci, and S. Bauer, "Ultrathin and lightweight organic solar cells with high flexibility," *Nature Communications*, vol. 3, 2012.

[6] J. A. Rogers, T. Someya, and Y. Huang, "Materials and Mechanics for Stretchable Electronics," *Science*, vol. 327, no. 1, pp. 1603–1607, 2010.

[7] B. C. Thompson and J. M. J. Fréchet, "Polymer-fullerene composite solar cells," *Angewandte Chemie - International Edition*, vol. 47, no. 1, pp. 58–77, 2008.

[8] R. R. Søndergaard, M. Hösel, and F. C. Krebs, "Roll-to-Roll fabrication of large area functional organic materials," *Journal of Polymer Science, Part B: Polymer Physics*, vol. 51, no. 1, pp. 16–34, 2013.

[9] A. C. Arias, J. D. MacKenzie, I. McCulloch, J. Rivnay, and A. Salleo, "Materials and applications for large area electronics: Solution-based approaches," *Chemical Reviews*, vol. 110, no. 1, pp. 3–24, 2010.

[10] S. R. Forrest, "Electronic Appliances on Plastic," *Nature*, vol. 428, pp. 911–918, 2004.

[11] S. M. Lee, J. H. Kwon, S. Kwon, and K. C. Choi, "A Review of Flexible OLEDs Toward Highly Durable Unusual Displays," *IEEE Transactions on Electron Devices*, vol. 64, no. 5, pp. 1922–1931, 2017.

[12] P. Sengodu and A. D. Deshmukh, "Conducting polymers and their inorganic composites for advanced Li-ion batteries: a review," *RSC Advances*, vol. 5, no. 52, pp. 42109–42130, 2015.

[13] M. E. Abdelhamid, A. P. O'Mullane, and G. A. Snook, "Storing energy in plastics: a review on conducting polymers & their role in electrochemical energy storage," *RSC Advances*, vol. 5, no. 15, pp. 11611–11626, 2015.

[14] G. Horowitz, "Organic field-effect transistors," *Advanced Materials*, vol. 10, no. 5, pp. 365–377, 1998.

[15] A. Köhler and H. Bässler, *Electronic Processes in Organic Semiconductors - An introduction*. Weinheim: Wiley-VCH Verlag, 1 ed., 2015.

[16] H. Sirringhaus, P. J. Brown, R. H. Friend, M. M. Nielsen, K. Bechgaard, B. M. W. Langeveld-Voss, a. J. H. Spiering, R. a. J. Janssen, E. W. Meijer, P. Herwig, and D. M. de Leeuw, "Two-Dimensional Charge Transport in Self-Organized, High-Mobility Conjugated Polymers," *Nature*, vol. 401, no. 6754, pp. 685–688, 1999.

[17] C. R. Singh, G. Gupta, R. Lohwasser, S. Engmann, J. Balko, M. Thelakkat, T. Thurn-Albrecht, and H. Hoppe, "Correlation of charge transport with structural order in highly ordered melt-crystallized poly(3-hexylthiophene) thin films," *Journal of Polymer Science, Part B: Polymer Physics*, vol. 51, no. 12, pp. 943–951, 2013.

[18] Y. Liu, J. Zhao, Z. Li, C. Mu, W. Ma, H. Hu, K. Jiang, H. Lin, H. Ade, and H. Yan, "Aggregation and morphology control enables multiple cases of high-efficiency polymer solar cells.," *Nature communications*, vol. 5, no. 9, p. 5293, 2014.

[19] I. Botiz and N. Stingelin, "Influence of molecular conformations and microstructure on the optoelectronic properties of conjugated polymers," *Materials*, vol. 7, no. 3, pp. 2273–2300, 2014.

[20] M. T. Dang, L. Hirsch, and G. Wantz, "P3HT:PCBM, best seller in polymer photovoltaic research," *Advanced Materials*, vol. 23, no. 31, pp. 3597–3602, 2011.

[21] G. Li, R. Zhu, and Y. Yang, "Polymer solar cells," *Nature Photonics*, vol. 6, no. 3, pp. 153–161, 2012.

[22] H. Shi, C. Liu, Q. Jiang, and J. Xu, "Effective Approaches to Improve the Electrical Conductivity of PEDOT:PSS: A Review," *Advanced Electronic Materials*, vol. 1, no. 4, pp. 1–16, 2015.

[23] K. Fehse, K. Walzer, K. Leo, W. Lövenich, and A. Elschner, "Highly conductive polymer anodes as replacements for inorganic materials in high-efficiency organic light-emitting diodes," *Advanced Materials*, vol. 19, no. 3, pp. 441–444, 2007.

[24] Y. H. Kim, C. Sachse, M. L. MacHala, C. May, L. Müller-Meskamp, and K. Leo, "Highly conductive PEDOT:PSS electrode with optimized solvent and thermal post-treatment for ITO-free organic solar cells," *Advanced Functional Materials*, vol. 21, pp. 1076–1081, 2011.

[25] F. C. Krebs, "Fabrication and processing of polymer solar cells: A review of printing and coating techniques," *Solar Energy Materials and Solar Cells*, vol. 93, no. 4, pp. 394–412, 2009.

[26] S. A. Gevorgyan and F. C. Krebs, "Bulk heterojunctions based on native polythiophene," *Chemistry of Materials*, vol. 20, no. 13, pp. 4386–4390, 2008.

[27] J. Roncali, "Conjugated Poly(thiophenes): Synthesis, Functionalizatlon, and Applications," *Chemical Reviews*, vol. 92, pp. 711–738, 1992.

[28] G. Sabouraud, S. Sadki, and N. Brodie, "The mechanisms of pyrrole electropolymerization," *Chemical Society Reviews*, vol. 29, no. 5, pp. 283–293, 2000.

[29] N. K. Guimard, N. Gomez, and C. E. Schmidt, "Conducting polymers in biomedical engineering," *Progress in Polymer Science*, vol. 32, no. 8-9, pp. 876–921, 2007.

[30] Y. Wei, C. C. Chan, J. Tian, G. W. Jang, and K. F. Hsueh, "Electrochemical polymerization of thiophenes in the presence of bithiophene or terthiophene: kinetics and mechanism of the polymerization," *Chemistry of Materials*, vol. 3, no. 5, pp. 888–897, 1991.

[31] R. Valaski, C. D. Canestraro, L. Micaroni, R. M. Mello, and L. S. Roman, "Organic photovoltaic devices based on polythiophene films electrodeposited on FTO substrates," *Solar Energy Materials and Solar Cells*, vol. 91, no. 8, pp. 684–688, 2007.

[32] E. Bravo-Grimaldo, S. Hachey, C. G. Cameron, and M. S. Freund, "Metastable Reaction Mixtures for the in Situ Polymerization of Conducting Polymers," *Macromolecules*, pp. 7166–7170, 2007.

[33] D. C. Borrelli, M. C. Barr, V. Bulović, and K. K. Gleason, "Bilayer heterojunction polymer solar cells using unsubstituted polythiophene via oxidative chemical vapor deposition," *Solar Energy Materials and Solar Cells*, vol. 99, pp. 190–196, 2012.

[34] D. C. Borrelli, S. Lee, and K. K. Gleason, "Optoelectronic properties of polythiophene thin films and organic TFTs fabricated by oxidative chemical vapor deposition," *Journal of Materials Chemistry C*, vol. 2, no. 35, pp. 7223–7231, 2014.

[35] P. Kovacik, H. E. Assender, and A. A. R. Watt, "Morphology control in co-evaporated bulk heterojunction solar cells," *Solar Energy Materials and Solar Cells*, vol. 117, pp. 22–28, 2013.

[36] B. Kolodziejczyk, D. Mayevsky, and B. Winther-jensen, "Enhanced absorption spectra of conducting polymers," *RCS Advances*, pp. 4568–4573, 2013.

[37] B. Kolodziejczyk, O. Winther-jensen, R. Kerr, P. Firbas, and B. Winther-jensen, "Reactive & Functional Polymers Tuning the morphology of electroactive polythiophene nano-structures," *REACTIVE AND FUNCTIONAL POLYMERS*, vol. 86, pp. 60–66, 2015.

[38] D. Fichou and C. Ziegler, "Structure and Properties of Oligothiophenes in the Solid State: Single Crystals and Thin Films," in *Handbook of Oligo- and Polythiophenes*, ch. 4, pp. 183–282, Weinheim: Wiley-VCH Verlag, 1 ed., 1998.

[39] B. Tieke, *Makromolekulare Chemie*. Weinheim: Wiley-VCH Verlag, 3 ed., 2014.

[40] M. Wright and A. Uddin, "Organic—inorganic hybrid solar cells: A comparative review," *Solar Energy Materials and Solar Cells*, vol. 107, pp. 87–111, 2012.

[41] T. Johansson, W. Mammo, M. Svensson, M. R. Andersson, and O. Inganäs, "Electrochemical bandgaps of substituted polythiophenes," *J. Mater. Chem.*, vol. 13, no. 6, pp. 1316–1323, 2003.

[42] R. Kroon, M. Lenes, J. C. Hummelen, P. W. M. Blom, and B. De Boer, "Small bandgap polymers for organic solar cells (polymer material development in the last 5 years)," *Polymer Reviews*, vol. 48, no. 3, pp. 531–582, 2008.

[43] H. Bässler, "Charge Transport in Disordered Organic Photoconductors," *Physica Status Solidi (B)*, vol. 175, no. 1, pp. 15–56, 1993.

[44] F. C. Spano and C. Silva, "H- and J-aggregate behavior in polymeric semiconductors.," *Annual review of physical chemistry*, vol. 65, pp. 477–500, 2014.

[45] F. C. Spano, "The fundamental photophysics of conjugated oligomer herringbone aggregates," *The Journal of Chemical Physics*, vol. 118, no. 2, pp. 981–994, 2003.

[46] J. Clark, C. Silva, R. H. Friend, and F. C. Spano, "Role of intermolecular coupling in the photophysics of disordered organic semiconductors: Aggregate emission in regioregular polythiophene," *Physical Review Letters*, vol. 98, no. 20, pp. 1–4, 2007.

[47] H. Hoppe and N. S. Sariciftci, "Organic solar cells: An overview," *Journal of Materials Research*, vol. 19, no. 07, pp. 1924–1945, 2011.

[48] G. Dennler, M. C. Scharber, and C. J. Brabec, "Polymer-Fullerene Bulk-Heterojunction Solar Cells," *Advanced Materials*, vol. 21, no. 13, pp. 1323–1338, 2009.

[49] D. Hertel and H. Bässler, "Photoconduction in amorphous organic solids," *ChemPhysChem*, vol. 9, no. 5, pp. 666–688, 2008.

[50] C. Deibel and V. Dyakonov, "Polymer-fullerene bulk heterojunction solar cells," *Reports on Progress in Physics*, vol. 73, no. 9, 2010.

[51] A. Malinauskas, "Chemical deposition of conducting polymers," *Polymer*, vol. 42, no. 9, pp. 3957–3972, 2001.

[52] R. J. Waltman and J. Bargon, "Electrically conducting polymers: a review of the electropolymerization reaction, of the effects of chemical structure on polymer film properties, and of applications towards technology," *Canadian Journal of Chemistry*, vol. 64, pp. 76–95, 1986.

[53] J. P. Aime, F. Bargain, M. Schott, H. Eckhardt, G. G. Miller, and R. L. Elsenbaumer, "Structural study of doped and undoped polythiophene in solution by small-angle Neutron Scattering," *Physical Review Letters*, vol. 62, no. 1, pp. 55–58, 1989.

[54] U. Salzner, "Theoretical investigation of excited states of oligothiophenes and of their monocations," *Journal of Chemical Theory and Computation*, vol. 3, no. 3, pp. 1143–1157, 2007.

[55] B. Winther-Jensen, M. Forsyth, K. West, J. Wenzel, P. Bayley, S. Pas, and D. R. Macfarlane, "Order-disorder transitions in poly (3,4-ethylenedioxythiophene)," *Polymer*, vol. 49, 2008.

[56] S. L. McFarlane, B. A. Deore, N. Svenda, and M. S. Freund, "A One-Step, Organic-Solvent Processable Synthesis of PEDOT Thin Films via in Situ Metastable Chemical Polymerization," *Macromolecules*, vol. 43, no. 24, pp. 10241–10245, 2010.

[57] M. Tolan, *X-Ray Scattering from Soft-Matter Thin Films*. Berlin: Springer Berlin Heidelberg, 148 ed., 2013.

[58] Z. Jiang, "GIXSGUI: A MATLAB toolbox for grazing-incidence X-ray scattering data visualization and reduction, and indexing of buried three-dimensional periodic nanostructured films," *Journal of Applied Crystallography*, vol. 48, pp. 917–926, 2015.

[59] J. L. Baker, L. H. Jimison, S. Mannsfeld, S. Volkman, S. Yin, V. Subramanian, A. Salleo, a. P. Alivisatos, and M. F. Toney, "Quantification of thin film crystallographic orientation using X-ray diffraction with an area detector.," *Langmuir : the ACS journal of surfaces and colloids*, vol. 26, no. 11, pp. 9146–9151, 2010.

[60] D. M. Smilgies, "Scherrer grain-size analysis adapted to grazing-incidence scattering with area detectors," *Journal of Applied Crystallography*, vol. 42, no. 6, pp. 1030–1034, 2009.

[61] Y. Yoneda, "Anomalous surface reflection of X rays," *Physical Review*, vol. 131, no. 5, pp. 2010–2013, 1963.

[62] V. Holý and T. Baumbach, "Nonspecular x-ray reflection from rough multilayers," *Physical Review B*, vol. 49, no. 15, pp. 10668–10676, 1994.

[63] S. K. Sinha, E. B. Sirota, S. Garoff, and H. B. Stanley, "X-ray and neutron scattering from rough surfaces," vol. 38, no. 4, pp. 2297–2312, 1988.

[64] A. Naudon, D. Babonneau, D. Thiaudière, and S. Lequien, "Grazing incidence small-angle X-ray scattering applied to the characterization of aggregates in surface regions," *Physica B*, vol. 283, pp. 69–74, 2000.

[65] J. Tauc, R. Grigorovici, and A. Vancu, "Optical Properties and Electronic Structure of Amorphous Germanium," *Physica Status Solidi (B)*, vol. 15, no. 2, pp. 627–637, 1966.

[66] N. Ghobadi, "Band Gap Determination Using Absorption Spectrum Fitting Procedure," *International Nano Letters*, vol. 3:2, no. 1, 2013.

[67] A. Armin, G. Juska, M. Ullah, M. Velusamy, P. L. Burn, P. Meredith, and A. Pivrikas, "Balanced carrier mobilities: Not a necessary condition for high-efficiency thin organic solar cells as determined by MIS-CELIV," *Advanced Energy Materials*, vol. 4, no. 4, pp. 1–8, 2014.

[68] G. Juška, N. Nekrašas, and K. Genevičius, "Investigation of charge carriers transport from extraction current transients of injected charge carriers," *Journal of Non-Crystalline Solids*, vol. 358, no. 4, pp. 748–750, 2012.

[69] S. Mansi, *Optimization of a charge carrier mobility measurement setup for the characterization of semiconducting organic thin films*. Bachelor's thesis, Technische Universität München, 2016.

[70] C. A. Schneider, W. S. Rasband, and K. W. Eliceiri, "NIH Image to ImageJ: 25 years of image analysis," *Nature Methods*, vol. 9, no. 7, pp. 671–675, 2012.

[71] A. Hexemer, W. Bras, J. Glossinger, E. Schaible, E. Gann, R. Kirian, A. MacDowell, M. Church, B. Rude, and H. Padmore, "A SAXS/WAXS/GISAXS Beamline with Multilayer Monochromator," *Journal of Physics: Conference Series*, vol. 247, p. 012007, 2010.

[72] G. Ciatto, M. H. Chu, P. Fontaine, N. Aubert, H. Renevier, and J. L. Deschanvres, "SIRIUS: A new beamline for in situ X-ray diffraction and spectroscopy studies of advanced materials and nanostructures at the SOLEIL Synchrotron," *Thin Solid Films*, vol. 617, pp. 48–54, 2016.

[73] G. Benecke, W. Wagermaier, C. Li, M. Schwartzkopf, G. Flucke, R. Hoerth, I. Zizak, M. Burghammer, E. Metwalli, P. Müller-Buschbaum, M. Trebbin, S. Förster, O. Paris, S. V. Roth, and P. Fratzl, "A customizable software for fast reduction and analysis of large X-ray scattering data sets: Applications of the new DPDAK package to small-angle X-ray scattering and grazing-incidence small-angle X-ray scattering," *Journal of Applied Crystallography*, vol. 47, no. 5, pp. 1797–1803, 2014.

[74] A. F. Diaz, J. Crowley, J. Bargon, G. P. Gardini, and J. B. Torrance, "Electrooxidation of aromatic oligomers and conducting polymers," *Journal of Electroanalytical Chemistry*, vol. 121, no. C, pp. 355–361, 1981.

[75] M. S. Freund, C. Karp, and N. S. Lewis, "Growth of thin processable films of poly(pyrrole) using phosphomolybdate clusters," *Inorganica Chimica Acta*, vol. 240, no. 1-2, pp. 447–451, 1995.

[76] F. Jonas, G. Heywang, W. Schmidtberg, J. Heinze, and D. M., *Polythiophenes, process for their preparation and their use*. Ep 339 340, Bayer AG, 1988.

[77] A. F. Hollemann, E. Wiberg, and N. Wiberg, *Lehrbuch der Anorganischen Chemie*. Berlin, New York: de Gruyter Verlag, 102 ed., 2007.

[78] B. R. Saunders, "Hybrid polymer/nanoparticle solar cells: Preparation, principles and challenges," *Journal of Colloid and Interface Science*, vol. 369, no. 1, pp. 1–15, 2012.

[79] A. Elschner, "The in situ polymerization of EDOT to PEDOT," in *PEDOT - principles and applications of an intrinsically conductive polymer*, pp. 91–112, 2011.

[80] L. Hofbauer, *Influence of a Commodity Polymer on the Active Layer of Organic Photovoltaics*. Bachelor's thesis, Technische Universität München, 2014.

[81] S. Pröller, D. Moseguí González, C. Zhu, E. Schaible, C. Wang, P. Müller-Buschbaum, A. Hexemer, and E. M. Herzig, "Note: Setup for chemical atmospheric control during in situ grazing incidence X-ray scattering of printed thin films," *Review of Scientific Instruments*, vol. 88, no. 6, p. 066101, 2017.

[82] S. Nejati and K. K. S. Lau, "Chemical vapor deposition synthesis of tunable unsubstituted polythiophene," *Langmuir*, vol. 27, no. 24, pp. 15223–15229, 2011.

[83] N. Massonnet, A. Carella, O. Jaudouin, P. Rannou, G. Laval, C. Celle, and J.-P. Simonato, "Improvement of the Seebeck coefficient of PEDOT:PSS by chemical reduction combined with a novel method for its transfer using free-standing thin films," *Journal of Materials Chemistry C*, vol. 2, no. 7, pp. 1278–1283, 2014.

[84] S. A. Chen and J. M. Ni, "Structure/properties of conjugated conductive polymers. 1. Neutral poly(3-alkythiophene)s," *Macromolecules*, vol. 25, no. 23, pp. 6081–6089, 1992.

[85] D. Kelkar and A. Chourasia, "Structural properties of Polythiophene doped with FeCl3," *Chemistry & Chemical Technology*, vol. 5, no. 3, pp. 309–315, 2011.

[86] M. Bjerring, J. S. Nielsen, N. C. Nielsen, and F. C. Krebs, "Polythiophene by Solution Processing," *Macromolecules*, vol. 40, pp. 6012–6013, 2007.

[87] F. C. Spano, J. Clark, C. Silva, and R. H. Friend, "Determining exciton coherence from the photoluminescence spectral line shape in poly(3-hexylthiophene) thin films," *Journal of Chemical Physics*, vol. 130, no. 7, p. 074904, 2009.

[88] F. C. Spano, "Modeling disorder in polymer aggregates: The optical spectroscopy of regioregular poly(3-hexylthiophene) thin films," *The Journal of Chemical Physics*, vol. 122, no. 23, p. 234701, 2005.

[89] O. Bubnova, Z. U. Khan, A. Malti, S. Braun, M. Fahlman, M. Berggren, and X. Crispin, "Optimization of the thermoelectric figure of merit in the conducting polymer poly(3,4-ethylenedioxythiophene)," *Nature Materials*, vol. 10, no. 6, pp. 429–433, 2011.

[90] J. P. Lock, S. G. Im, and K. K. Gleason, "Oxidative chemical vapor deposition of electrically conducting poly(3,4-ethylenedioxythiophene) films," *Macromolecules*, vol. 39, no. 16, pp. 5326–5329, 2006.

[91] Z. U. Khan, O. Bubnova, J. Jafari, R. Brooke, X. Liu, R. Gabrielsson, T. Ederth, D. R. Evans, J. W. Andreasen, and X. Crispin, "Acido-basic control of the thermoelectric properties of poly(3,4-ethylenedioxythiophene)tosylate (PEDOT-Tos) thin films," *Journal of Materials Chemistry C*, vol. 3, pp. 10616–10623, 2015.

[92] B. Winther-Jensen, J. Chen, K. West, and G. Wallace, "Vapor phase polymerization of pyrrole and thiophene using iron(III) sulfonates as oxidizing agents," *Macromolecules*, vol. 37, no. 16, pp. 5930–5935, 2004.

[93] B. Winther-Jensen, D. W. Breiby, and K. West, "Base inhibited oxidative polymerization of 3,4-ethylenedioxythiophene with iron(III)tosylate," *Synthetic Metals*, vol. 152, no. 1-3, pp. 1–4, 2005.

[94] T. Y. Kim, J. E. Kim, and K. S. Suh, "Effects of alcoholic solvents on the conductivity of tosylate-doped poly(3,4-ethylenedioxythiophene) (PEDOT-OTs)," *Polymer International*, vol. 55, no. 1, pp. 80–86, 2006.

[95] U. Zhokhavets, T. Erb, G. Gobsch, M. Al-Ibrahim, and O. Ambacher, "Relation between absorption and crystallinity of poly(3-hexylthiophene)/ fullerene films for plastic solar cells," *Chemical Physics Letters*, vol. 418, no. 4-6, pp. 347–350, 2006.

[96] F. C. Krebs and H. Spanggaard, "Significant Improvement of Polymer Solar Cell Stability," *Chemistry of Materials*, vol. 17, no. 21, pp. 5235–5237, 2005.

[97] J. Lebert, E. M. Kratzer, A. Bourdick, M. Coric, S. Gekle, and E. M. Herzig, "Directing the Aggregation of Native Polythiophene during in situ Polymerization," *ACS Omega*, vol. 3, no. 6, p. 6388–6394, 2018.

[98] K. Kaneto, K. Yoshino, and Y. Inuishi, "Electrical and optical properties of polythiophene prepared by electrochemical polymerization," *Solid State Communications*, vol. 46, no. 5, pp. 389–391, 1983.

[99] S. S. Jeon, S. J. Yang, K. J. Lee, and S. S. Im, "A facile and rapid synthesis of unsubstituted polythiophene with high electrical conductivity using binary organic solvents," *Polymer*, vol. 51, no. 18, pp. 4069–4076, 2010.

[100] X. G. Li, J. Li, Q. K. Meng, and M. R. Huang, "Interfacial synthesis and widely controllable conductivity of polythiophene microparticles," *Journal of Physical Chemistry B*, vol. 113, no. 29, pp. 9718–9727, 2009.

[101] T. Yamamoto, A. Morita, Y. Miyazaki, T. Maruyama, H. Wakayama, Z.-H. Zhou, Y. Nakamura, T. Kanbara, S. Sasaki, and K. Kubota, "Preparation of π-conjugated Poly(thiophene-2,5-diyl), Poly(p-phenylene), and Related Polymers Using Zerovalent Nickel Complexes. Linear Structure and Properties of the π-conjugated Polymers," *Macromolecules*, vol. 25, pp. 1214–1223, 1992.

[102] K. R. Miller, Larry L.; Mann, "π-Dimers and π-Stacks in Solution and in Conducting Polymers," *Accounts of Chemical Research*, vol. 4842, pp. 417–423, 1996.

[103] G. Brocks, "Π-Dimers of Oligothiophene Cations," *The Journal of Chemical Physics*, vol. 112, no. 12, pp. 5353–5363, 2000.

[104] A. Chaalane, D. Mahi, and A. Dkhissi, "Structural and electronic properties of doped oligothiophenes in the presence of p-toluenesulfonate acids," *Theoretical Chemistry Accounts*, vol. 134, no. 5, pp. 1–7, 2015.

[105] S. Brückner and W. Porzio, "The structure of neutral polythiophene. An application of the Rietveld method," *Die Makromolekulare Chemie*, vol. 189, no. 4, pp. 961–967, 1988.

[106] Z. Mo, K. B. Lee, Y. B. Moon, M. Kobayashi, A. J. Heeger, and F. Wudl, "X-ray Scattering from Polythiophene: Crystallinity and Crystallographic Structure," *Macromolecules*, vol. 18, no. 10, pp. 1972–1977, 1985.

[107] S. G. Youm, E. Hwang, C. A. Chavez, X. Li, S. Chatterjee, K. L. Lusker, L. Lu, J. Strzalka, J. F. Ankner, Y. Losovyj, J. C. Garno, and E. E. Nesterov, "Polythiophene thin films by surface-initiated polymerization: Mechanistic and structural studies," *Chemistry of Materials*, vol. 28, no. 13, pp. 4787–4804, 2016.

[108] K. A. Page, A. Kusoglu, C. M. Stafford, S. Kim, R. J. Kline, and A. Z. Weber, "Confinement-driven increase in ionomer thin-film modulus," *Nano Letters*, vol. 14, pp. 2299–2304, 2014.

[109] S. J. Van Der Gaast and A. J. Vaars, "A Method to Eliminate the Background in X-ray Diffraction Patterns of Oriented Clay Mineral Samples," *Clay Minerals*, vol. 16, pp. 383–393, 1981.

[110] T. J. Prosa, M. J. Winokur, J. Moulton, P. Smith, and a. J. Heeger, "X-ray Structural Studies of Poly(3-alkylthiophenes): An Example of An Inverse Comb," *Macromolecules*, vol. 25, no. 17, pp. 4364–4372, 1992.

[111] K. E. Aasmundtveit, E. J. Samuelsent, L. A. A. Pettersson, T. Johansson, and R. Feidenhans, "Structure of thin films of poly(3,4-ethylenedioxythiophene)," vol. 101, no. 0379, pp. 561–564, 1999.

[112] F. Panzer, H. Bässler, and A. Köhler, "Temperature Induced Order–Disorder Transition in Solutions of Conjugated Polymers Probed by Optical Spectroscopy," *J. Phys. Chem. Lett.*, vol. 8, pp. 114–125, 2016.

[113] H. Koezuka, A. Tsumura, and T. Ando, "Field-effect Transistor with Polythiophene thin film," *Synthetic Metals*, vol. 18, pp. 699–704, 1987.

[114] P. Vanlaeke, A. Swinnen, I. Haeldermans, G. Vanhoyland, T. Aernouts, D. Cheyns, C. Deibel, J. D'Haen, P. Heremans, J. Poortmans, and J. Manca, "P3HT/PCBM bulk heterojunction solar cells: Relation between morphology and electro-optical characteristics," *Solar Energy Materials and Solar Cells*, vol. 90, no. 14, pp. 2150–2158, 2006.

[115] T. S. Hansen, K. West, O. Hassager, and N. B. Larsen, "Integration of conducting polymer network in non-conductive polymer substrates," *Synthetic Metals*, vol. 156, no. 18-20, pp. 1203–1207, 2006.

[116] C. L. Huisman, A. Huijser, H. Donker, J. Schoonman, and A. Goossens, "UV Polymerization of Oligothiophenes and Their Application in Nanostructured Heterojunction Solar Cells," *Macromolecules*, vol. 37, no. 15, pp. 5557–5564, 2004.

[117] D. Fichou, ed., *Handbook of Oligo- and Polythiophenes*. Weinheim: Wiley-VCH Verlag, 1 ed., 1999.

[118] K. R. Fewings, P. C. Junk, D. Georganopoulou, P. D. Prince, and J. W. Steed, "Supramolecular interactions in metal tosylate complexes," *Polyhedron*, vol. 20, no. 7-8, pp. 643–649, 2001.

[119] Y. Kim, S. Cook, S. M. Tuladhar, S. A. Choulis, J. Nelson, J. R. Durrant, D. D. C. Bradley, M. Giles, I. McCulloch, C. S. Ha, and M. Ree, "A strong regioregularity effect in self-organizing conjugated polymer films and high-efficiency polythiophene:fullerene solar cells," *Nature Materials*, vol. 5, no. 3, pp. 197–203, 2006.

[120] J. Clark, J.-F. Chang, F. C. Spano, R. H. Friend, and C. Silva, "Determining exciton bandwidth and film microstructure in polythiophene films using linear absorption spectroscopy," *Applied Physics Letters*, vol. 94, no. 16, p. 163306, 2009.

[121] H. Ma, H.-L. Yip, F. Huang, and A. K.-Y. Jen, "Interface Engineering for Organic Electronics," *Advanced Functional Materials*, vol. 20, no. 9, pp. 1371–1388, 2010.

[122] D. Cheyns, K. Vasseur, C. Rolin, J. Genoe, J. Poortmans, and P. Heremans, "Nanoimprinted semiconducting polymer films with 50 nm features and their application to organic heterojunction solar cells," *Nanotechnology*, vol. 19, no. 42, 2008.

[123] H. Hlaing, X. Lu, T. Hofmann, K. G. Yager, C. T. Black, and B. M. Ocko, "Nanoimprint-induced molecular orientation in semiconducting polymer nanostructures," *ACS Nano*, vol. 5, no. 9, pp. 7532–7538, 2011.

[124] J. P. Singer, M. Gopinadhan, Z. Shao, A. D. Taylor, J. Schroers, and C. O. Osuji, "Nanoimprinting sub-100 nm features in a photovoltaic nanocomposite using durable bulk metallic glass molds," *ACS Applied Materials and Interfaces*, vol. 7, no. 6, pp. 3456–3461, 2015.

[125] D. Wu, F. Xu, B. Sun, R. Fu, H. He, and K. Matyjaszewski, "Design and preparation of porous polymers," *Chemical Reviews*, vol. 112, no. 7, pp. 3959–4015, 2012.

[126] C. Gu, N. Huang, Y. Chen, H. Zhang, S. Zhang, F. Li, Y. Ma, and D. Jiang, "Porous Organic Polymer Films with Tunable Work Functions and Selective Hole and Electron Flows for Energy Conversions," *Angewandte Chemie - International Edition*, vol. 55, no. 9, pp. 3049–3053, 2016.

[127] S. Das, P. Heasman, T. Ben, and S. Qiu, "Porous Organic Materials: Strategic Design and Structure-Function Correlation," *Chemical Reviews*, vol. 117, no. 3, pp. 1515–1563, 2017.

[128] C. Gu, N. Huang, Y. Chen, L. Qin, H. Xu, S. Zhang, F. Li, Y. Ma, and D. Jiang, "π-Conjugated Microporous Polymer Films: Designed Synthesis, Conducting Properties, and Photoenergy Conversions," *Angewandte Chemie - International Edition*, vol. 54, no. 46, pp. 13594–13598, 2015.

[129] H. Goktas, X. Wang, A. Ugur, and K. K. Gleason, "Water-Assisted Vapor Deposition of PEDOT Thin Film," *Macromolecular Rapid Communications*, vol. 36, no. 13, pp. 1283–1289, 2015.

[130] M. Fabretto, K. Zuber, C. Hall, P. Murphy, and H. J. Griesser, "The role of water in the synthesis and performance of vapour phase polymerised PEDOT electrochromic devices," *Journal of Materials Chemistry*, vol. 19, no. 42, pp. 7871–7878, 2009.

[131] K. Zuber, M. Fabretto, C. Hall, and P. Murphy, "Improved PEDOT Conductivity via Suppression of Crystallite Formation in Fe (III) Tosylate During Vapor Phase

Polymerization," *Macromolecular Rapid Communications*, vol. 29, pp. 1503–1508, 2008.

[132] A. Moser, I. Salzmann, M. Oehzelt, A. Neuhold, H. G. Flesch, J. Ivanco, S. Pop, T. Toader, D. R. Zahn, D. M. Smilgies, and R. Resel, "A disordered layered phase in thin films of sexithiophene," *Chemical Physics Letters*, vol. 574, pp. 51–55, 2013.

[133] J.-O. Vogel, I. Salzmann, S. Duhm, M. Oehzelt, J. P. Rabe, and N. Koch, "Phase-separation and mixing in thin films of co-deposited rod-like conjugated molecules," *Journal of Materials Chemistry*, vol. 20, no. 20, pp. 4055–4066, 2010.

[134] C. Lorch, R. Banerjee, C. Frank, J. Dieterle, A. Hinderhofer, A. Gerlach, and F. Schreiber, "Growth of competing crystal phases of α-sexithiophene studied by real-time in situ X-ray scattering," *Journal of Physical Chemistry C*, vol. 119, no. 1, pp. 819–825, 2015.

[135] B. C. Hoffman, T. Mcafee, S. Pazoki, A. Apperson, B. T. O'Connor, and D. B. Dougherty, "Temperature controlled interlayer disorder in ultrathin films of α-sexithiophene," *Thin Solid Films*, vol. 642, no. September, pp. 182–187, 2017.

[136] M. Mueller, M. Fabretto, D. Evans, P. Hojati-Talemi, C. Gruber, and P. Murphy, "Vacuum vapour phase polymerization of high conductivity PEDOT: Role of PEG-PPG-PEG, the origin of water, and choice of oxidant," *Polymer*, vol. 53, no. 11, pp. 2146–2151, 2012.

[137] A. Elschner, S. Kirchmeyer, W. Lövenich, U. Merker, and K. Reuter, "From EDOT to PEDOT Oxidative Polymerization and other Routes," in *PEDOT - principles and applications of an intrinsically conductive polymer*, pp. 67–82, CRC Press, 2010.

[138] B. Hess, C. Kutzner, D. van der Spoel, and E. Lindahl, "GROMACS 4: Algorithms for highly efficient, load-balanced, and scalable molecular simulation," *Journal of Chemical Theory and Computation*, vol. 4, pp. 435–447, 2008.

[139] C. Oostenbrink, A. Villa, A. E. Mark, and W. F. Van Gunsteren, "A biomolecular force field based on the free enthalpy of hydration and solvation: The GROMOS force-field parameter sets 53A5 and 53A6," 2004.

[140] W. Humphrey, A. Dalke, and K. Schulten, "VMW: Visual Molecular Dynamics," *Journal of Molecular Graphics*, vol. 14, no. 1, pp. 33–38, 1996.

[141] P. Ertl, "Molecular structure input on the web.," *Journal of cheminformatics*, vol. 2, no. 1, p. 1, 2010.

[142] A. K. Malde, L. Zuo, M. Breeze, M. Stroet, D. Poger, P. C. Nair, C. Oostenbrink, and A. E. Mark, "An Automated force field Topology Builder (ATB) and repository: Version 1.0," *Journal of Chemical Theory and Computation*, vol. 7, no. 12, pp. 4026–4037, 2011.

[143] M. J. Frisch, G. W. Trucks, H. B. Schlegel, G. E. Scuseria, M. A. Robb, J. R. Cheeseman, G. Scalmani, V. Barone, B. Mennucci, G. A. Petersson, H. Nakatsuji, M. Caricato, X. Li, H. P. Hratchian, A. F. Izmaylov, J. Bloino, G. Zheng, J. L. Sonnenberg, M. Hada, M. Ehara, K. Toyota, R. Fukuda, J. Hasegawa, M. Ishida, T. Nakajima, Y. Honda, O. Kitao, H. Nakai, T. Vreven, J. A. Jr., Montgomery, J. E. Peralta, F. Ogliaro, M. Bearpark, J. J. Heyd, E. Brothers, K. N. Kudin, V. N. Staroverov, T. Keith, R. Kobayashi, J. Normand, K. Raghavachari, A. Rendell, J. C. Burant, S. S. Iyengar, J. Tomasei, M. Cossi, N. Rega, J. M. Millam, M. Klene, J. E. Knox, J. B. Cross, V. Bakken, C. Adamo, J. Jaramillo, R. Gomperts, R. E. Stratmann, O. Yazyev, A. J. Austin, R. Cammi, C. Pomelli, J. W. Ochterski, R. L. Martin, K. Morokuma, V. G. Zakrzewski, G. A. Voth, P. Salvador, J. J. Dannenberg, S. Dapprich, A. D. Daniels, O. Farkas, J. B. Foresman, J. V. Ortiz, J. Cioslowski, and D. J. Fox, "Gaussian 09, Revision E.01." Gaussian, Inc., Wallingford CT, 2013.

[144] M. Abraham, B. Hess, D. van der Spoel, and E. Lindahl, "GROMACS Reference Manual. Version 2016.3," 2016.

[145] Jülich Supercomputing Centre, "JURECA: General-purpose supercomputer at Jülich Supercomputing Centre," *Journal of large-scale research facilities JLSRF*, vol. 2, no. A62, 2016.

List of publications

Publication related to the dissertation

- J. Lebert, E. M. Kratzer, A. Bourdick, M. Coric, S. Gekle, E. M. Herzig, "Directing the aggregation of native polythiophene during in situ polymerization", *ACS Omega*, vol. 3, no. 6, pp. 6388-6394, 2018.

Further publication

- F.-J. Kahle, C. Saller, S. Olthof, C. Li, J. Lebert, S. Weiß, E. M. Herzig, S. Hüttner, K. Meerholz, P. Strohriegl, A. Köhler, "Does Electron Delocalization Influence Charge Separation at Donor–Acceptor Interfaces in Organic Photovoltaic Cells?", *J. Phys. Chem. C.*, vol. 122, no. 38, pp. 21792–21802, 2018.

Conference talks

- J. Lebert, E. M. Kratzer, S. Pröller, O. Filonik, P. Fontaine, E. M. Herzig, "Tracking the reaction and film formation dynamics during in situ polymerization of polythiophene thin films", *DPG spring meeting*, Berlin, Germany, 11.-16.03.2018
- J. Lebert, E. M. Kratzer, M. Coric, V. Norman, E. M. Herzig, "Controlling the aggregation of native polythiophene during in situ polymerization", *Colloquium AK Synchrotronstrahlung, Bundesanstalt für Materialprüfung- und Forschung*, Berlin, Germany, 17.07.2017
- J. Lebert, E. M. Kratzer, M. Coric, S. Mansi, E. M. Herzig, "Controlling the aggregation of native polythiophene during in situ polymerization", *DPG spring meeting*, Dresden, Germany, 20.-26.03.2017
- J. Lebert, S Pröller, D. Moseguí González, "Polymer blends", *Summer School - Lehrstuhl für funktionelle Materialien, TUM*, Obertauern, Austria, 21.-24.06.2016
- J. Lebert, C. M. Palumbiny, "Conducting polymers", *Summer School - Lehrstuhl für funktionelle Materialien, TUM*, Obertauern, Austria, 24.-27.06.2014

Conference poster presentations

- J. Lebert, E. M. Kratzer, M. Coric, V. Norman, S. Mansi, E. M. Herzig, "Controlling the aggregation of native polythiophene during in situ polymerization", *7th Colloquium of the Munich School of Engineering*, Garching, Germany, 13.07.2017
- J. Lebert, E. M. Kratzer, E. M. Herzig, "Solution-processed insoluble polythiophene for organic solar cells", *GISAS Summer School 2016*, Garching, Germany, 18.-22.07.2016
- J. Lebert, E. M. Kratzer, E. M. Herzig, "Solution-processed insoluble polythiophene for organic solar cells", *6th Colloquium of the Munich School of Engineering*, Garching, Germany, 07.07.2016
- J. Lebert, A. Sanina, E. M. Kratzer, E. M. Herzig, "In situ polymerized insoluble semiconducting polymers for application in organic solar cells", *DPG spring meeting*, Regensburg, Germany, 06.-11.03.2016 15.-20.03.2015
- J. Lebert, K. Rahimi, P. Fontaine, E. M. Herzig, "In situ polymerization of active layers for organic solar cells", *GISAS conference*, Nice, France, 08.-11.09.2015
- J. Lebert, K. Rahimi, P. Fontaine, E. M. Herzig, "In situ polymerization of active layers for organic solar cells", *MatHero Summer School on Organic Photovoltaics*, Freudenstadt, Germany, 23.-27.08.2015
- J. Lebert, E. M. Herzig, "In situ polymerization of active layers for organic solar cells", *5th Colloquium of the Munich School of Engineering*, Garching, Germany, 09.07.2015
- J. Lebert, E. M. Herzig, "In situ polymerization of organic conductive thin films", *DPG spring meeting*, Berlin, Germany, 15.-20.03.2015

Acknowledgments

First of all I want to thank Prof. Dr. Eva M. Herzig for welcoming me in her research group and giving me the opportunity to work on this challenging topic. I am constantly amazed at how much energy and enthusiasm you put in all the projects that we are working on. Thanks for giving me the chance to improving many of my scientific and personal skills during my PhD time with you. I am especially happy you have always appreciated my creativity and were supportive of my ideas and the ways in which I tried to find solutions to all kinds of scientific problems. I really enjoyed the fact that we managed to merge our different scientific backgrounds into the successful completion of this project.

I additionally want to thank Prof. Dr. Peter Müller-Buschbaum and Prof. Dr. Christine Papadakis for providing lots of support over the last four years. I am glad I was always welcome to join your groups in scientific as well as social activities and benefit from your experience in our research fields. Without your help I would have been lost in the mysterious worlds of polymer physics and X-ray scattering techniques much more often.

The Bavarian State Ministry of Science, Research and the Arts is gratefully acknowledged for funding within the *Energy Valley Bavaria* project.

The beamtime data presented were always measured in teamwork. I am happy I got to perform these exciting experiments and solve the challenges that come with them with Dr. Philippe Fontaine, Dr. Stephanie Tassler, Nicolas Aubert, Dr. Stephan Pröller, Oliver Filonik, Margret Thordardottir, and Sebastian Weiß. Mihael Coric and Victoria Norman deserve my deep thanks for the night they spent collecting GIWAXS data at the ALS in Berkeley.

My thesis would not be what it is without several more people contributing to it. Leonhard Hofbauer implemented the first version of our heatable spin coater that we were happy to use as prototype in our project. For building its final version and providing lots of help on the way I want to thank the technical and electronic workshops of the chemistry department, especially Roland Schwarz and Max Wiedemann. Lorenz Bießmann, thank you for your time and patience at the SEM. Salma Mansi, who never tires of helping us out, put lots of effort in implementing the measurement setup for the mobility measurements

and eventually performing them. Thanks to my hard-working students Anna Sanina, Ana Rosa Aguilera, Grace Guu, and Stephan Wanckel. I had so much fun working with you on all of your different projects. At this point, the biggest thanks belongs to Eva Kratzer for being the best working student I could have imagined. Thank you for everything!

Thanks to Angela Brunnbauer, Sabine Kutscherauer, Susanna Fink, Marion Waletzki, and Carola Kappauf for taking care of all the administrative tasks while at the same time having an open ear whenever I needed help or simply a reason to escape my desk for a while.

Dr. Lars Menger, thank you for being my mentor throughout this project and helping out with your pragmatism and shared pleasure in the occasional cold beverage.

For proof reading this thesis I'd like to thank Dr. Stephan Pröller, Mihael Coric, Oliver Filonik, and Nitin Saxena.

During my PhD time I got to learn that you can get the chance of belonging to more than one family. I am grateful for being part of the best working group there probably ever was and which turned into my second family over the course of the last four years. Without you, the struggle of writing this thesis would not have been such an unforgettably great time! Thank you, Dr. Stephan Pröller, Mihael Coric, Oliver Filonik, Eva Kratzer, Margret Thordardottir, Anna Sanina, Leonhard Hofbauer, Salma Mansi, Sebastian Weiß, Ana Rosa Aguilera, Leon Katzenmeier, and Tom Wollschläger. I am especially happy about my fellow PhD students Stephan, Mihi, and Oli. We all have to leave university eventually, but I will take you with me wherever I go!

I am grateful that my time at TUM was accompanied by many more excellent people who made it an unforgettable experience. Though this list could be endless, I want to especially mention Nitin Saxena, Johannes Schlipf, Franziska Löhrer, Lorenz Bießmann, Nuri Hohn, Simon Schaper, Lucas Kreuzer, Dr. Christoph Schaffer, Dr. Claudia Palumbiny, Dr. Daniel Moseguí-Gonzalez, and Dr. Volker Körstgens. Without you, the PhD time wouldn't have been the same. Thanks to the whole Chair of Functional Materials who always welcomed our small working group and made us feel at home in the physics department. Many thanks to the crazy PMB gang, I am proud to be a member of the best-looking band ever. Dr. Francoise Schäfers, Anna Sib, Dr. Hülya Aldemir, Dr. René Richarz, Marko Cigler, Susanne Mayer, Marie-Kristin von Wrisberg, Maximilian Fottner, Steffen Säubert, Florin Loghin, Marius Loch, the nano group, Akhila Jambagi, Michael Kramer, Korbinian Schechner, Christian Dirschl, and Dr. Patricia Laboureur: Thank you for helping me with scientific discussions, after-work beers, your moral support, legendary athletic competitions, endless coffee breaks, party nights, and motivation as well as distraction whenever I needed them. Here's to us!

I am very lucky I got to spent my studying times with Dr. Patricia Laboureur and Anke Korte, who made all the work and everything beyond an exceptionally fun time. I am glad we share so many memories from Bremen, Cologne, and Munich, and I am pretty sure we will create many more in the future!

A special and deep thank goes to Anja Dörge, Svenja Kinzel, Julia Schukowski, Miriam Jansing, Janika Stehmeier, Lena Fehrcke, Susanne Heiland, Mariele Müller, Carolin Güneri, and Inga Hermann. Thank you for being a reliable constant in my life and being the wonderful and inspirational women you are. Also, I am more than blessed to have Mathias Wunderlich and Arne-Steffen Möller in my life, who are always enthusiastically and unconditionally supporting me.

Finally, I want to thank my family for their unlimited support through those many years. I know I can always count on you. Jan, thank you for patience and endorsement, and being by my side all this time.